

**PROGRESS TOWARDS AN AUTOMATIC, MICROFABRICATED POLYMER  
AIR -FLUID SAMPLING INLET**

**Final report for DARPA Contract DAAH01-96-C-R155**

**November 20, 1997**

**Sponsored by**

**Advanced Research Projects Agency (DOD)  
ARPA Order PH 1 SBIR PROG RTW C7-96  
Issued by U.S. Army Missile Command Under  
Contract No. DAAH01-96-C-R155 A00001**

Name of Contractor:	BOMEC, L.L.C.	Principal Scientist:	John Madden
Business Address:	19 Jersey Street	Phone Number:	617-253-8116
	Marblehead, MA 01945	Short Title of Work:	Creation of conducting polymer air-to-liquid pumps.
Effective Date of Contract:	July 1, 1996		
Contract Expiration Date:	January 31, 1997		
Reporting Period:	July 1, 1996 - January 31, 1997		

**Disclaimer**

“The views and conclusions contained in this document are those of the authors and should not be interpreted as representing the official policies, either expressed or implied, of the Advanced Research Projects Agency or the U.S. Government.”

**UNCLASSIFIED**

“Approved for public release; distribution unlimited.”

19971126 131

**DTIC QUALITY INSPECTED 3**

## **ABSTRACT**

The primary objective of this study is to develop a miniature autonomous aerosol-to-fluid sampling inlet as the input to a chemical or biological agent detection system. The principal challenge is creation of a pump capable of generating the required flow of air into a liquid phase ( $>0.1 \text{ cm}^3/\text{min}$ ), given the constraints of size ( $< 2.5 \text{ cm}^3$ ), back pressure to inject the aerosol into the liquid phase ( $40 \text{ kPa}$ ) and available electrical power. The Phase I goal is to demonstrate the feasibility of employing conducting polymer actuators in this application.

Our report, to our knowledge, is the first extensive experimental measurements delineating the relationship between stress, strain, frequency bandwidth, lifetime and energy consumption achievable with conducting polymers. Conducting polypyrrole actuators meet the air sampler pump requirements, notably demonstrating high stresses ( $5 \text{ MPa}$ ,  $10 \times$  mammalian muscle and the highest reported yet for conducting polymer actuators), and mechanical displacement bandwidths exceeding  $10 \text{ Hz}$ . Furthermore, while actuators have heretofore depended upon a liquid electrolyte for operation, we demonstrate here the operation of an electrically-activated conducting polymer bilayer actuator independent of a liquid electrolyte (i.e. in air).

Our pump design analysis reveals that displacement pumps prove more effective than inertial mechanisms (due to the low Reynolds number regime) for injecting air into a fluid carrier stream. Accordingly, we built and tested both a peristaltic and two versions of a bellows pumps actuated by nickel titanium shape memory alloy fibers and demonstrated pumping speeds two orders of magnitude greater than targeted ( $>10 \text{ cm}^3/\text{min}$ ). Our actuator analysis showed that shape memory alloys have similar contractile characteristics to conducting polymers except for a lower electromechanical efficiency. Finally, a new technology is described, in which gas is electrochemically evolved, pressurizing a porous capsule that emits a target compound at a controllable rate.

## TABLE OF CONTENTS

1.0	Introduction.....	3
1.1	Phase I work .....	7
2.0	Air Inlet Pump Design Considerations .....	10
2.1	Pump requirements .....	10
2.2	General Considerations: Inertial vs. Displacement Pumps.....	11
2.3	Pump design and actuator properties .....	11
3.0	Conducting polymer actuators .....	15
3.1	Conducting polymers – general characteristics.....	15
3.2	Conducting Polymer Actuators.....	17
3.2.1	Force per Cross-sectional Area.....	20
3.2.2	Strain .....	21
3.2.3	Strain Rate .....	22
3.2.4	Energy Density, Efficiency and Power Density.....	23
3.3	Conducting Polymer Actuator Theory, Experiments and Results.....	24
3.3.1	Contraction mechanisms.....	25
3.3.2	Film Modeling: Mechanical Response .....	26
3.3.3	Film Synthesis.....	34
3.3.4	Film Actuator Characterization.....	36
3.3.5	Bilayers .....	49
3.3.6	Bilayer operation in Air.....	55
3.4	Summary and Conclusions .....	57
4.0	Voltage-controlled gas release capsule.....	59
4.1	Introduction .....	59
4.2	Nitrogen gas controlled release capsule .....	61
4.2.1	Electrochemical Cell Design .....	62
4.2.2	Experimental Results .....	62
4.2.3	Conclusion regarding Nitrogen Generator.....	63
4.3	Oxygen gas controlled release capsule .....	64
4.3.1	Electrochemical Cell Design .....	64

4.3.2	Experimental Results .....	65
4.3.3	Conclusion regarding oxygen gas pump .....	68
4.4	Proposed applications and future work .....	70
5.0	Shape memory alloy pumps.....	71
5.1	Introduction .....	71
5.2	Overview of SMA actuators .....	72
5.2.1	Principle of Operation.....	72
5.3	Applications of NiTi Shape Memory Alloys .....	79
5.4	Shape memory alloy air inlet pump .....	81
5.4.1	SMA Bellows pump-Version 1.....	81
5.4.2	SMA Bellows Pump – Version 2.....	87
5.4.3	Peristaltic SMA pump .....	91
6.0	Summary and Conclusions .....	95
7.0	Acknowledgements .....	98

## TABLE OF FIGURES

FIGURE 1: SCHEMATIC SHOWING THE SALIENT SUBSYSTEMS OF THE PROPOSED BOMECAIR SAMPLER.....	4
FIGURE 2: SCHEMATIC DEPICTING PROPOSED DETECTOR MODULE FOR BOMECAIR SAMPLER.....	6
FIGURE 3: SOME APPLICATIONS OF CONDUCTING POLYMERS.....	15
FIGURE 4: SCHEMATIC SHOWING BOND STRUCTURE OF THREE CONDUCTING POLYMERS. WE USED POLYPYRROLE AND POLYANILINE CONDUCTING POLYMERS IN OUR ACTUATOR STUDIES.....	16
FIGURE 5: SCHEMATIC SHOWING MECHANISM RESPONSIBLE FOR VOLUMETRIC CHANGE IN CONDUCTING POLYMERS.....	17
FIGURE 6: COMPARISON OF MAXIMUM STRESS GENERATED BY DIFFERENT ACTUATOR TYPES. NOTE THE PREDICTED MAXIMUM STRESS FOR CONDUCTING POLYMERS EXCEEDS THAT POSSIBLE WITH OTHER ACTUATORS CONSIDERED EXCEPT FOR SHAPE MEMORY ALLOYS.....	18
FIGURE 7: MAXIMUM STRAINS REPORTED FOR DIFFERENT ACTUATORS. NOTE THAT IN THE CASE OF CONDUCTING POLYMERS IT IS PREDICTED THAT THE MAXIMUM STRAIN CAN VARY OVER A LARGE RANGE BECAUSE OF ITS DEPENDENCE ON THE SPECIFIC POLYMER CONFIGURATION (E.G. MORPHOLOGY, DOPANT ION, ETC.).....	19
FIGURE 8: CONDUCTING POLYMERS HAVE HIGH STRAIN RATES AS INDICATED BY THE HIGH ROLL-OFF FREQUENCY OF THE MECHANICAL FREQUENCY RESPONSE OF AN ELECTRICALLY-ACTIVATED CONDUCTING POLYMER BILAYER.....	20
FIGURE 9: COMPARISON OF ENERGY DENSITIES PRODUCED BY DIFFERENT ACTUATOR TYPES. THE ACHIEVED ENERGY DENSITY FOR CONDUCTING POLYMERS IS RATHER LOW (COMPARABLE TO POLYMER GELS AND SKELETAL MUSCLES) BUT THE PREDICTED ENERGY DENSITIES BASED ON IMPROVED MATERIALS IS SEVERAL ORDERS OF MAGNITUDE GREATER THAN MOST OTHER ACTUATORS LISTED.....	21
FIGURE 10: COMPARISON OF ELECTRO-MECHANICAL EFFICIENCIES ACROSS DIFFERENT ACTUATOR TYPES. WITH ELECTRICAL ENERGY RECOVERY, THE CONVERSION EFFICIENCY OF CONDUCTING POLYMERS CAN BE QUITE GOOD.....	22
FIGURE 11: POWER DENSITY COMPARISON ACROSS DIFFERENT ACTUATOR TYPES.....	24
FIGURE 12: SCHEMATIC DEPICTING THE STANDARD LINEAR NETWORK MECHANICAL MODEL USED TO MODEL THE PASSIVE MECHANICAL BEHAVIOR OF A CONDUCTING POLYMER.....	27
FIGURE 13: STRESS RELAXATION IN RESPONSE TO A STEP IN STRAIN (EQUATION 5).....	29
FIGURE 14: PASSIVE STRESS-STRAIN CURVE FOR A POLYPYRROLE FILM IN A PROPYLENE CARBONATE ELECTROLYTE. THE FILM IS SUBJECT TO A STRAIN RATE OF 0.0012HZ. THE DARK LINE	

INDICATES THE MEASURED VALUE WHILE THE DASHED LINE IS A FIT TO THE PASSIVE MODEL (EQUATION 3).....	30
FIGURE 15: PHOTOGRAPH OF APPARATUS FOR CHEMICAL, MECHANICAL AND ELECTRICAL CHARACTERIZATION OF CONDUCTING POLYMER FILMS.....	36
FIGURE 16: CLOSE-UP OF THE ELECTRO-CHEMO-MECHANICAL TESTING APPARATUS SHOWING THE STRAIN GAUGE, SALT BRIDGE AND CLAMPING ARRANGEMENT OF THE PYRROLE FILMS. 37	
FIGURE 17: STRESS RELAXATION FOLLOWING A 2% STEP IN STRAIN.....	39
FIGURE 18: STRESS-STRAIN FOR DIFFERENT INCREASING STRAIN RATES. FROM TOP TO BOTTOM, THE RATES APPLIED TO THE FILM ARE 0.02 HZ, 0.005 HZ, 0.00125 HZ, $3.1 \times 10^{-4}$ HZ, $8 \times 10^{-5}$ HZ AND $2 \times 10^{-2}$ HZ.....	40
FIGURE 19: STRESS-STRAIN CURVES AS A FUNCTION OF DECREASING STRAIN RATE, FROM THE TOP 0.008 HZ; 0.002 HZ; 0.0005 HZ; AND 0.000125 HZ FOR THE BOTTOM CURVE.....	41
FIGURE 20: TYPICAL FILM ACTIVATION SEQUENCE. INPUT TO THE FILM IS CHARGE (CURRENT, MIDDLE PLOT) AND THE EVOLUTION OF STRESS (TOP PLOT) AND VOLTAGE (BOTTOM PLOT) ARE MEASURED WITH TIME.....	42
FIGURE 21: STRESS GENERATED IN FREE STANDING POLYPYRROLE FILM AS CHARGE IS EXTRACTED FROM FILM.....	44
FIGURE 22: STRESS GENERATED IN FREE-STANDING POLYPYRROLE FILM AS INCREASING AMOUNT OF CHARGE IS INJECTED INTO THE FILM.....	44
FIGURE 23: STRAIN INDUCED IN A FREE STANDING POLYPYRROLE FILM WITH A CONSTANT BIAS STRESS OF 5 MPa AND AN ACTIVATION CURRENT OF 10 mA CURRENT.....	45
FIGURE 24: STRAIN INDUCED IN A FREE STANDING POLYPYRROLE FILM WITH A CONSTANT BIAS STRESS OF 5 MPa AND AN ACTIVATION CURRENT OF -10 mA CURRENT.....	46
FIGURE 25: STRESS INDUCED IN A POLYPYRROLE FILM ACTUATOR AS A FUNCTION OF ELECTRICAL STIMULATION FREQUENCY.....	48
FIGURE 26: SCHEMATIC SHOWING MOVEMENT OF IONS IN CONDUCTING POLYMER BILAYER. ....	49
FIGURE 27: DIMENSIONLESS RELATIONSHIP BETWEEN CURVATURE AND RELATIVE THICKNESS OF THE BILAYER LAYERS FOR VARIOUS RATIOS OF BETWEEN THE TWO LAYERS. ....	50
FIGURE 28: DIMENSIONLESS PLOT SHOWING BILAYER CURVATURE (AND THUS DEFLECTION) AS A FUNCTION OF RELATIVE THICKNESS OF THE BILAYER LAYERS AND ELASTIC MODULI OF EACH LAYER. ....	51
FIGURE 29: PHOTOGRAPHS SHOWING POLYPYRROLE CONDUCTING BILAYER ACTIVATED WITH +/- 6 V SQUARE WAVE APPLIED WITH A 1 HZ FREQUENCY. THE ELECTROLYTE SOLUTION WAS A 0.1M DODECYLBENZENESULFONATE AQUEOUS SOLUTION. ....	52

FIGURE 30: POLYPYRROLE BILAYER MECHANICAL FREQUENCY RESPONSE IN A 0.1M DODECYLBENZENESULFONATE AQUEOUS SOLUTION. THE EXCITATION VOLTAGE WAS A +/- 6 V SQUARE WAVE .....	53
FIGURE 31: ENCAPSULATED BILAYER CONFIGURATION FOR OPERATION OF CONDUCTING POLYMER ACTUATOR IN AIR.....	54
FIGURE 32: AIR BILAYER ACTIVATED WITH +/- 5V APPLIED AT 0.1 HZ.....	55
FIGURE 33: MECHANICAL FREQUENCY RESPONSE OF AN ENCAPSULATED CONDUCTING POLYMER BILAYER. EACH CURVE PLOTTED CORRESPONDS TO A DIFFERENT PEAK-TO-PEAK SQUARE WAVE VOLTAGE APPLIED TO THE BILAYER. FOR VOLTAGES GREATER THAN 5V, THE 3DB ROLL-OFF OCCURS AT A FREQUENCY > 10HZ .....	56
FIGURE 34: SCHEMATIC SHOWING CONTROLLED-GAS RELEASE CAPSULE CONCEPT. GAS EVOLVED FROM THE ELECTROCHEMICAL CELL PRESSURIZES THE PRIMARY GAS BLADDER RESULTING IN A PRESSURE APPLIED TO THE SECONDARY BLADDER THAT EXPELS ITS CONTENTS .....	59
FIGURE 35: SCHEMATIC SHOWING GENERAL EXPERIMENTAL LAYOUT FOR N <sub>2</sub> GAS CELL.....	62
FIGURE 36: CELL CURRENT DENSITY AS A FUNCTION OF TIME FOR DIFFERENT STARTING CURRENTS. ....	63
FIGURE 37: SCHEMATIC OF ELECTROCHEMICAL CELL AND REACTIONS TO GENERATE OXYGEN GAS AT ANODE.....	65
FIGURE 38: INFLATION OF A MEMBRANE WITH OXYGEN GAS GENERATED BY THE MINIATURE ELECTROCHEMICAL CELL.....	66
FIGURE 39: COMPARISON OF ELECTROCHEMICAL CELL CURRENT AS A FUNCTION OF TIME WITHOUT (A) AND WITH (B) WATER RESERVOIR. NOTE THAT THE RATE OF GAS PRODUCTION IS PROPORTIONAL TO CELL CURRENT .....	67
FIGURE 40: VOLUME OF GAS PRODUCED AS A FUNCTION OF TIME FOR TWO DIFFERENT ELECTROCHEMICAL CELL CURRENTS.....	68
FIGURE 41: DEMONSTRATION OF SCALING OF ELECTROCHEMICAL GAS CELL FOR PUMPING LARGE VOLUMES. TWENTY ELECTROCHEMICAL CELLS ARE MOUNTED WITH OUTLETS THAT OPEN INTO A COMMON MANIFOLD. THE LARGE VOLUME IS FILLED WITH OXYGEN GAS IN APPROXIMATELY 1.5 DAYS OF PUMPING @ 2 M <sup>3</sup> PER CELL.....	69
FIGURE 42: COMPARISON OF MAXIMUM STRESS ACROSS DIFFERENT ACTUATOR TECHNOLOGIES. NOTE THAT SMA CAN GENERATE STRESS LEVELS THAT EXCEED SUCH CONVENTIONAL ACTUATOR TECHNOLOGIES AS ELECTROMAGNETIC MOTORS BY >10 <sup>4</sup> AND PIEZOELECTRIC CERAMICS BY A FACTOR OF 10.....	73

FIGURE 43: COMPARISON OF MAXIMUM STRAIN ACROSS DIFFERENT ACTUATOR TECHNOLOGIES. SMA FIBERS ARE WITHIN A FACTOR OF 10 OF ELECTROMAGNETIC, PNEUMATIC AND HYDRAULIC ACTUATORS AND OVER A FACTOR OF 100 TIMES LARGER THAN PIEZOELECTRIC CERAMICS.....	74
FIGURE 44: MAXIMUM STRAIN RATE FOR DIFFERENT ACTUATOR TECHNOLOGIES. SMA FIBERS EXHIBIT STRAIN RATES THREE TIMES LARGER THAN ELECTROSTATIC ACTUATORS BUT SMALLER THAN ELECTROMAGNETIC, PNEUMATIC AND PIEZOCERAMICS BY THE SAME AMOUNT.....	75
FIGURE 45: COMPARISON OF POWER PER UNIT MASS ACROSS DIFFERENT ACTUATOR TECHNOLOGIES. .....	76
FIGURE 46: COMPARISON OF ELECTROMECHANICAL EFFICIENCY ACROSS DIFFERENT ACTUATOR TECHNOLOGIES. NOTE THAT SMA EFFICIENCY IS SUBSTANTIALLY LOWER -BY ABOUT A FACTOR OF 10- THAN OTHER PUMP ACTUATOR TECHNOLOGIES.....	77
FIGURE 47: SMA BELLOWS PUMP SCHEMATIC AND PHOTOGRAPH SHOWING DETAIL OF HOUSING CONFIGURATION.....	82
FIGURE 48: SCHEMATIC AND PHOTOGRAPH SHOWING DETAIL OF NITI FIBER VALVE. ....	84
FIGURE 49: SCHEMATIC OF EXPERIMENTAL ARRANGEMENT TO EVALUATE BELLOWS PUMP OPERATION.....	85
FIGURE 50: SCHEMATIC SHOWING SECOND VERSION OF NITI BELLOWS PUMP .....	88
FIGURE 51: SCHEMATIC SHOWING EXPERIMENTAL ARRANGEMENT TO EVALUATION OPERATION OF SECOND NITI BELLOWS PUMP.....	89
FIGURE 52: PHOTOGRAPH OF SMA BELLOWS PUMP-VERSION 2. THE TWO PUMPING CHAMBERS ARE VISIBLE ON OPPOSITE END OF THE WHITE DELRIN ROD IN THE CENTER OF THE PICTURE. THE ATTACHMENT POINTS FOR THE NITI FIBERS ARE THE AL DISKS LOCATED AT EITHER END OF THE DELRIN ROD. ATTACHED TO THE ROD ENDS ARE THE BRASS PLATES THAT ARE FLEXED TO CHANGE THE DIMENSIONS OF THE PUMPING CHAMBER. IN THE UPPER RIGHT IS ONE OF THE CHECK VALVES.....	90
FIGURE 53: NITI FIBERS PERISTALTIC PUMP SCHEMATIC.....	92
FIGURE 54: PHOTOGRAPH SHOWING SMA PERISTALTIC PUMP CONFIGURATION. ....	93
FIGURE 55: SCHEMATIC SHOWING EXPERIMENTAL ARRANGEMENT TO EVALUATION OPERATION OF NITI FIBER PERISTALTIC PUMP. ....	94

## 1.0 Introduction

Detection of air-borne pathogens (bacteria, viruses or toxins) has become increasingly important in medicine, environmental monitoring, law enforcement and military activities involving chemical and biological warfare (CBW). In response, considerable progress is being made in the development of bio- and chemical detection devices and subsystem components. The need for small, rugged sensor units for fast, accurate detection of airborne pathogens in the field has motivated application of microfabrication techniques to create a micro PCR-based sensors on a chip and realize various biodetection mechanisms in small-scale form.

Lagging behind sensor progress is development of small, powerful actuators to sample and transport the pathogen-laden air to a biochemical sensor<sup>1</sup> for analysis and the integration of sensors and actuators into an air sampler system. As outlined in our original SBIR Phase I proposal, we envision such a system to contain the following key components:

1. an inlet filter to block large, unwanted particulates from entering and clogging the sensor,
2. an air inlet pump for injecting air loaded with aerosol into a carrier fluid at a rate compatible with the response time of the biochemical sensors (between  $0.1 - 1 \text{ cm}^3/\text{min}$ ) and finally,
3. an integrator module that acts to separate aerosol particles from the air stream and incorporate them into the detector carrier fluid stream.

In this final report for Phase I, we report on the results of our investigation into electrically-activated conducting polymers as the actuator in a miniature air inlet pump as well as the actuator in the active enclosures and fluid handling devices located in the integrator module. This relatively new actuator technology exhibits the stress, strain and power per unit mass required of actuators needed in the different air sampler subsystems. We now focus on the actuator requirements of the air inlet pump and the devices resident in the integrator module. Necessary characteristics of the sampler inlet filter have been covered by others (see Grinshpun *et al.*<sup>2</sup> for example) and will not be discussed further here.

---

<sup>1</sup> EAI, Inc., "Chemical weapons treaty verification technology R/D: Best technical approach", pp. 25-26, EAI 86/31.00702 U.S. Army CRDEC (K300 006) 1991.

<sup>2</sup> Grinshpun, S., Chang, C-W., Nevalainen, A. and Willeke, K., J. Aerosol. Sci., 25 pp. 1503-1515, 1994.

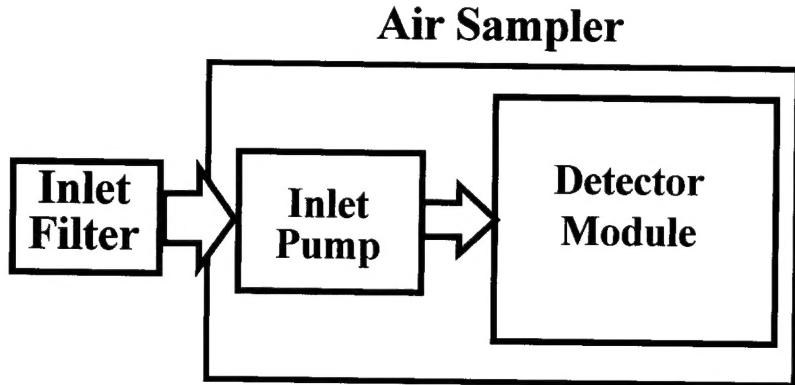


**Figure 1:** Schematic showing the salient subsystems of the proposed BOMEC air sampler.

The role of the air inlet pump is to inject air passed through the inlet filter and laden with aerosol into a carrier fluid for transport to the integrator module containing the biochemical sensors. Maximizing the efficiency by which aerosols are introduced into the carrier fluid is a critical task for the pump and there are several methods available. Inertial methods, such as fans and centrifuges, bend high speed air flows such that the inertia of the airborne particulate causes it to leave the stream and be collected. Electrostatic, thermal and other types of impingers have also been investigated.

The viscosity of air suggests that inertial methods become increasingly ineffective at small scales as viscous forces begin to dominate. The large inertia needed to overcome these forces require inertial forces to be generated that are impractical for a miniature air sampler. Instead, we have focused our efforts on pump mechanisms that can produce the instantaneous pressures necessary to force air into a liquid. The first pump mechanism considered is based on the piston action of a stiff membrane actuated by an antagonistic pair of actuators or a single actuator biased with an opposing force. The pump inlet and outlet are each one-way valves. On the intake stroke, the outlet valve closes, the inlet valve opens and fluid is drawn into the piston chamber. As the piston moves to compress the chamber, the inlet valve closes and the outlet valve opens. The increased pressure inside the chamber forces fluid out through the open outlet valve and fluid is expelled from the pump. As the piston

returns to its starting position, the outlet valve closes, the inlet valve opens and the chamber is refilled with fluid from outside the pump.

The volume pumped per piston stroke depends on the piston stroke length and cross-sectional area while the pumping rate depends on the interplay of a variety factors including actuator strain rate and power per unit mass. The maximum pressure generated by the pump is determined ultimately by the maximum stress generated by the actuator. Advantages of the piston design are many and include a large volume of gas displaced per pump stroke, a high pumping rate for a rapid stroke rate and the capability of generating high pressure heads between inlet and outlet. One drawback with this design, though, is the necessity for either passive or active valves to ensure uni-directional fluid flow from inlet to outlet.

A second pump mechanism is based on peristaltic action. Actuators are arranged such that their sequential contraction squeezes a bolus of material through a flexible tube. The volume of material pumped is directly dependent on the volume of tube collapsed by the actuators during the contraction sequence. The mass flow rate of material through the pump is determined by the rate of volume change per contraction cycle. Thus a given flow rate is achieved by either small volume changes at high repetition rates or large volume changes at low repetition rates. In the first case, the time modulation of the flow rate is small while in the second case the flow pulsation is larger. Actuators characteristics required for a peristaltic pump include those capable of generating large stresses and strains at moderate strain rates.

A variety of materials can be pumped in this manner including gases, liquids of different viscosity and slurries. A peristaltic pump operates without valves, which keeps the pump design and construction simple. High outlet pressures can be generated by the peristaltic action but with the potential disadvantage of a pulsating flow. However, the flow pulsation could be advantageous if delivery of precise and discrete quantity of material is desired. Additionally, the modulated mass flow when coupled with a detector technology could be used as part of a signal-processing scheme to increase detection sensitivity of materials in the flow stream. Lines can be multiplexed into a single pump configuration to either increase the rate or the diversity of materials (i.e. a different material per pumping channel) pumped.

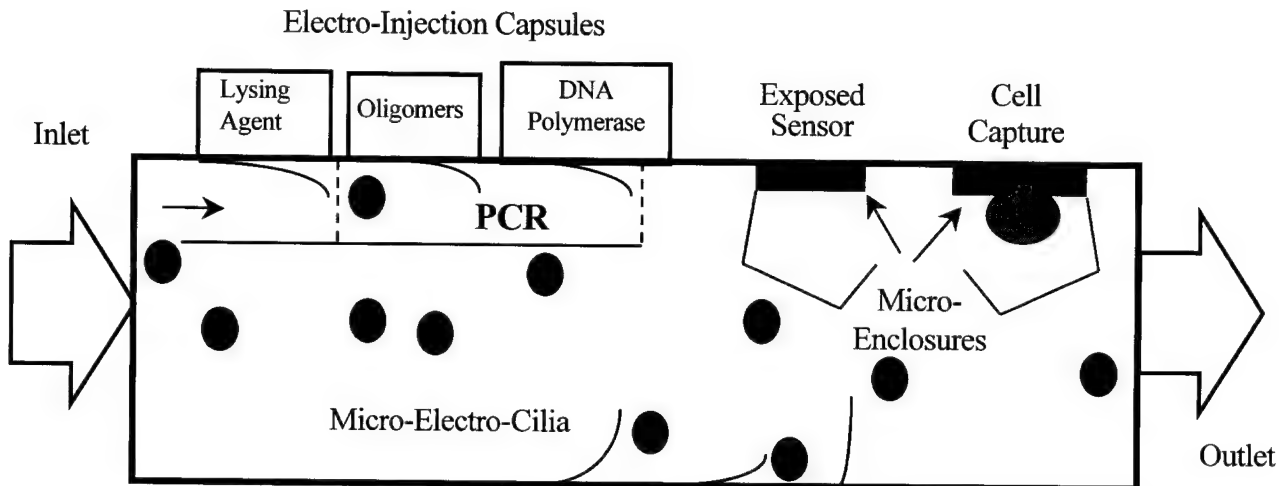


**Figure 2:** Schematic depicting proposed detector module for BOMECA air sampler.

After the air inlet pump is the detector module in which are located biological and chemical sensors for analyzing the carrier stream into which the aerosol and other particulates are transported. Operation of many biological and chemical sensors in “real-world” environments results in a high false-positive detection rate from ambient non-targeted chemicals that rapidly degrade the sensor utility. To combat this degradation in sensor performance and ensure high reliability, an additional requirement for the detector module is the pre-selection of pathogens, based on *a priori* characteristics such as molecular size or weight, before introduction to the biochemical detectors. Further improvements in sensor performance are expected if the most sensitive detectors are protected and exposed only when on-board alarm detectors indicated a need to confirm identification or presence of a pathogen.

Small, efficient and powerful conducting polymer actuators play a key role in implementing this detection strategy. As shown in Figure 2, there are essentially three components to the module in which actuators are needed. Bilayer conducting polymer actuators are integral to the construction of electrically-driven enclosures for isolation and subsequent exposure of sensitive sensor elements. Micro-electro cilia made from electrically driven conducting polymer bilayers attached to the module

wall can enhance fluid movement through the module. Finally, electrically-driven controlled release capsules to release compounds for pre-conditioning the sample stream to enhance or aid detector sensitivity. The following section overviews our work in Phase I to create conducting polymer actuators and other actuator types that satisfy the general criteria as set forth above.

### ***1.1 Phase I work***

A critical technology for miniaturization of gas-to-liquid samplers is the actuator that can pump air or aerosol into a liquid carrier for transport to a detector suite. Thus, the first objective of this Phase I study is to identify and demonstrate an actuator with the performance characteristics for driving the flow of gas into a liquid phase. A second important aspect of a miniature gas-to-liquid sampler that we report progress on is the development of actuated mechanisms for transport of analytes within the detector's liquid phase and of methods to control the release of agents into the liquid. This capability is necessary in order to encapsulate and then allow selective exposure of sensitive detector elements in the inlet sampler.

The very high forces per cross-sectional areas and strains achievable in conducting polymer actuators, along with their light weight, flexibility and low, cost led us to propose conducting polymers as the actuator technology of choice for autonomous air sampling systems. In the course of pump development it was found that very little rigorous testing of material performance had been done with these materials thus impeding the design and realization of a suitable inlet pump. This report presents, to the best of our knowledge, the most comprehensive investigation of conducting polymer actuator properties to date and the first presentation of a self contained air-operated conducting polymer actuator. It is shown that these characteristics match the aerosol sampler pump requirements, but that a Phase II technical development is needed to fabricate a field testable conducting polymer bioaerosol inlet system.

A key Phase I deliverable is an inlet pump. This deliverable was attained using nickel titanium (NiTi) shape memory alloy (SMA) materials. The measured characteristics of material and actuator properties for both the SMA and conducting polymers, coupled with a design tradeoff analysis indicated that peristaltic and bellows-type pumps are the most effective primary pumping mechanisms

actuated with either actuator type. Given the similar properties of the two material classes, the SMA pumps served to prove designs to be implemented in the next phase of this work.

The SMA bellows pumps thus constructed readily transported over two orders of magnitude more air into a fluid phase than is required by the detectors. The SMA-actuated peristaltic pump, on the other hand, has a lower flow rate yet exhibits the ability to generate higher pressure heads, thereby enabling the pumping of liquids and slurries in addition to gas. Shape memory alloys are the only other actuator technology with properties similar to those of conducting polymers. Nickel titanium fibers are well characterized and have highly favorable specific stress, strain and energy density. Indeed, they are second only to conductive polymers in the properties needed for an effective actuator or pump. Hence these materials were deemed suitable for demonstration of different air inlet pump designs in the prototype phase. Their principal drawback is their low electromechanical efficiency thus necessitating relatively large current densities to activate. This problem is partially overcome by driving the NiTi fibers with brief current pulses. However, conducting polymers are the best suited technology for miniaturized air inlets for several reasons including materials compatibility, low detectability and a potentially much higher electromechanical efficiency.

Prior to this work, conducting polymer actuators were restricted to operation in a liquid electrolyte environment. This arose from the mechanisms associated with contraction and expansion. Electrochemically induced changes in oxidation state of the polymer add or remove charge from the polymer backbone. This charge is balanced by the flow of ions into or out of the material from a liquid electrolyte. The necessity of the bulk liquid environment restricts the scope of actuator designs and the environments in which they can operate. Thus a major thrust of this work was to demonstrate the operation of conducting polymer-based actuators in air.

Air operation was achieved by choosing a gel-based electrolyte rather than a liquid one and by encapsulation of the gel and polymer into a single, electrically activated bilayer actuator. The presence of the gel electrolyte and the encapsulation method employed appears not to degrade the actuator performance or its other material properties. Furthermore, isolation of the actuator system from its surroundings enables operation in environments inhospitable to the actuator constituents themselves in addition to preventing contamination of the gas or liquid stream pumped with the

actuator. This technical achievement represents a major advance for the design and construction of aerosol sampling systems and, in general, paves the way for much broader application of conducting polymer-based actuators.

A second issue relating to the detection of chemical and biological agents is the ability to control the release of chemicals into the detector's liquid phase. Some scenarios requiring this action include:

- antidotes to pathogen exposure which is contained in lightweight chemical protective gear;
- cell membrane lysing agents for PCR;
- compounds for calibrating chemical and biological detectors;
- ‘antibodies’ to aid detection and/or enhance the sensitivity of detectors to a specific material, and;
- temporal modulation of the material mass flow to the detectors as a means to improve the detector signal to noise through application of correlation detection techniques.

The first technology we have investigated for this application are bilayer flaps and containers that can enclose agents to be released, and subsequently be electrically activated to release material. The second is a new technology in which material is slowly released in a controlled manner due to pressure applied by a gradually expanding bladder driven by electrochemical decomposition of water vapor in the air or from an onboard, microliter-sized water reservoir. This report presents results that quantifies the operation of the controlled release gas capsule and demonstrates it is a very effective means to release volatile and gaseous substances in a controlled manner.

Section Two first summarizes the air inlet pump requirements and relates these to material properties inherent to conducting polymers. After a brief review of the pump requirements, several competing designs are evaluated and recommendations given as to the pump designs best suited to take advantage of the electromechanical properties of conducting polymers. Section Three describes the conducting polymer work in detail, starting with passive and active models of their actuation behavior. Film and encapsulated bilayer fabrication techniques are then given followed by passive and active mechanical measurements of free standing films in a liquid electrolyte and activated mechanical measurements of the encapsulated bilayers. Section Four discusses the controlled release gas capsule and its operation while Section Five, the final section, describes the design and performance of peristaltic and bellows-type SMA actuated pumps for pumping air into water.

## 2.0 Air Inlet Pump Design Considerations

This section aims to determine the most effective air inlet pump design and performance given the measured properties of conducting polymer actuators. First the air pump requirements are listed after which the properties of conducting polymer actuators relevant to pump operation are summarized. It will be shown in Section 3 of this report that the conducted polymer actuators we investigate as part of this work satisfy most of the requirements pertinent to air pump operation. Viable air inlet pump designs are then assessed based on the pump requirements and actuator properties.

### 2.1 *Pump requirements*

Pump performance requirements as determined from ARPA are listed below. Note that the original assumption was that an air flow of  $10 \text{ cm}^3/\text{min}$  was required. It now appears that  $0.1 \text{ cm}^3/\text{min}$  is a sufficient flow rate given the slow response time of most biological and chemical detectors. The originally calculated pressure drop given here forms a very conservative upper bound. The estimated pressure drops and flow rate of air into liquid required of the pump is as follows:

- Flow rate be  $>0.1 \text{ cm}^3/\text{min}$ .
- Pressure drop for the maximum flow ( $10 \text{ cm}^3/\text{min}$ ) estimated to be  $< 10 \text{ kPa}$ .
- Viscous drag on walls is  $\sim 3 \text{ kPa}$ . This drag is due primarily to flow through a length  $L$  of the inlet nozzle.
- Head of liquid in detector  $\sim 0.1 \text{ kPa}$ . This is an estimate of the maximum pressure that might reasonably be expected due to the detection liquid head, demonstrating that this effect is negligible.
- Surface tension to enter fluid (assumed to be similar to water)  $\sim 1 \text{ kPa}$ .
- Inlet filter drop  $\sim 0.5 \text{ kPa}$ .

The total pressure drop for a flow rate of  $10 \text{ cm}^3/\text{min}$  is estimated to be no greater than  $15 \text{ kPa}$ . Other targeted specifications relevant to pump operation and its integration into the air sampler are:

- |                     |   |
|---------------------|---|
| (a) Pump flow rate  | $10^{-1} \text{ cm}^3/\text{min}$ at $20 \text{ kPa}$ |
| (b) Size of sampler | $< 8 \text{ cm}^3$ (Phase II goal)                    |

(c) Lifetime >10 days continuous.

Given the need for batteries, modulation electronics, chemical sensors and filtration, the total space available to the pumps is about  $2.5 \text{ cm}^3$ .

## **2.2 General Considerations: Inertial vs. Displacement Pumps**

Most pumps are either of displacement or inertial types. Examples of displacement pumps are pistons, bellows and peristaltic mechanisms. Inertial pumps include fans and turbo-molecular pumps. A key consideration is the Reynolds number regime of the flow required. Reynolds number is a dimensionless quantity that provides a good estimate of the ratio of inertial to viscous forces. It is expressed in terms of viscosity,  $\eta$ , and density  $\rho$ , of the fluid, as well as a characteristic viscosity,  $v$ , and length scale,  $l$ ,

$$R = \frac{\rho v l}{\eta} \quad . \quad 1$$

Reynolds number of 1 or less indicates a very viscous regime in which inertial mechanisms are ineffective. The relation can be expressed in terms of flow rate,  $Q$ ,

$$R = \frac{\rho Q}{\eta l} \quad . \quad 2$$

The viscosity of air at standard temperature and pressure (STP) is  $1.8 \times 10^{-5} \text{ N} \cdot \text{s} \cdot \text{m}^{-2}$  and the density is  $1.2 \text{ kg/m}^3$ . Given a nominal flow rate of  $Q = 10^{-8} \text{ m}^3/\text{s}$  ( $0.6 \text{ cm}^3/\text{min}$ ) and a length scale,  $l = 10^{-2} \text{ m}$ , as determined by pump dimensions, the Reynolds number is 0.007. Clearly inertial pumps are not practical for the specified flow rates and pump dimensions.

### **2.3 Pump design and actuator properties**

The pump specifications have been set out in section 2.1. These are now related to the measured conducting polymer material properties, the details of measurements being described in Section 3. Finally, the characteristics of a conducting polymer driven pump are listed.

A bellows design is chosen for analysis. This form of displacement pump involves an inlet and outlet, each with valves. The stroke cycle begins with the inlet valve open, the outlet closed and a

piston moving to increase chamber volume and draw air in. The inlet is then closed, and a compression stroke begins in which air is forced out the outlet. In the bellows design the seal between the piston and the chamber is made via a compliant membrane. Friction is low, increasing efficiency. Flow rate is determined by the piston stroke volume and the rate of cycling.

Can conducting polymers meet the required pump specifications? From bilayer studies, it initially appeared that the required performance was well within the capabilities of the conducting polymers made in our laboratory. However, proper analysis of the bilayer film data depended upon a knowledge of the stiffnesses of the component film. Furthermore, these films were often somewhat non-uniform in thickness, leading to twisting and bending that made results more difficult to quantify. Furthermore bilayers generate large displacements, but correspondingly small forces. The pressure requirements on the pump are significant, and making a stand alone fiber or film contractile actuator more appropriate. For these reasons, studies were undertaken of stand alone films. The results from section 3 are summarized as follows:

<i>Property</i>	<i>Measured</i>	<i>Required Minimum</i>
1. Stress	5 MPa	0.015 MPa
2. Strain	2 % typical	
3. Cycles per Minute	1.5 (film), 600 (bilayer)	1.0 (film)
4. Strain/Charge	$1.2 \times 10^{-10} m^3/C$	
5. Power Density	1.5 kW/kg	
6. Cycle Life	< 7 000 @ 2% strain	15 000

Given a pump cross-section of about  $2.0 \text{ cm}^2$ , and a cycle rate of 1 RPM, the displacement required to pump  $0.1 \text{ cm}^3/\text{min}$  is  $0.5 \text{ mm}$ . Choosing a conservative stress and strain of 5 MPa and 1% to reduce plastic deformations in the polymer, the pump requires actuator dimensions of  $2 \text{ mm}^2$  in cross-section and  $50 \text{ mm}$  in length, consuming a volume of  $0.1 \text{ cm}^3$ .

The cycle life must be at least 15,000 assuming continuous operation for a ten-day period. While relatively long lifetimes were obtained at 3 Hz operation ( $>200\,000$  cycles), this was achieved

for strains of less than 1%. For larger strains, performance degraded over time thus additional data is required at intermediate strains and stresses to estimate actuator performance in this strain regime.

Should lifetime prove to be a problem, two remedies are very promising for the next phase of research. Strain can be further reduced, at the cost of increasing the actuator size. Given that the pump size is only  $0.1 \text{ cm}^3$ , even a tripling in size would keep the volume well within the specified limits. The second option is to stretch align the film, which increases stiffness ( $30 \text{ GPa}$ ) and tensile strength ( $300 \text{ MPa}$ ), and drastically reduces plastic deformation. While strains are reduced to a level of about 1%, as observed in polyaniline, the stresses may reach  $100 \text{ MPa}$ . Note that the first remedy implies an increase in the amount of actuator material required, and therefore the space occupied. The second requires less material due to the increase in force per cross-sectional area.

Another issue is the power consumption. The first generation of actuators will run off batteries, likely high energy density lithium polymer cells ( $1 \text{ MJ/kg}$ ). From the strain/charge ratio and the polymer volume, the charge per cycle is determined. It corresponds to a battery consumption of  $100 \text{ g/day}$ .

Two approaches will reduce battery consumption. Firstly, more than 90% of the electrical energy input is recoverable. Essentially, the actuator is a battery itself. The consumption then becomes less than  $10 \text{ g/day}$ . Furthermore, by using many small parallel fibers, the surface area to volume ratio is improved, mass transport rate increases, and the overpotential required to run the batteries will drop, likely to near the equilibrium potential of less than  $1 \text{ V}$ . Battery consumption will then drop further, to  $2 \text{ g/day}$ .

Listed below are properties of the displacement pump described. Version 1 consists of the actuator film as measured. In Version 2, a stretch aligned film is assumed, along with energy recovery. Also assumed for Version 2 is a higher bandwidth and lower activation voltage due to an increased surface area to volume in the actuator. The numbers employed for both versions are fairly conservative estimates of what can be achieved.

<i>Property</i>	<i>Version 1</i>	<i>Version 2</i>
Flow Rate	0.1 cm <sup>3</sup> /s	0.1 cm <sup>3</sup> /s
Pump Volume	0.2 cm <sup>3</sup>	0.003 cm <sup>3</sup>
Actuator Volume	0.1 cm <sup>3</sup>	0.002 cm <sup>3</sup>
Maximum Pressure	20 kPa	20kPa
Pump Frequency	1 RPM	1 Hz
Applied Voltage	4.5 V	1 V
Battery Consumption	100 g/day	2 g/day

The following section describes the characterization of the conducting polymer actuators, which provided the data to determine pump characteristics. The report concludes with a demonstration of two displacement pump designs, namely bellows and peristaltic. These employ shape memory alloy fibers, which are the only other actuators to share similar contractile characteristics with conducting polymers.

## 3.0 Conducting polymer actuators

The bulk of the results pertaining to conducting polymer actuators are presented. In particular, it is shown that stress and strain are related to charge transferred, and the mechanical properties of the polymers are determined, passive and active. Also, the operation of polymer actuators outside a liquid environment is shown. First, though, an overview of conducting polymers is given, followed by a comparison of conducting polymer actuator characteristics with those of other actuator technologies, motivating the use of conducting polymers.

### 3.1 *Conducting polymers – general characteristics*

Nature employs organic materials to fabricate highly complex nano-systems. Twenty-two amino acids, four ribonucleases, one basic lipid structure and one basic sugar structure, all immersed in aqueous salts, form a relatively small basis set from which nearly all of life is constructed. A few conducting polymers combined with ionic salts, either in a liquid or solid solution, can form a similarly diverse basis set. Figure 3 lists just some of the devices possible using conducting polymers. In fact, using either polyaniline or polypyrrole, which are the two best characterized conducting polymers, all of these devices can be built as variations of one of these materials. Many polymeric fabrication techniques are well-suited for construction of devices on the micro and/or nanoscale in addition to allowing co-fabrication of integrated microsystems.

Conducting polymers are also called conjugated polymers as they are characterized by a conjugated backbone structure, represented by alternating single and double bonds. The structure of some of the most common conjugated polymers, including polyaniline and polypyrrole, are shown in Figure 4.

The conjugation of the backbone allows the delocalization of electrons along the backbone and hence some degree of conductivity. In their undoped form, these molecules are semi-metals, as delocalization is incomplete. Upon doping,

- ◆ **Actuators**
- ◆ **Wire (cf Cu)**
- ◆ **Transistors**
- ◆ **Sensors**
  - chemical (noses)
  - force, length
- ◆ **Batteries (...)**
- ◆ **Capacitors**
- ◆ **Memory**
- ◆ **Light emitting diodes**
- ◆ **Photodetectors & cells**
- ◆ **Electrochromic displays**
- ◆ **Drug delivery systems**
- ◆ **EMI shielding**
- ◆ **Electrorheological fluids**
- ◆ **3D co-micro-fabrication**

**Figure 3:** Some applications of conducting polymers.

dopant ions migrate into or out of the bulk polymer and affect the electronic state) a conductive state is achieved. Conductivities up to a third that of copper have been reported<sup>3</sup>. Note that in many instances, the doping is reversible – for polymers in a solution, ions that migrate into the polymer can also migrate back to the solution. Changes with doping level of properties such as conductivity are therefore also reversible.

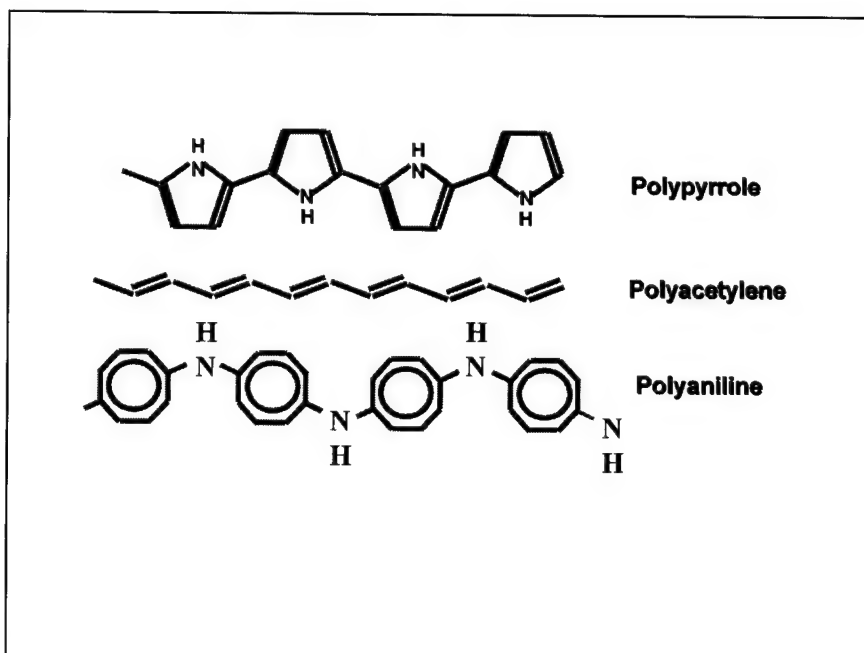


**Figure 4:** Schematic showing bond structure of three conducting polymers. We used polypyrrole and polyaniline conducting polymers in our actuator studies.

Conducting polymers exhibit other properties valuable to the micro-system designer. By changing the doping level, which in turn changes the oxidation state of the polymer, conductivity can be switched by 11 orders of magnitude, an effect that has been employed to build supercapacitors and *k*Hz frequency transistors<sup>4</sup>. Conducting polymer blends have been made into high efficiency photosensors and photoemitters. High energy density batteries, about 1 *MJ/kg*, employ the high-density ion storage properties of conducting polymers (c.f. lead acid batteries at 0.15 *MJ/kg*). Finally, several of these materials are biocompatible. Polypyrrole, for example, is

<sup>3</sup> Roth, Siegmar, One-dimensional Metals, Springer-Verlag; New York, 1995.

<sup>4</sup> Jones, E.T.T. et. al., “Preparation and characterization of Molecule -based transistors with a 50-nm source-drain separation”, J. American Chem. Soc., V. 109, pp.5526-9, 1987.

being used to guide nerve regeneration<sup>5</sup>. Note that the range of devices constructed using conjugated polymers, as listed in Figure 3, covers the range of sub-systems sought in an autonomous micro-mechanical device, namely energy storage and delivery, actuation, sensation, intelligence, and communication.

### 3.2 Conducting Polymer Actuators

Volume changes associated with changes in oxidation state brought about by the corresponding doping or undoping of the polymer by mobile ions is a proposed mechanism underlying conducting polymer actuators (Figure 5). Baughman *et al.*<sup>7</sup> demonstrated with diffraction techniques the volume changes result from inclusion of dopant ions between polymer chains. Such volume changes are typically about 10%, but can be as high as 200%<sup>8</sup>. For small

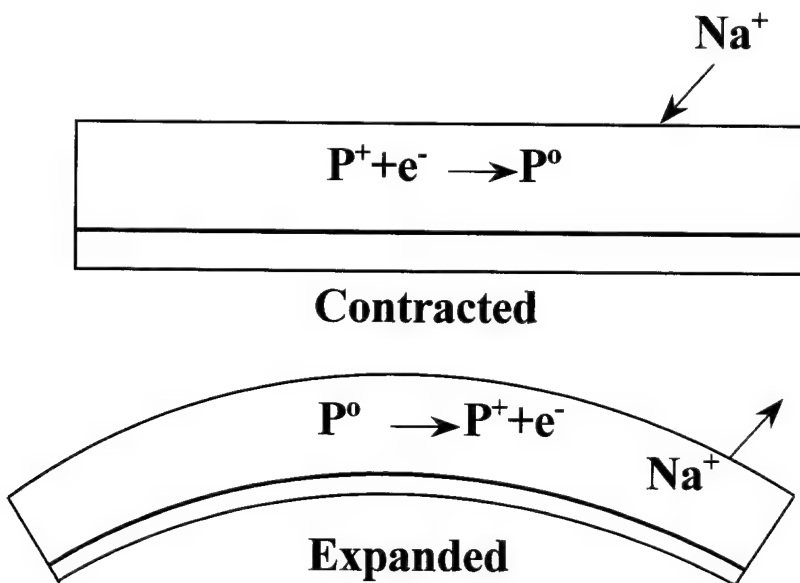


**Figure 5:** Schematic showing mechanism responsible for volumetric change in conducting polymers<sup>6</sup>.

<sup>5</sup> Shastri, V.R. et al. “polypyrrole – a potential candidate for stimulated nerve regeneration” manuscript, 1996.

<sup>6</sup> Smela, E. Inganäs, O. and Lundstrom, I “Controlled folding of micrometer-size structures”, Science, 268, pp.1735-1737, 1995.

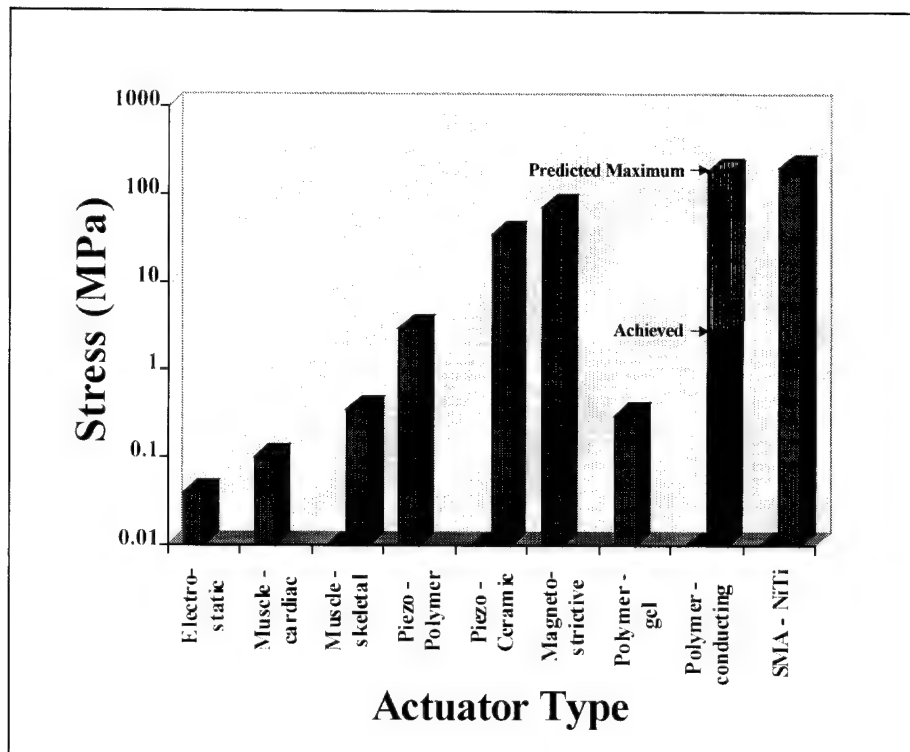


**Figure 6:** Comparison of maximum stress generated by different actuator types. Note the predicted maximum stress for conducting polymers exceeds that possible with other actuators considered except for shape memory alloys.

strains, typically 0.5%, most of the volume change occurs along the chain backbone. Thus, potentially much higher stresses can be generated in conducting polymers whose chains are preferentially oriented in one direction. Chain alignment can also result in anisotropic material properties of which advantage can be taken, if for example, uniaxial strain is required in a given actuator application.

Properties relevant to actuator performance are grossly divided according to whether they are static or dynamic in nature. Static properties include the maximum stress or strain developed by the actuator such that it does not suffer permanent deformation. Dynamic properties include strain rate, power per unit mass and electro-mechanical conversion efficiency (e.g. conversion efficiency of electrical energy in to output mechanical work). These properties are important in the selection of an actuator mechanism and pumping scheme that takes greatest advantage of the characteristics inherent to a given actuator type. For example, to achieve a specified mass flow

---

<sup>7</sup>Baughman, R.H., "Micro Electromechanical Actuators based on conducting polymers", Molecular Electronics, P.I.Lavarev Ed, Kluwer: Nederlands, pp.267-289, 1991.

rate, an actuator capable of a high repetition rate at small displacements and forces could result in a pump design very different from one that utilizes an actuator operating at low repetition rates but generating large displacements and forces. The actuator's electro-mechanical efficiency (electrical energy consumed per unit of mechanical work) determines many system level factors such as energy source for powering the pump and can, accordingly, ultimately impact on the pump's portability.

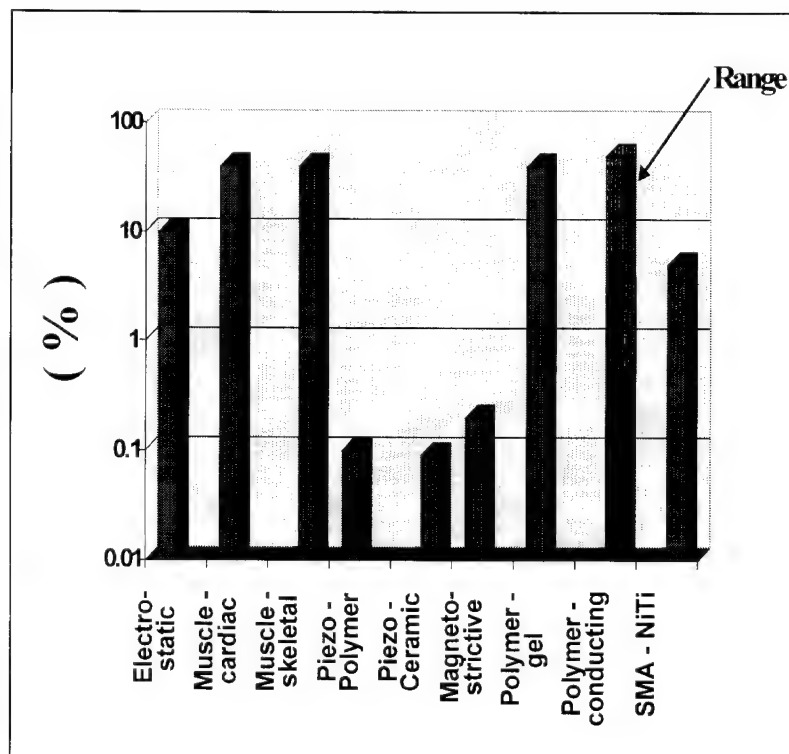


**Figure 7:** Maximum strains reported for different actuators. Note that in the case of conducting polymers it is predicted that the maximum strain can vary over a large range because of its dependence on the specific polymer configuration (e.g. morphology, dopant ion, etc.).

These characteristics are now discussed in greater detail and related to properties of other types of actuators including Nature's ubiquitous actuator, muscle<sup>9</sup>. As the field of polymer actuators is relatively new, and actuators have only been built in the last several years, both the measured performance to date and the anticipated properties are shown.

<sup>8</sup> Baughman, R.H., "Conducting Polymer Artificial Muscles", *Synthetic Metals*, Vol. 78, pp.339-53, 1996.

<sup>9</sup> Hunter I.W. and Lafontaine S.R. "A comparison of muscle with artificial actuators" Technical Digest of the 5<sup>th</sup> IEEE Workshop on Solid State Sensors and Actuators, 5, pp. 178-85, 1992.

### 3.2.1 Force per Cross-sectional Area

Force per cross-sectional area, equivalent to the stress or pressure generated by an actuator, is a measure of force that is independent of scale. For micro-systems, where reduction of size is essential, high force per cross-sectional area is clearly desirable.

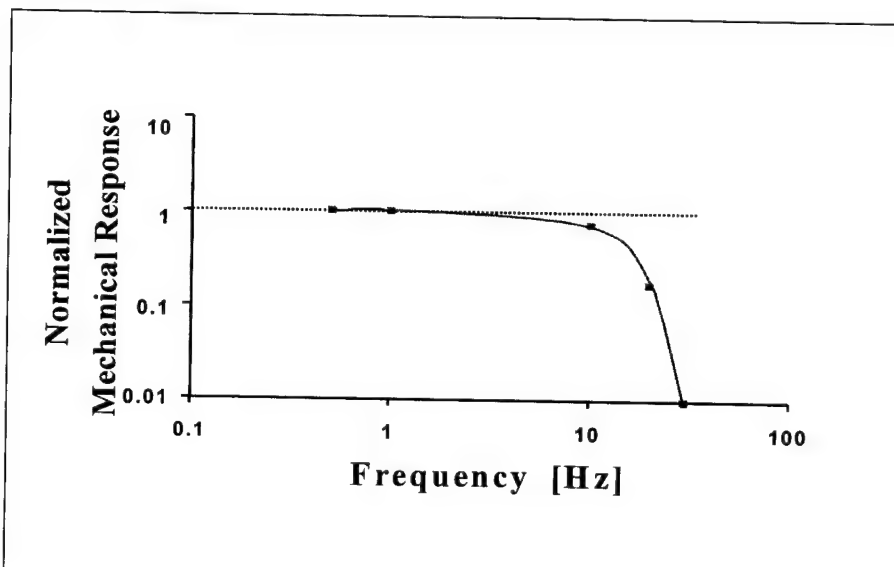


**Figure 8:** Conducting polymers have high strain rates as indicated by the high roll-off frequency of the mechanical frequency response of an electrically-activated conducting polymer bilayer.

Figure 6 compares force per cross-sectional area for a number of actuation mechanisms, based on data from Hunter and Lafontaine<sup>9</sup>. Conducting polymers are predicted to generate forces per cross-sectional area comparable to shape memory alloys, and stress far greater than other actuators such as piezo-electrics (50 ×), mammalian muscle (600 ×) and electro-static actuators (10 000 ×). Note that the data presented in the plot represents an estimate of polymer performance based on what is effectively the yield stress in these materials. The achieved stress measurements shown in Figure 6 are those reported in this report and are, to our knowledge, the first such measurements of their kind made on conducting polymer actuators. We were able to generate with free-standing films immersed in electrolytic solution stresses greater than 5 MPa. This stress level is matched only by piezo-polymers, magneto-strictive alloys and shape memory alloy actuators, the first two of which are limited in the strain they can produce. Further

processing of the polymer by stretch alignment can yield much larger forces perhaps even up to the tensile strength of the material.

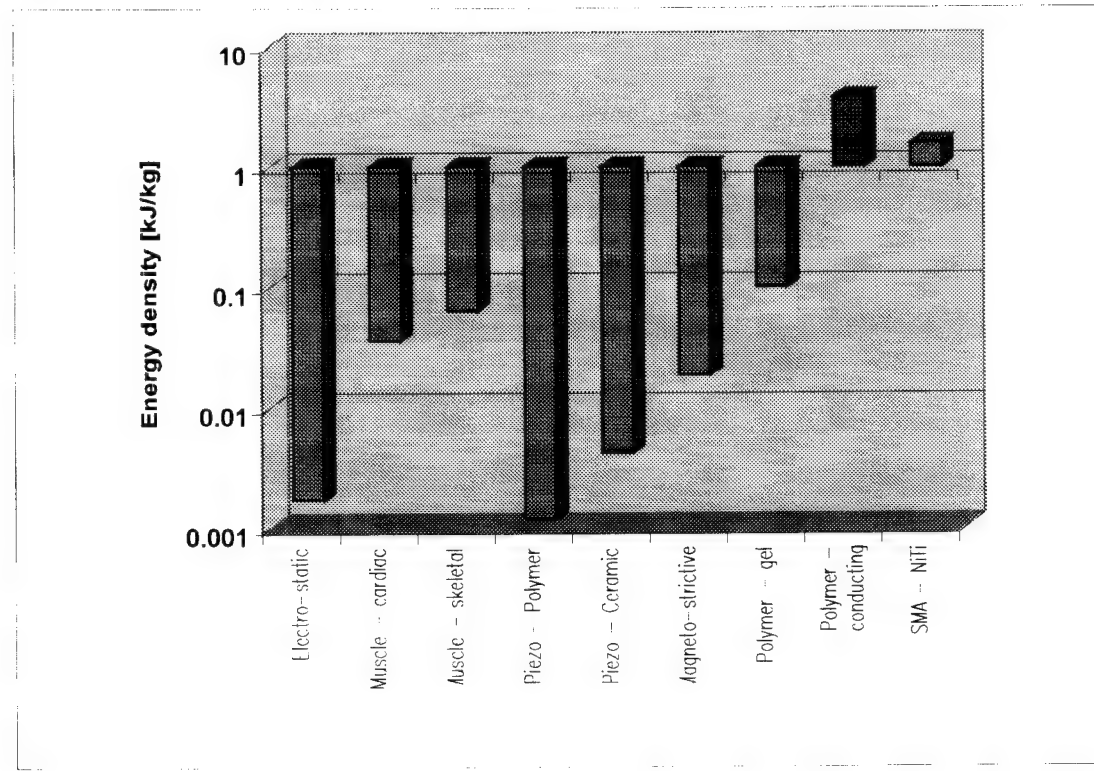


**Figure 9:** Comparison of energy densities produced by different actuator types. The achieved energy density for conducting polymers is rather low (comparable to polymer gels and skeletal muscles) but the predicted energy densities based on improved materials is several orders of magnitude greater than most other actuators listed.

### 3.2.2 Strain

Figure 7 compares typical strains of a number of actuator technologies. Note that there is a wide range of strains given for the conducting polymers. Strain is dependent on polymer morphology and the nature of the dopant ions inserted. If the dopant ions are small and mainly affect chain length, then strains are only approximately 0.5%. Often dopant ions will create spaces between chains and if solvent molecules enter the polymer along with the dopants then volume changes can be up to 100% or more, although typically volume changes are about 10%. Very little is known about the constitutive relationship governing stress and strain in conducting polymers. One aspect is clear, however, in that large strains generate kinks in the polymer

backbone, which in turn reduce the stress produced. In the polymer actuators investigated in this report, the strains observed are about 2%.

### 3.2.3 Strain Rate

Strain rate is a function of how rapidly dopant can enter or exit the polymer. The time constant for mass transport by diffusion,  $\tau$ , is proportional to film thickness squared,  $L^2$ , and inversely proportional to the diffusion coefficient,  $D$ :

$$\tau \propto L^2 / D$$

3

We have observed have observed time constants as small as 0.1 s for 30-60 micrometer thick films (Figure 8), with some motion being observed at frequencies up to 60 Hz. The effect of film thickness on doping rate has been demonstrated in electrochromic devices and transistors, which

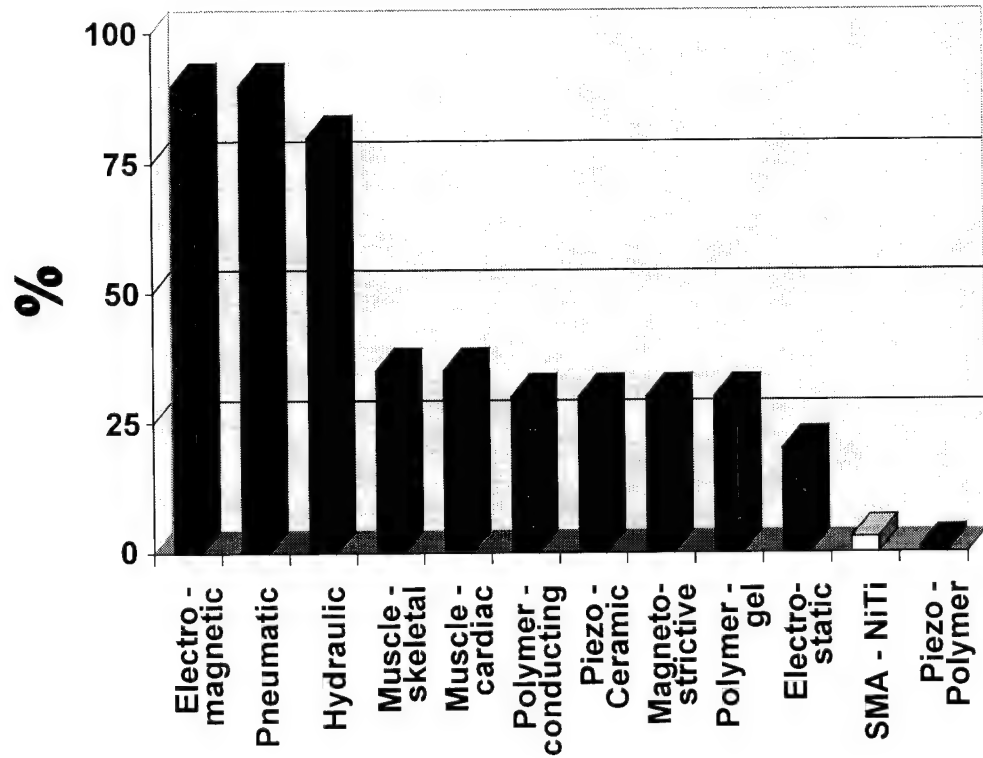


**Figure 10:** Comparison of electro-mechanical efficiencies across different actuator types. With electrical energy recovery, the conversion efficiency of conducting polymers can be quite good.

can operate up to frequencies of 10 kHz. As the force generated is a function of the cross-sectional area of the film, decreasing the film thickness will decrease the force generated, all else remaining constant. By employing many thin fibers in parallel, as in muscle, a large cross-sectional area with short diffusion lengths can be constructed to produce fast responses and large forces.

### 3.2.4 Energy Density, Efficiency and Power Density

Mechanical energy density is defined as the amount of work that can be performed per unit mass of material. This quantity should be large to minimize the volume of actuator needed to achieve a certain pumping performance. Figure 9 compares this parameter across different actuator technologies. We have included in this plot our results -the first measurement of this quantity for conducting polymer actuators- at 8 KJ/kg.

Actuator efficiency is the ratio of work done by the actuator to the energy input to the actuator. Defined in terms of stress,  $\sigma$ , strain,  $\varepsilon$ , applied voltage,  $V$ , and current per unit volume,  $j$ , the efficiency,  $\beta$ , is written as,

$$\beta = \frac{\int \sigma d\varepsilon}{\int V j dt} \quad 4$$

Currently conducting polymer actuators exhibit efficiencies of less than one percent. However, much of the energy expended is recoverable because the reduction-oxidation (reoxd) cycling of conducting polymers is, in effect, charging and discharging of a battery. Battery technology based on conducting polymers achieves efficiencies of up to 99%. Thus, it is simply a matter of devising a suitable scheme to recover the energy presently dissipated in the polymer through ohmic loss.

Power density is a final actuator characteristic of importance because it is a normalized parameter that quantifies the amount of mechanical power generated by the actuator. For a pump actuator, this must be large to overcome the inertial and viscous forces inherent to imparting

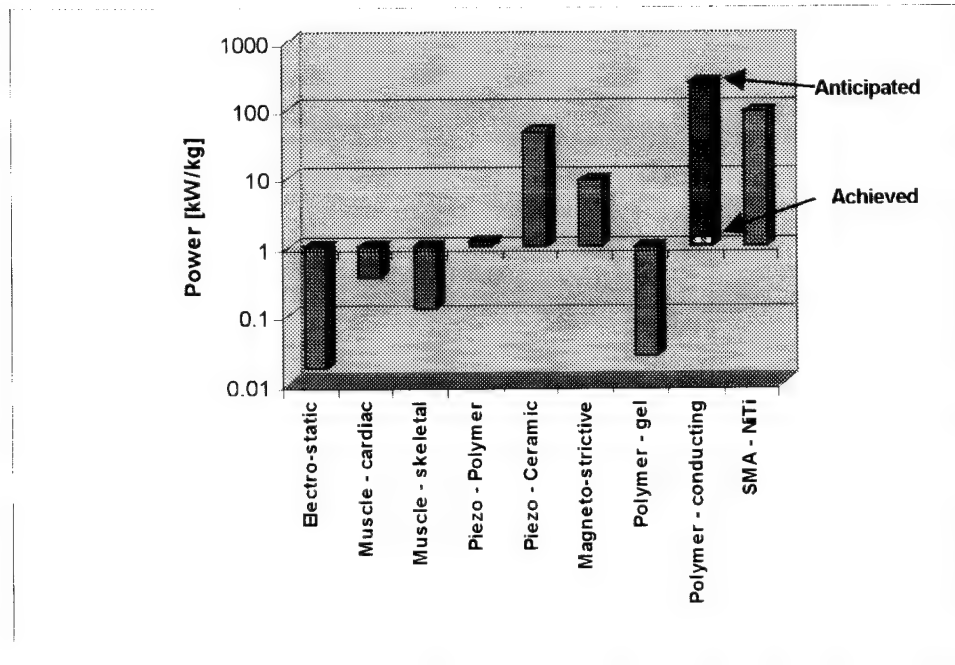


**Figure 11:** Power density comparison across different actuator types.

motion to a liquid or gas. As plotted in Figure 11 for different actuator technologies, the power density of conducting polymers is at present quite low. However, improvements in electro-mechanical efficiencies suggests a power-to-mass ratio potentially comparable to SMAs. The theoretical power-to-mass ratio is based on the predicted stresses (Figure 6), a 2% strain and a strain rate of 2 Hz (i.e. for a 2% strain a 100 Hz oscillation).

### 3.3 Conducting Polymer Actuator Theory, Experiments and Results

In the application of conducting polymers as pump actuators, it is essential for the system designer to know basic properties such as stress, strain, lifetime, efficiency, applied voltage, current, and frequency response. These properties are investigated here, beginning with a discussion of the underlying mechanisms of activation and followed by models of conducting polymer active and passive

passive response relevant to their application as pump actuators. Experimental measurements are next given and analyzed within the context of these models to establish the phenomenological relationships between electrical input (charge) and mechanical output (stress and strain) as functions of material formulation and fabrication.

### 3.3.1 Contraction mechanisms

Several mechanisms have been proposed to explain the expansion and contraction of polyaniline and polypyrrole films as their oxidation potentials are varied. These include changes in intermolecular spacing due to electrostatic repulsion, change in bond length along the polymer backbone or different molecular conformations in the reduced and oxidized states. However, the experimental evidence suggests that in polypropylene, employed in the work presented here, the most likely explanation is that changes in intermolecular spacing –and hence volume- results from the insertion of charged ionic or solvent species into the polymer. X-ray diffraction studies by Yamaura *et al.*<sup>10</sup> on polypyrrole films grown under the same conditions as those presented in this study show a fairly linear increase in molecular spacing as a function of the anion employed during electrochemical synthesis. The work of Pei<sup>11</sup> and his colleagues also suggests that volume changes in polypyrrole are ionically induced. They show that using the combination of a very large anion and a small cation, oxidation induces contraction in the polymer. When very large cations are employed, along with small anions, oxidation results in expansion. It seems that the large cations and anions are too large to move in and out of the material. Small ions can, however, and charge balance is maintained. Upon oxidation, the polymer backbone becomes relatively more positively charged, and hence either cations must leave or anions enter. In the case of large anion/small cation, cations leave, resulting in contraction, and vice versa for the large cation/ small anion case. No quantitative data is available relating volume changes to the dimensions of the mobile ion. However, it appears that ions can affect at least the direction of contraction and expansion and are therefore central to the actuation process in polypyrrole.

---

<sup>10</sup> Yamaura, M, Hagiwara, T., and Iwata, K. "Enhancement of electrical conductivity of polypyrrole film by stretching: counter ion effect", *Synthetic Metals* 1988, 26, p.209-224.

<sup>11</sup> Pei, Quibing and Inganás, Olle, Electrochemical Muscles, *Synthetic Metals* 55-57 (1993) p.3718-3723.

Counter to this line of experimental evidence runs the work by Herod<sup>12</sup> and Kaneto<sup>13</sup> on the measurement of strain as a function of dopant ion size in polyaniline. Kaneto claims some change in strain as a function of anion size for a give change in oxidation state. The trend with anion ion size, however, is weak at best. Herod states that there is no perceptible difference between the total extent of elongation when using three acids, namely HCl, HF and HClO<sub>4</sub>. X-ray diffraction studies appear to confirm that the extent of expansion/contraction is significantly larger than can be explained by anion size alone. There may be solvent entrained into the material, or electrostatic repulsion may be responsible for the strains observed.

Evidently further study is required to elucidate the mechanisms in both polyaniline and polypyrrole. It is clear, however, that at least in polyaniline, expansion and contraction is directly proportional to charge injected into the polymer. This result has important implications for modeling of the active behavior of the polymer, as well as for control. A direct relationship between charge and strain makes the polymer behavior readily predictable.

### 3.3.2 Film Modeling: Mechanical Response

To begin, it is useful to have some grounding in models that might describe polymer behavior. This is important in order to, first, understand the mechanisms of actuator operation and, second, utilize this knowledge to fabricate conducting polymer actuators exhibiting predictable and reproducible behavior so that they can eventually brought under servocontrol to further improve the actuator performance.

The polymer electro-chemo-mechanical response is complex as evidenced by the many variables in the constitutive law governing stress in a conducting polymer. These include strain, strain rate, electrochemical state, anion/cation/solvent concentration, temperature and history. Other properties dictating the conducting polymer response to electrochemical activation include its diffusion coefficient, electrical conductivity, reduction potentials of the oxidation states, and elastic modulus

---

<sup>12</sup> Herod, T.E. and Schlenoff, J.B. Doping-Induced Strain in Polyaniline: Stretchelectrochemistry *Chemistry of Materials* 1993 5 951-955.

<sup>13</sup> Kaneto, K. Kancko, M. Min, Y. and MacDiarmid, A.G. Artificial Muscle: Electromechanical actuators using polyaniline films *Synthetic Metals* 1995b 71 2211-2212.

and Poisson's ratio among other mechanical properties. In this section a theoretical framework is developed for the understanding of polymer behavior as a function of these variables.

The passive material response is first analyzed. The passive response is the behavior of the actuator as a function of applied stress and strain, without any applied electrical potential. It is an important part of the overall response. For example, creep and stress relaxation may occur due to plastic deformations of the material. Knowledge of the extent of these effects is crucial in determining actuator lifetime and the range of stresses that can be withstood without major deformation. Tensile strength is also clearly relevant as it sets the absolute maximum applied stress that can be withstood by the material.

Active response is then modeled. The aim is a relationship between stress and strain as a function

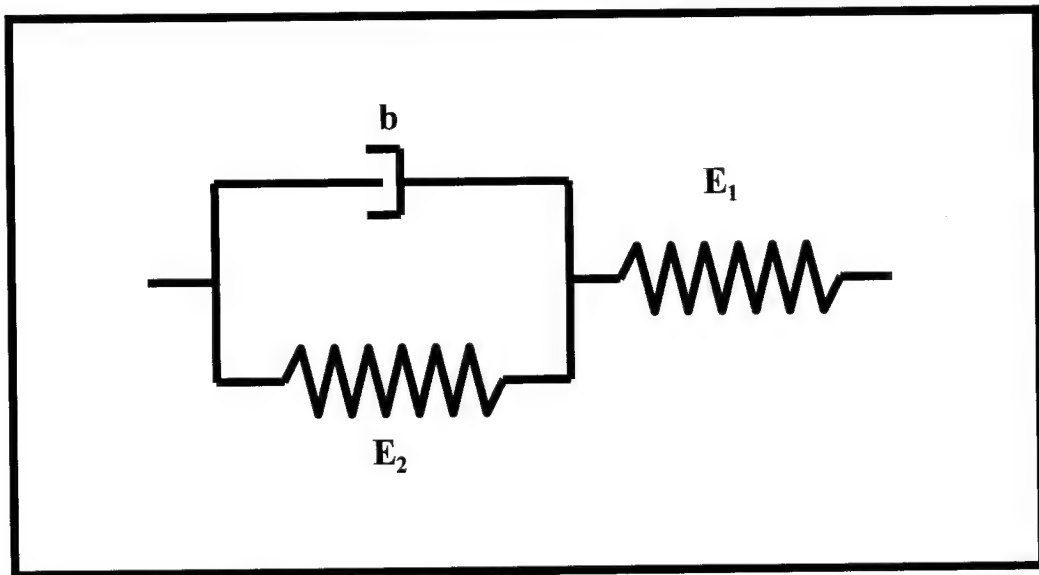


**Figure 12:** Schematic depicting the standard linear network mechanical model used to model the passive mechanical behavior of a conducting polymer.

of charge and the passive mechanical properties. Such a relationship allows the prediction of mechanical behavior under all load and charge conditions.

### 3.3.2.1 Passive Response

In this section, a qualitative model of polymer passive response is given. This model helps to explain the importance of the passive properties to overall actuator and pump behavior. Such response often determines the success or failure of load bearing structures fabricated from polymers.

As a first order attempt to model polymer characteristics, a standard linear network model is presented to describe the response to a ramp in strain, under passive conditions. (Note that passive conditions imply there is no change in oxidation state.) Given that the polymer exhibits visco-elastic behavior, a spring (elastic modulus  $E_1$ ) in series with parallel spring ( $E_2$ ) and damper ( $b$ ), is used to model the constitutive behavior. Such a constitutive relationship, shown in Figure 12, is a widely used approximation to describe many polymer systems at temperatures below their glass transition point. The constitutive equation is written,

$$\sigma \left[ 1 + \frac{E_2}{E_1} \right] + \frac{b}{E_1} \dot{\sigma} = E_2 \varepsilon + b \dot{\varepsilon}, \quad 5$$

where  $\sigma$  is stress,  $\varepsilon$  is strain and the dots represent time derivatives.

When a step in strain is applied, the stress response takes on the form,

$$\frac{\sigma(t)}{\varepsilon} = \frac{E_1^2}{E_1 + E_2} e^{\frac{-E_2 t}{b}} + \frac{E_1 E_2}{E_1 + E_2}. \quad 6$$

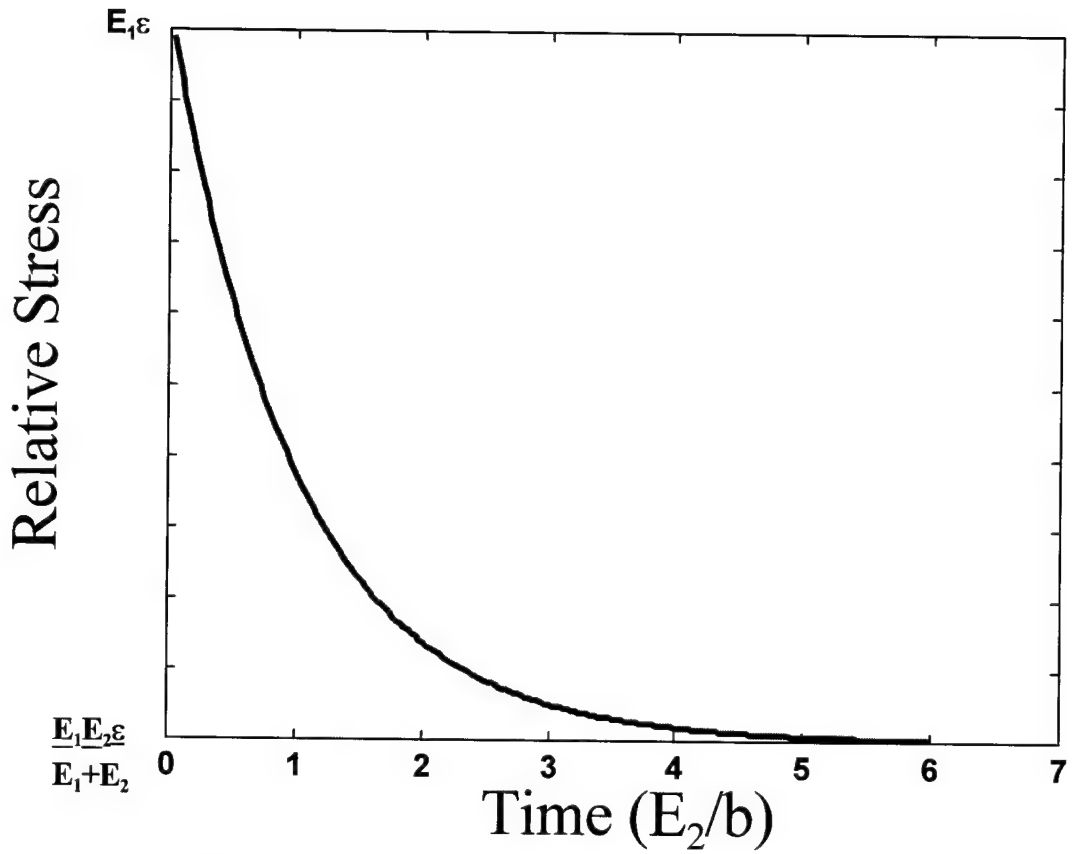


**Figure 13:** Stress relaxation in response to a step in strain (Equation 5).

Figure 13 plots the stress relaxation predicted from Equation 5 that occurs in response to a step in strain. Note that in extreme cases, stress can relax many tens of percent of total stress over seconds or minutes. It is thus important to determine the time constant and the magnitude of relaxation. If such relaxation is significant, measures must be taken either to change the material processing, model the behavior such that these effects can be compensated for, or introduce compensating feedback on stress and/or strain to minimize this effect. It should also be noted that the behavior shown in Figure 13 is not unique. The constitutive relationship represented by the model shown in Figure 12 may, for example, also include a further damping element in series, and hence continuous relaxation with an asymptote at zero stress.

Rather than apply a step stimulus to the polymer, an alternative is to apply a ramp stimulus with the applied strain expressed in terms of strain rate,  $\gamma$ ,

$$\varepsilon(t) = \gamma t,$$

7

and the ramp response is found by simply taking the integral of the step response (Equation 6). For stain that increases with time, the stress is calculated to be ,

$$\sigma(t) = \frac{E_1}{E_1 + E_2} \left[ \frac{E_1 b \gamma}{E_2} \left( 1 - e^{-\frac{E_2 \varepsilon}{b \gamma}} \right) + E_2 \varepsilon \right], \quad 8$$

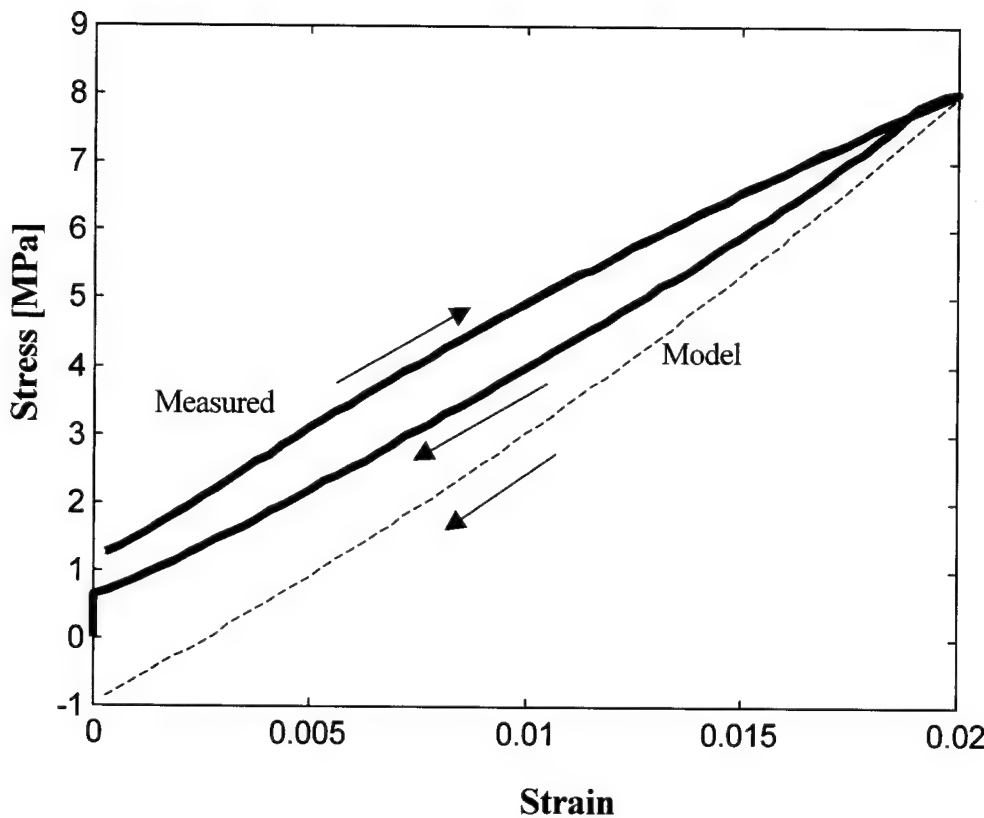


**Figure 14:** Passive stress-strain curve for a polypyrrole film in a propylene carbonate electrolyte. The film is subjected to a strain rate of 0.0012Hz. The dark line indicates the measured value while the dashed line is a fit to the passive model (Equation 3).

and when the strain decreases with time from a maximum strain,  $\varepsilon_o$ , the resulting stress is,

$$\sigma(t) = \frac{E_1}{E_1 + E_2} \left[ \frac{E_1 b \gamma}{E_2} \left( -2e^{\frac{E_2(\varepsilon - \varepsilon_o)}{b \gamma}} + e^{\frac{-E_2(2\varepsilon_o - \varepsilon)}{b \gamma}} - 1 \right) + E_2 \varepsilon \right]. \quad 9$$

The response predicted by Equations 7 and 9 is compared with experimental measurement in Figure 14 for both increasing and decreasing strain with time. The theoretical prediction for increasing strain compares well with the experimental measurement (the theoretical curve is hidden under the experimental result for increasing strain) but substantially underestimates the stress as the strain decreases with time. This difference is caused by stress relaxation in the polymer and appears as a hysteresis in the stress-strain measurement. However, this is not in fact true hysteresis, but rather is dependent on the rate of activation (strain rate). Note also that the model does not account for the fact that a laterally unconstrained film will not exert negative stresses. These shortcomings will be further discussed in the experimental section. Polymers often display visco-elastic behavior that qualitatively follows Equation 3, but is in fact non-linear and very difficult to model. This makes the option of model-based compensation for plastic deformation unrealistic. If plastic deformation is large, either new methods of synthesis must be found, or feedback compensation should be employed.

Equations 5 through 9 provide a qualitative mathematical description of the polymer's passive mechanical behavior under applied strain. Relaxation and creep are major concerns in the design and implementation of any polymer load bearing structure. For this reason, experimental results showing passive response, in addition to active behavior, are treated in some detail below.

### 3.3.2.2 Modeling Active Response

The expansion or contraction of the polymers can be related to charge transfer in much the same way as thermal expansion is related to temperature by making the following assumptions:

- Expansion is proportional to the charge transfer,
- Volume change is directly proportional to the magnitude of charge transfer, and
- $N$  species of ion are present which are capable of entering or leaving the material, and these ions in turn are responsible for expansion and/or contraction.

In such cases, the strain due to the injection or removal of species at any given time is,

$$\varepsilon = \frac{\sigma}{E} + \sum_{i=1}^N \alpha_i Q_i , \quad 10$$

where,  $\alpha_i$ , is the linear coefficient of ionic expansion for a given influx of ions of the type denoted by,  $i$ , whose charge is  $Q_i$ . Here we have made the further assumption that the time constant of activation is short relative to time constants for creep and relaxation. The constitutive model depicted in Figure 12 is replaced by a single spring of modulus  $E$ . As will be shown in the experimental section, this is a reasonable approximation, provided that stress is not maintained for long periods of time. This is the case for pumps, where high levels of stress are experienced only during the relatively brief compression stroke.

Neglecting the initial capacitive charging that occurs in electrochemical cells, the relationship between the applied current,  $i$ , and the total charge transferred is,

$$i = \frac{d}{dt} \sum_{i=1}^N Q_i . \quad 11$$

If we now assume that only one ion is being transported into and out of the polymer,

$$\varepsilon = \frac{\sigma}{E} + \alpha Q . \quad 12$$

Such a situation will occur if the anion in a two component solution is much larger than the cation, or vice-versa, and therefore the larger ion is not transported at all, or at a much lower rate. Note also that, while the model has been explained in terms of ionically induced expansion, all hypothesized mechanisms involve charge transfer of some form, and hence Equation 12 is not subject to the choice of any particular hypothesis.

Clearly, Equation 12 can be rearranged to express stress in terms of strain and the coefficient of ionic expansion,

$$\sigma = E\varepsilon - E\alpha Q . \quad 13$$

Since charge is simply the integral of current over time, the time dependence of stress and strain can be expressed in terms of the current,

$$\varepsilon = \frac{\sigma}{E} + \alpha \int i dt , \quad 14$$

and,

$$\sigma = E\varepsilon - E\alpha \int idt . \quad 15$$

Under galvanostatic conditions (constant current), stress and strain are linearly proportional to time,

$$\varepsilon = \frac{\sigma}{E} + \alpha it . \quad 16$$

One might expect that at a sufficiently high frequency, when the mass transfer does not have a chance to reach equilibrium and capacitive effects dominate, this relation would no longer hold. In addition, at some point the mass transfer rate will not be able to maintain the current, and other reactions will be initiated as the voltage increases to maintain current. At this point, other ions will be involved, which may act with or against the initial linear expansion. Finally, mechanical resonances may restrict the frequency range over which this equation is valid.

For potentiostatic conditions (constant applied voltage), current is no longer constant. For example, under conditions of diffusion limit, where the electrode forms an effective surface (as opposed to a porous structure), and current is proportional to the inverse square root of time,

$$i = gnFACD^{1/2}t^{-1/2} , \quad 17$$

where  $D$  is the diffusion coefficient,  $C$  is bulk concentration,  $A$  is the area of the electrode,  $F$  is Faraday's constant and  $g$  is a factor related to electrode geometry. This relationship, known as the Cotrell equation, holds reasonably well for porous materials also. Substituting Equation 17 into 15 and integrating it is clear that stress and strain will increase as  $t^{1/2}$ . The induced strain amplitude as a function of frequency,  $f$ , is therefore,

$$\varepsilon = \frac{\sigma}{E} + \alpha gnFACD^{1/2}f^{-1/2} . \quad 18$$

Mass transport is nearly always the rate limiting process in electrochemical reactions and migration also plays a role in mass transport. The migration current is proportional to ionic concentration, the diffusion coefficient and the field strength. Field strength is determined by the applied potential, and also by the local electrostatic charge generated by the polymer as the oxidation state is changed.

Given the numerous interactions, the migration effect is difficult to calculate. However, if current is roughly proportional to the applied cell electrochemical potential, and will therefore be constant for a given cell potential, the strain amplitude will be proportional to time and to  $f^1$ .

In summary, a simple model which predicts that charge is directly proportional to strain and stress, has been chosen. A direct relationship between charge and strain has been observed previously, as noted in the discussion of actuator mechanisms. However, this direct relationship has not been reported in polypyrrole (the material used in the experiments described here), and no attempt has been made to date relate charge to stress as well as strain. The relationship between charge, stress and strain is central to predicting the operation of a conducting polymer actuator and in determining appropriate control strategies for optimizing actuator performance.

The rate of contraction is likely mass transport limited. Equation 18 predicts the response under diffusion limited conditions, while if migration is the limiting factor the strain amplitude as a function of frequency is inversely proportional to frequency. The determination of the rate limiting step has implications for future design. If diffusion is the rate limiting step, for example, a reduction in the film thickness by a factor of two will increase bandwidth four fold (see Equation 3).

Experimental results are now reported, beginning with polymer synthesis procedures and experimental methods. Results of passive tensile tests, isotonic and isometric measurements are then presented and compared with the models just described.

### 3.3.3 Film Synthesis

Various methods of polymer film fabrication were investigated. The desired film properties are:

- High conductivity in order to ensure low resistive losses across the film upon activation.
- High yield stress, to avoid fracture and plastic deformation during use.

Electrical stimulation of the polymer films investigated in this report was made through electrical contact at either end of the film. Electrons must then travel a long way out of or into the material when oxidation or reduction occurs. Resistive losses therefore become significant, especially at high redox rates. Furthermore, typically one out of every 10 to 100 monomers are oxidized or reduced in the course of full contraction, implying very large charge transfer (0.01 to 0.1 *mole/mole monomer*).

Thus, high conductivity is essential to increase the electromechanical efficiency of conducting polymer fibers and films. Higher conductivity also reduces voltage drops across the film or fiber and will therefore minimize differences in reaction rates through the polymer bulk. High yield stress, the second desirable material property, places an upper bound on the stress that can be generated by the actuator without damage.

We fabricated our films with an electrochemical deposition method developed by Yamamura *et al.*<sup>14</sup>. The polymer used is polypyrrole (PPy), which is synthesized and operated in a propylene carbonate electrolyte solution. Polypyrrole is one of a few conducting polymers that are stable in air and of that group, it is the one that exhibits the highest conductivity. Electrodeposition is the favored method for producing films because it gives greater density, high molecular weight, good mechanical properties and high conductivity. While chemical methods of polymerization are slightly less expensive, they are complicated by the fact that polypyrrole is insoluble, and thus precipitates at low molecular weights.

### 3.3.3.1 Polymerization

A mixture of  $0.06M$  freshly distilled pyrrole monomer and  $0.05M$  tetra ethyl ammonium hexafluoro phosphate is prepared in propylene carbonate. Polypyrrole is then electrodeposited onto a glassy carbon substrate. A copper counter electrode is employed and in galvanostatic (constant current) mode, the deposition current density on the glassy carbon is  $1.25 \text{ A m}^{-2}$ . Deposition takes place at  $-30^\circ\text{C}$  in a nitrogen atmosphere. The resulting films have densities of  $1440 \text{ kg/m}^3$  and their counter ion content is  $0.27 \text{ PF}_6^-$  per monomer<sup>14</sup>.

The low temperatures used appear to limit side reactions, which can degrade conductivity. Glassy carbon, which is polished to a 0.05 micrometers finish, allows ready removal of the film either by direct peeling or thermal shock with liquid nitrogen.

With this fabrication procedure, conductivities exceeding  $3 \times 10^4 \text{ S/m}$  and tensile strengths of greater than  $25 \text{ MPa}$  are routinely achieved. Typical films are 30 micrometers thick, 10 mm wide and 30 mm long.

### 3.3.4 Film Actuator Characterization

The films are characterized in terms of stress, strain and strain rate. In tests of active properties, either current or voltage are applied and recorded. These tests enable the determination of passive

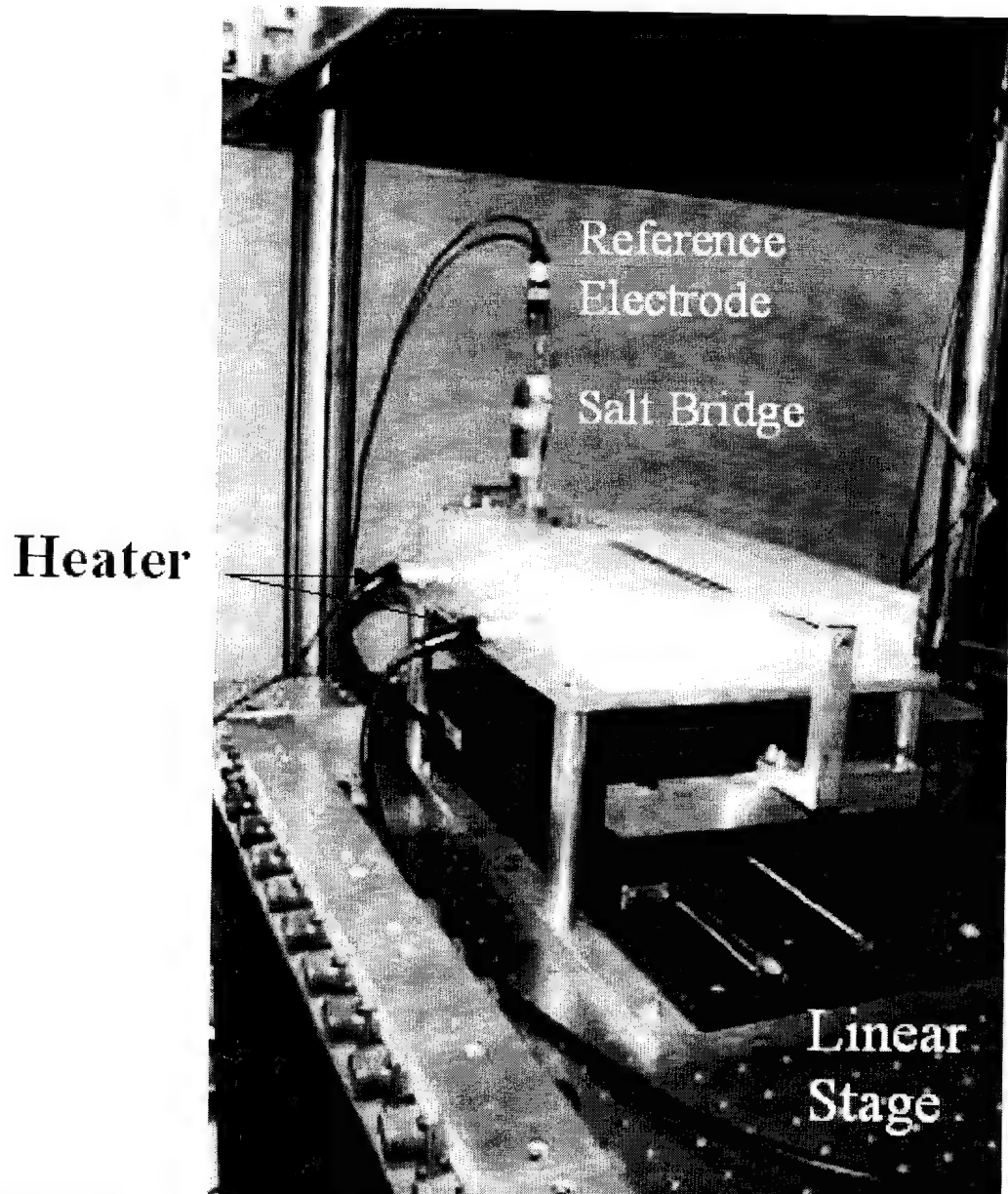


**Figure 15:** Photograph of apparatus for chemical, mechanical and electrical characterization of conducting polymer films.

---

<sup>14</sup> Yamaura, M., Hagiwara, T. and Iwata, K., "Enhancement of electrical conductivity of polypyrrole film by stretching: counter ion effect", Synthetic Metals 26 (1988) 209-224.

stress/strain relationships, and active stress, strain, strain-to-charge ratio ( $\alpha$ ) and strain rate. Measurement of these actuator characteristics will then allow us to estimate such performance parameters as pressure, displacement and flow rates for the different air inlet pump designs considered. The results presented here represent the first thorough chemical, electrical and mechanical characterization of conducting polymer actuators.

### 3.3.4.1 Mechanical Testing and Characterization: Apparatus

Characterizing the film actuators requires mechanical testing. Stress, strain, and rate of strain as functions of charge transfer and current are fundamental properties that have not yet been established for conducting polymer actuators. No commercial tensile testing device exists that adequately combines mechanical testing with electrochemical monitoring and excitation. Consequently, the apparatus shown in Figure 15 and Figure 16 was assembled.

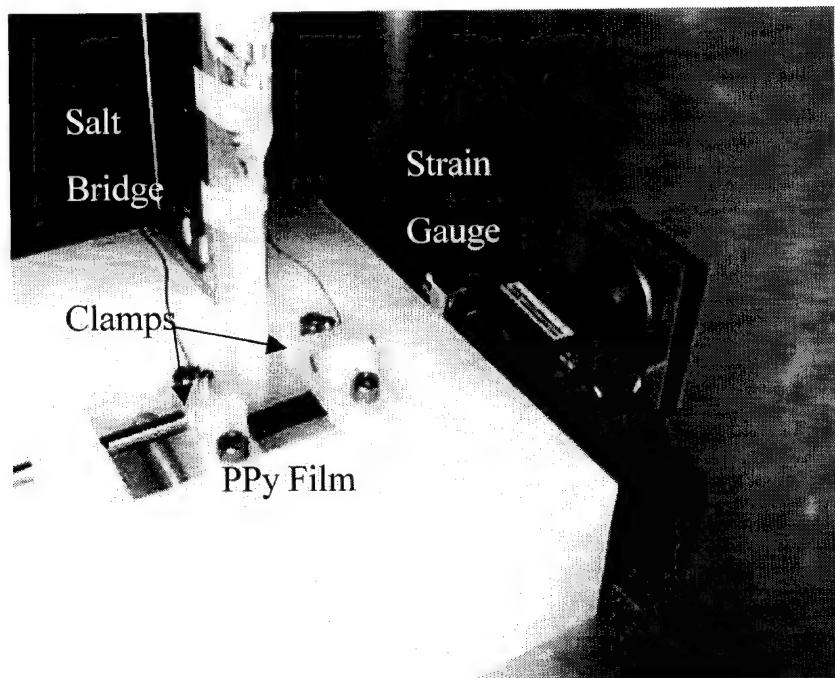


**Figure 16:** Close-up of the electro-chemo-mechanical testing apparatus showing the strain gauge, salt bridge and clamping arrangement of the pyrrole films.

The electro-chemo-mechanical test bed consists of a polypropylene bath, which sits above a linear motion stage. Films are mounted in the bath via two clamps, shown in Figure 16. One clamp is stationary with respect to the bath, and is fixed to a strain gauge (Omega LCCA-25), providing force transduction. The second clamp is fixed to a stainless steel rod. The rod translates along the length of the bath in response to a motion of the stage, which in turn is powered by a stepping motor. The clamps include connectors allowing electrical contact with mounted films. A stainless steel counter electrode is mounted inside the bath. With films mounted and immersed in a salt solution, electrochemical potentials can be applied between the counter electrode and the film mounted between the clamps. The applied potential, force (via Strain gauge amplifier Vishay 2311, gain of 1000), and current are recorded on a 16 bit A/D (HP E1413A). Displacement of the film is proportional to the number of steps traversed by the stepping motor, which in turn is controlled by computer via digital input and output (C&H VX441C). The electrochemical potential drop across the film is referenced to an Ag/AgCl reference electrode. The reference electrode is aqueous based, and therefore a salt bridge was employed between the aqueous solution and the propylene carbonate solution.

Strain was ramped linearly at various rates in the absence of applied voltage in order to investigate the passive mechanical properties of the films. Recording stress during the linear change in strain with time yields data from which the constitutive stress-strain relations can be extracted. Visco-elastic dynamics of the polymer actuators were studied by varying the rate of change of strain with time.

Two measurement protocols were employed to characterize the actuator's active properties. Isometric (fixed film length) and isotonic (fixed force) measurements were obtained, following well-established methods that are employed to characterize mammalian skeletal muscle other types of actuators.

The electrolyte in which films were immersed during measurement was  $0.05M$  tetra ethyl ammonium hexa fluorophosphate. This cation appears to be sufficiently large so that it cannot penetrate into the polymer from the propylene carbonate solution, forcing all doping to occur via the smaller anion. This follows observations by Pei<sup>15</sup> that if both cations and anions are mobile within

polypyrrole, charge balance will be attained by the combined outflow of one charge species and the inflow of the other, resulting in a smaller net strain.

### 3.3.4.2 Experimental Passive Mechanical Response

Key passive properties are the magnitude and time constant of stress relaxation, and the tensile strength. The following data were obtained using polypyrrole films prepared as explained above, and using the electro-chemo-mechanical test bed. In general for passive mechanical response, triangular waves in strain were applied and the resulting stress recorded. After each strain cycle, stress was allowed to relax back to near zero.

Tensile strength was determined by linearly increasing the strain with time until failure. The

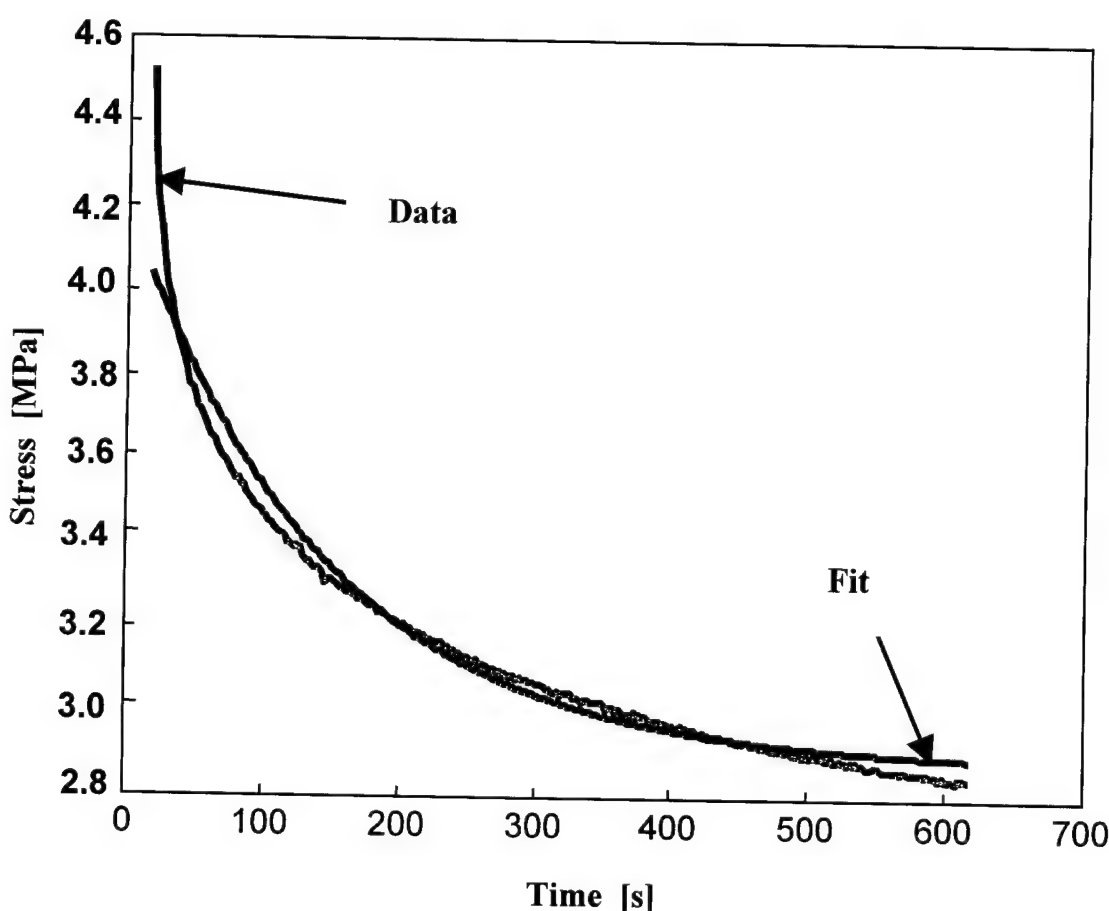
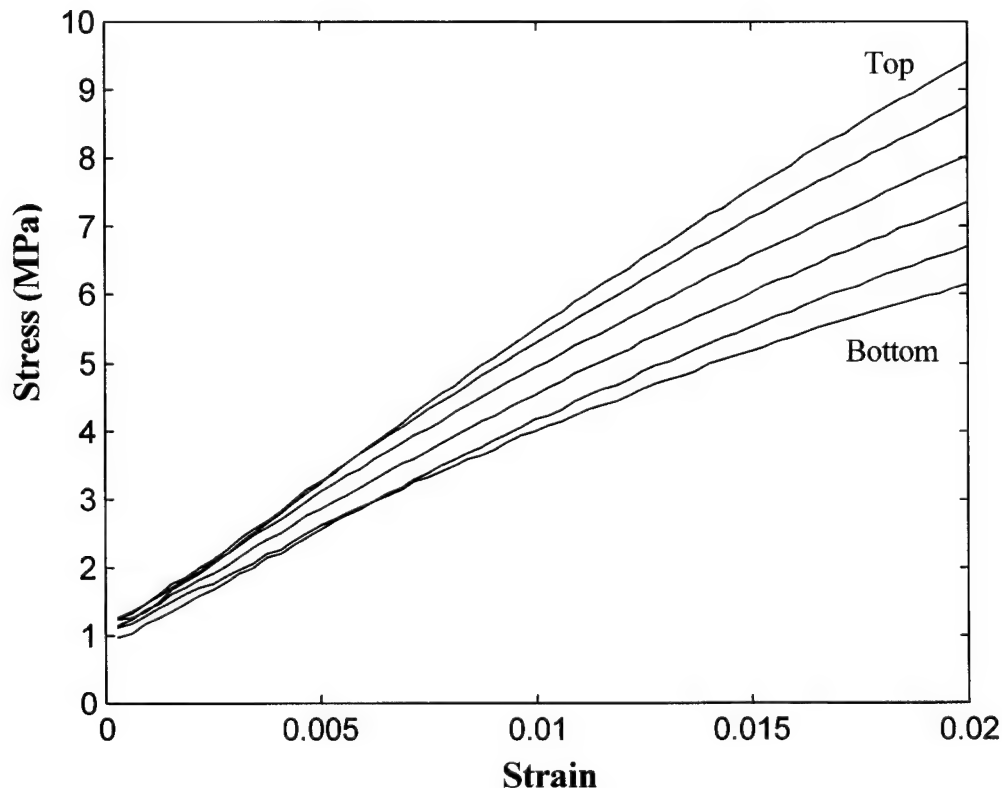


**Figure 17:** Stress relaxation following a 2% step in strain.

measured tensile strength of the polypyrrole films is 25 MPa. This provides an upper bound on the stress that can be generated by the polymer films.

Figure 14, Figure 17, Figure 18 and Figure 19 show data obtained from a polypyrrole film under a variety of conditions. The ends of the films were displaced relative to one another at given strain rates and the resulting forces were recorded.

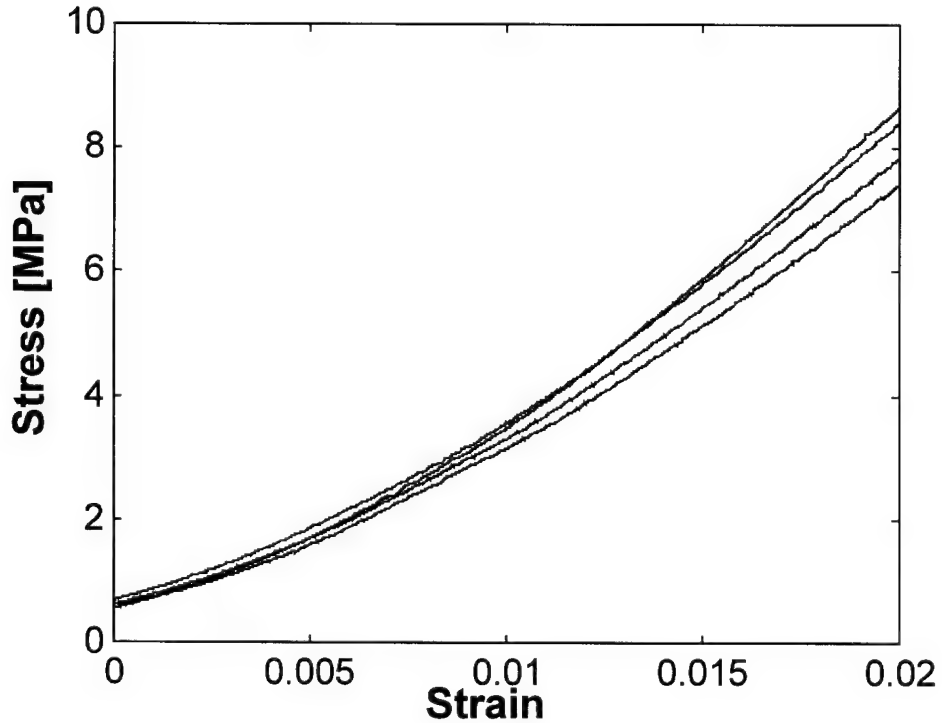
Figure 14 depicts the ramp response function for a film where the ramp amplitude  $\gamma = 0.00125$  per second, and the fitted model from Equations 7 and 9. It is clear from the apparent hysteresis that the system is lossy and that plastic deformation is occurring. Qualitatively the system behaves as expected in Equations 7 and 9, and the constitutive relationship depicted in Figure 12. Consider first the case where strain increases with time. The slope of the strain-stress plot is initially high as only  $E_1$  is felt but as elongation continues the system becomes more compliant, tending towards the series



**Figure 18:** Stress-strain for different increasing strain rates. From top to bottom, the rates applied to the film are 0.02 Hz, 0.005 Hz, 0.00125 Hz,  $3.1 \times 10^4$  Hz,  $8 \times 10^5$  Hz and  $2 \times 10^2$  Hz.

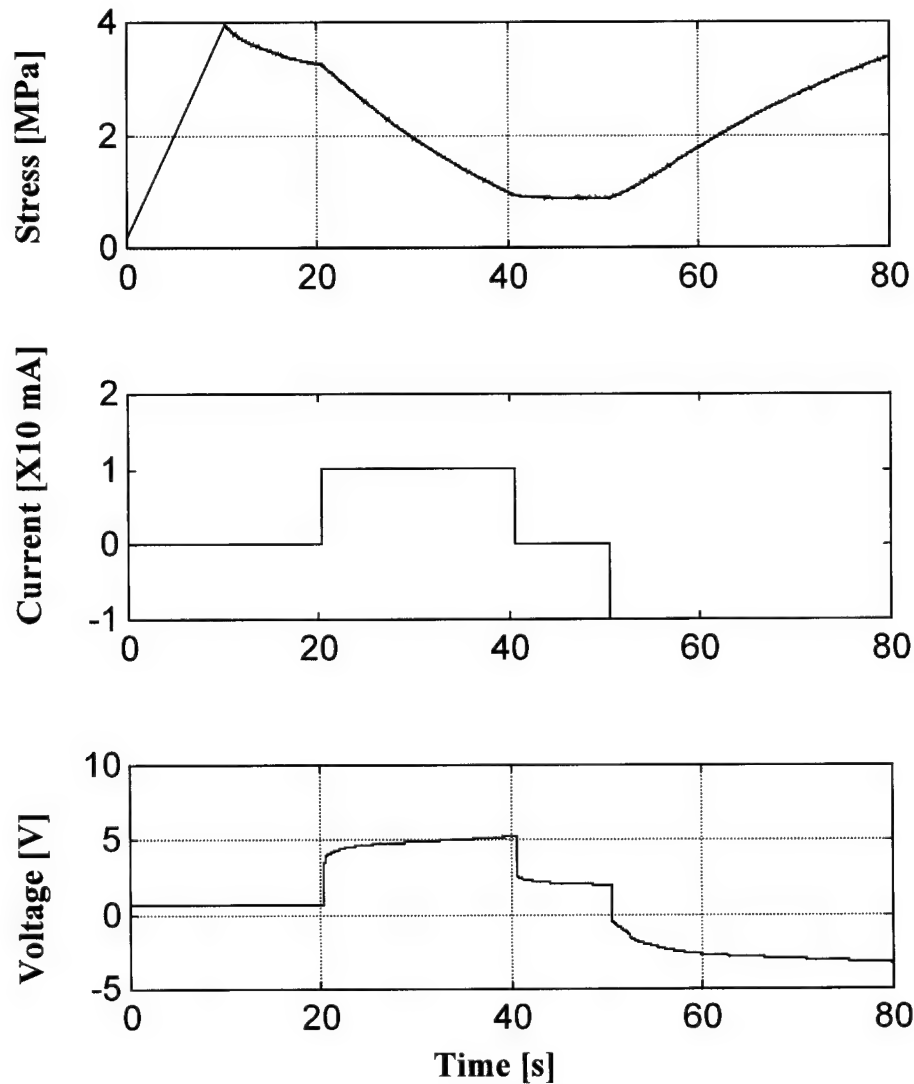
compliance of the two springs,  $E_1 E_2 / (E_1 + E_2)$ , in the limit as strain becomes large. There is an offset due to the constant stress generated by the viscous damper, now being strained at a rate  $\gamma$ . As strain is decreased with time, the model similarly describes the polymer behavior, except at the onset of the decrease in strain. This is partly due to the fact that the combined stepping motor and linear stage inertia is too large to generate the required discontinuity in velocity at peak strain, given the limited stepper motor torque. The elasticity of the material (slope of the curves in Figures 13 and 14), ranges between 0.75 GPa at short times to 0.25 GPa after relaxation.

Figure 17 shows the response to a 2% step in strain. The stress drops 30% over a period of 10 minutes. An exponential decay was fitted to the data, as specified by Equation 6. Note that the measured stress initially drops more rapidly than the fit curve, and does not plateau after 600 seconds, but rather continues to relax.



**Figure 19:** Stress-strain curves as a function of decreasing strain rate, from the top 0.008 Hz; 0.002 Hz; 0.0005 Hz; and 0.000125 Hz for the bottom curve.

The effect of strain rate on the stress-strain relations is shown in Figure 18 and Figure 19. Figure 18 shows how stress evolves under different strain rates as strain increases, while Figure 19 is the stress under similar conditions except for decreasing strain with time. Note that apparent stiffness (the slope of the stress-strain curve) increases as strain rate is increased, as expected in a visco-elastic material.



**Figure 20:** Typical film activation sequence. Input to the film is charge (current, middle plot) and the evolution of stress (top plot) and voltage (bottom plot) are measured with time.

By appropriate scaling and superposition of the ramp response at various rates, it is possible to determine whether the system is dynamically linear, or exhibits non-linear behavior. The passive behavior is in fact dynamically non-linear in nature.

Passive stress-strain analysis has revealed that the material tensile strength is  $25 \text{ MPa}$ . This provides an upper bound on the stress obtainable from the material. It is more than adequate for the sampler application. Of greater concern is the degree of stress relaxation observed. The step response of Figure 17, for example, shows a 30% relaxation in stress over 10 minutes. Furthermore, film stiffness varies by a factor of three, between  $0.25$  and  $0.75 \text{ GPa}$ . The active response of the material may then change over time as passive properties vary. Finally, ramp responses at various strain rates show that the material is dynamically non-linear in its behavior. Modeling and hence compensation for such effects is thus difficult.

Two solutions remain. The first is to add force and or displacement feedback to servocontrol the actuator while the second option is to alter the material processing. By stretch aligning the polypyrrole films, initial work suggests that relaxation effects become insignificant. Furthermore, tensile strengths are dramatically improved ( $>100 \text{ MPa}$ ) as is film stiffness. This option is very promising and could be pursued further in a Phase II follow on to this work.

### **3.3.4.3 Active Mechanical Properties: Isometric Measurements**

Key actuator properties that need to be evaluated for pump design are stress, strain, rate of strain, frequency response, magnitude of applied potential and the strain to charge ratio. Voltage and strain to charge together determine the size and lifetime of the battery in the sampler.

Redox reactions were induced electrochemically in the films. Step changes in current were applied. A typical activation sequence (Figure 20) shows stress, current and applied voltage as functions of time. Strain is ramped to 0.01 with zero applied current, resulting in a linear ramp in stress over the first 10 seconds. Strain is then held fixed and current is held at zero for a further 10 seconds. The stress plot shows passive relaxation occurring in the film. Current is then stepped to  $10 \text{ mA}$  for 20 seconds (top plot), resulting in a reduction in stress (top plot) and a rise in applied voltage

(bottom plot). This is followed by 10 seconds of zero applied current. Finally, a current of  $-10mA$  is applied, resulting in a rise in stress and a lowering of potential.

The expansion of the film occurs when positive ions (anions) flow into the film (and hence electrons are being removed from the film), indicates that overall more anions are entering the film than cations are leaving. Given that for the electrolyte used, namely  $N(C_2H_6)_4^+$   $PF_6^-$ , the anion is smaller than the cation, such a response is expected. The charge required to induce changes in stress is shown in Figure 22 and Figure 21. The data used in these figures is from the measurements shown in Figure 20. The slopes of these curves gives us the amount of stress generated per unit charge, about  $10 MPa/C$ .

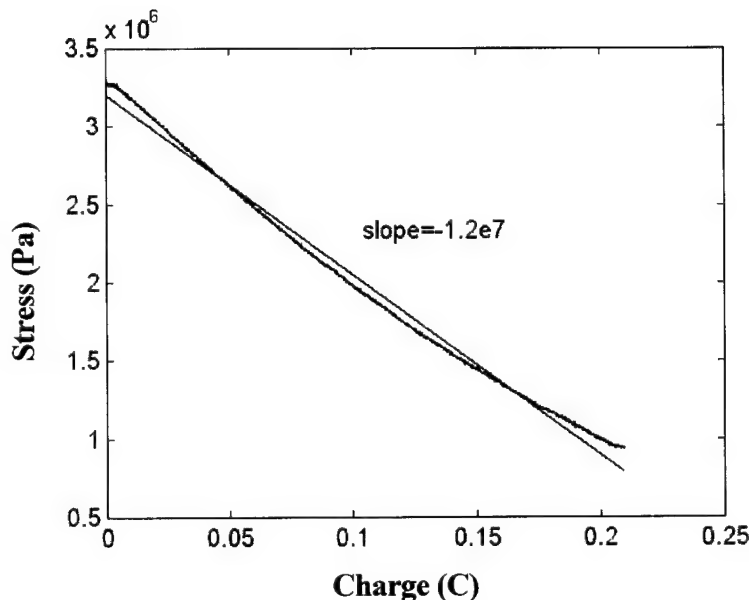


**Figure 22:** Stress generated in free-standing polypyrrole film as increasing amount of charge is injected into the film.

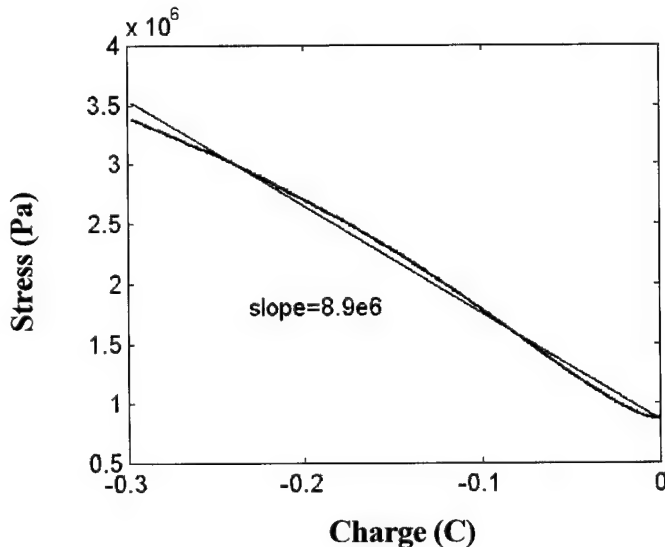


**Figure 21:** Stress generated in free standing polypyrrole film as charge is extracted from film.

Note that the change in stress per unit charge, as indicated by the fit slopes shown on each figure, is larger for decreasing stress/positive current than for increasing stress/negative current. This appears to be due to passive relaxation effects in the polymer, as observed in Figure 20 (top plot) between 10 and 20 seconds. In fact, when passive

relaxation, from Figure 14, is subtracted from the active response, Figure 22 and Figure 21, the upward and downward slopes agree to within 1 %, and virtually no curvature is observed. Stress is therefore directly proportional to charge, as predicted by the model of Equation 13.

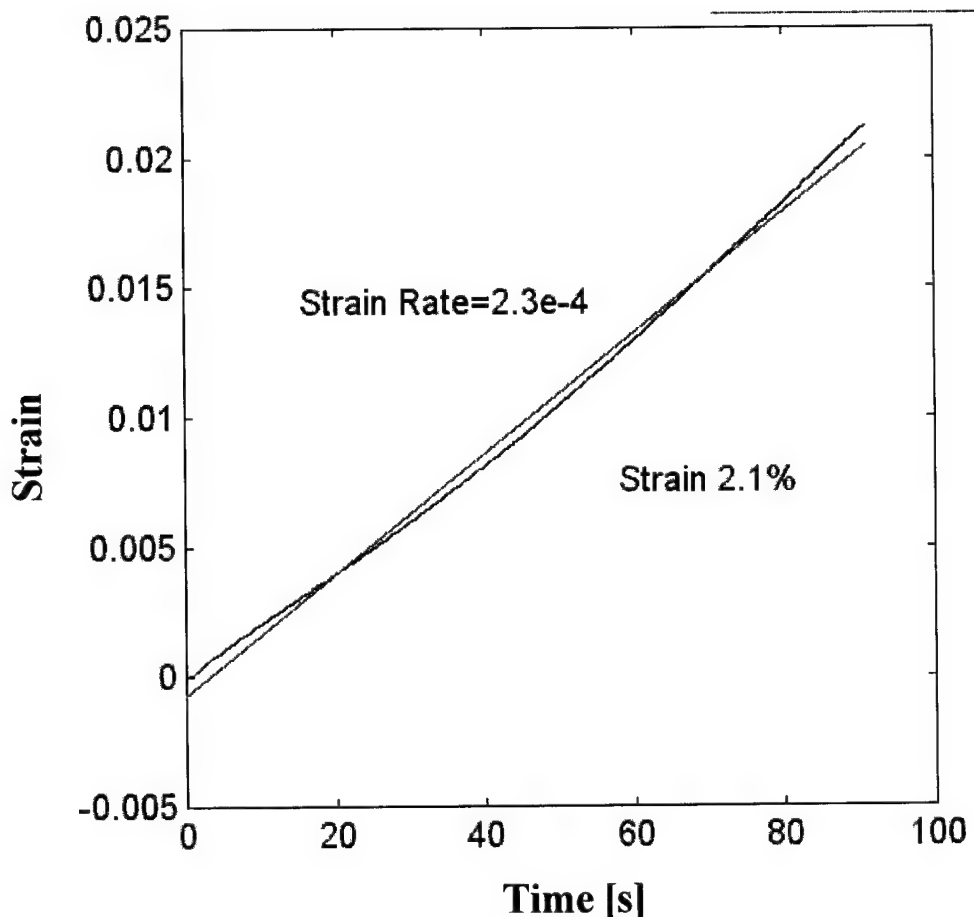


**Figure 23:** Strain induced in a free standing polypyrrole film with a constant bias stress of  $5 \text{ MPa}$  and an activation current of  $10 \text{ mA}$  current.

Strain is similarly proportional to charge under isotonic conditions, as depicted in Figure 23 and Figure 24. In both cases, a constant stress of  $5 \text{ MPa}$  and a current of  $10 \text{ mA}$  is applied to the film.

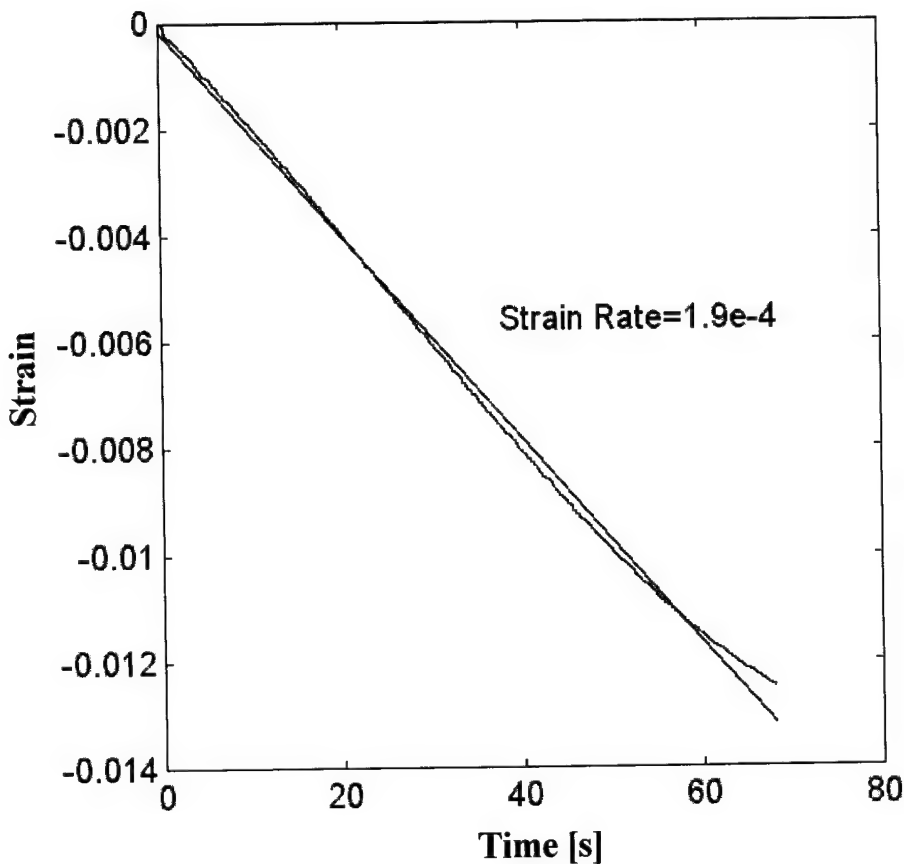


**Figure 24:** Strain induced in a free standing polypyrrole film with a constant bias stress of  $5 \text{ MPa}$  and an activation current of  $-10 \text{ mA}$  current.

From the isotonic (Figure 22 and Figure 21) and isometric data (Figure 23 and Figure 24) as well as the passive data it is possible to determine the constants  $\alpha$  and  $E$  in Equation 10. For these polypyrrole films and the electrolytic bath in which the polypyrrole film is immersed, we find that  $\alpha = 2.3 \times 10^{-12} \text{ C}^{-1} \text{ m}^3$ , or  $3.7 \times 10^{-31} \text{ m}^3 \text{ per ion}$  and  $E=0.5 \text{ GPa}$ . We have observed the film volume increases as the material becomes positively charged. This is consistent with a model of mobile anions and fixed cations because the cations are much larger than the anions, and appear to be too large to transport through the polymer.

### **3.3.4.4 Oxidation State**

The following section provides some further insight into the molecular mechanisms that give rise to macroscopic stress and strain and how these mechanisms relate to the magnitude of strain. Some speculation is also made on how strain might be increased.

The degree of oxidation provides an indication of how far the reaction has proceeded in the polymer. If the actuator experiences full oxidation or reduction while cycling, then it is reasonable to assume that maximum strain has been generated. If not, it may be possible to increase strain.

A measure of oxidation state is the proportion of monomer units or mers on the polymer backbone that are charged. The change in oxidation state can be determined by knowing the flow of charge into the material, and the density of mers. The reactions above show a change in oxidation state of 1 charge per 35 mers. Full oxidation or reduction involves changes of 1 charge per 2 mers, a much larger change. It is thus possible that larger strains could be achieved by further oxidation or reduction. In fact, chemical activation tends to result in larger dimensional changes<sup>12</sup>. It may then be possible to achieve significantly larger strains than those observed to date. The tradeoff is that conductivity also changes with oxidation state, which may make it difficult to further increase strain electrochemically.

The strains induced by this ion flux are approximately 2%, corresponding to volume changes of 6%. Assuming a density of  $2000 \text{ kg/m}^3$  for the ionic material, the ratio of volume change in the polymer to the ionic volume is approximately 4:1. The favorable ratio might be ascribed to the fact that the conjugated backbones of the conducting polymers are fairly rigid, and therefore an ion squeezing in between chains will displace a volume of material significantly larger than its own. It is also possible that other mechanisms such interchain electrostatic repulsion or other mechanisms are involved.

### **3.3.4.5 Frequency Response**

The stress and strain achievable as a function of frequency is important for two reasons. It provides an upper bound on the pumping rate, and it allows insight into the rate limiting mechanisms, and thereby clues as to methods to improve device bandwidth.

Increasing the frequency of activation reduces the amplitude of the response. Figure 25 is a log-log plot of the change in stress as a function of electrical stimulation frequency. 10 V square waves

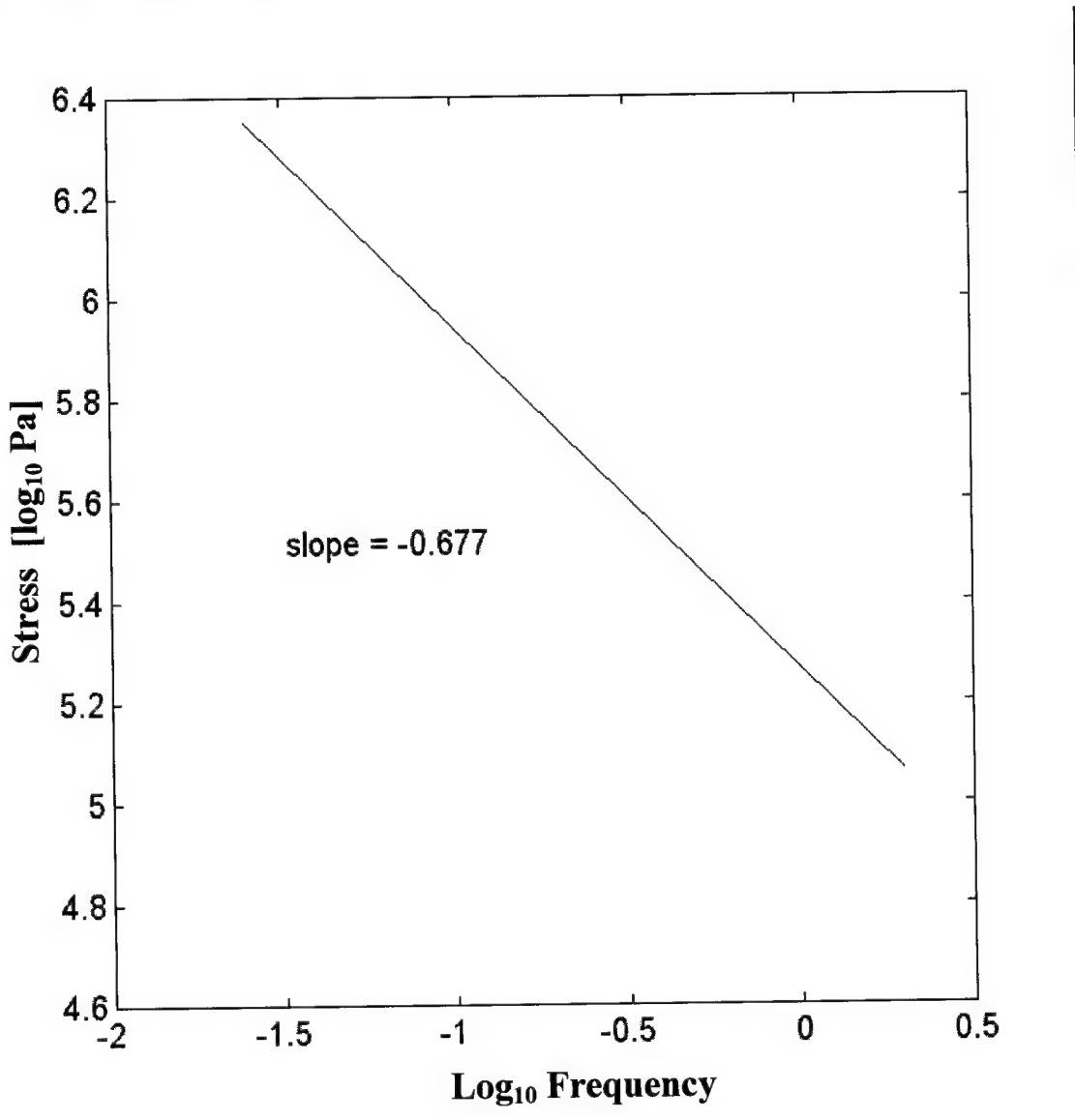


**Figure 25:** Stress induced in a polypyrrole film actuator as a function of electrical stimulation frequency.

were applied at frequencies ranging from 0.025 to 2 Hz for up to several hundred cycles. The slope of the roll off in response is  $-0.677$ . The expected slope for a purely diffusion limited system obeying Fick's Law would be  $-0.5$ , whereas for pure migration the slope is expected to be  $-1$ . Further study is required to indicate which mechanism rate limiting. In either case, rate should increase as film

thickness decreases, due to shorter ion transit distances. If diffusion is the limiting effect, then the bandwidth will increase as the inverse square of thickness, as given by Equation 1. Halving the thickness will increase activation rate by a factor of four. If on the other hand migration is rate limiting, a halving in thickness will double the rate. By employing multiple thin films in parallel, faster actuation can be achieved. The results suggest that, for one micrometer thick films, rates could be 30 to 900 times faster, or between 3 and 90 Hz for 2% strains. This is an exciting prospect that could be investigated in a Phase II follow on for further actuator development.

### 3.3.5 Bilayers

Bilayer actuators are useful for the movement of analytes within a liquid environment, where Reynold's numbers are lower than in air. They are also useful as valves and enclosures. In this section the work on bilayer actuators is summarized.

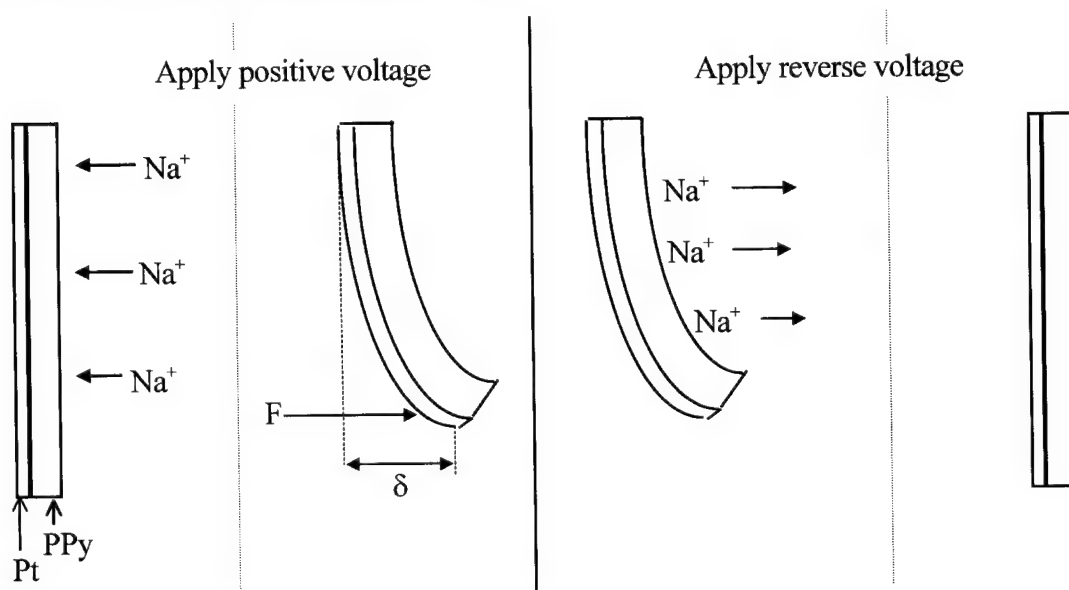


**Figure 26:** Schematic showing movement of ions in conducting polymer bilayer.

Bilayers are fabricated from two films and whose operation involves the change dimensions of one film relative to the other to produce a deflection (Figure 26). Bimetallic strips are familiar examples of bilayer actuators. In these materials changes in temperature and a difference in the coefficient of thermal expansion of the two metal layers, result in a beam deflection,  $\delta$  and a force,  $F$ . In the case of conducting polymer bilayers presented in this section,

the conducting polymer expands and contracts against a passive metal layer, producing deflection. In the section on air activation a bilayer is presented in which both layers are conducting polymer films with a thin electrolytic gel layer between them. On electrical activation, one polypyrrole layer expands while the other contracts.

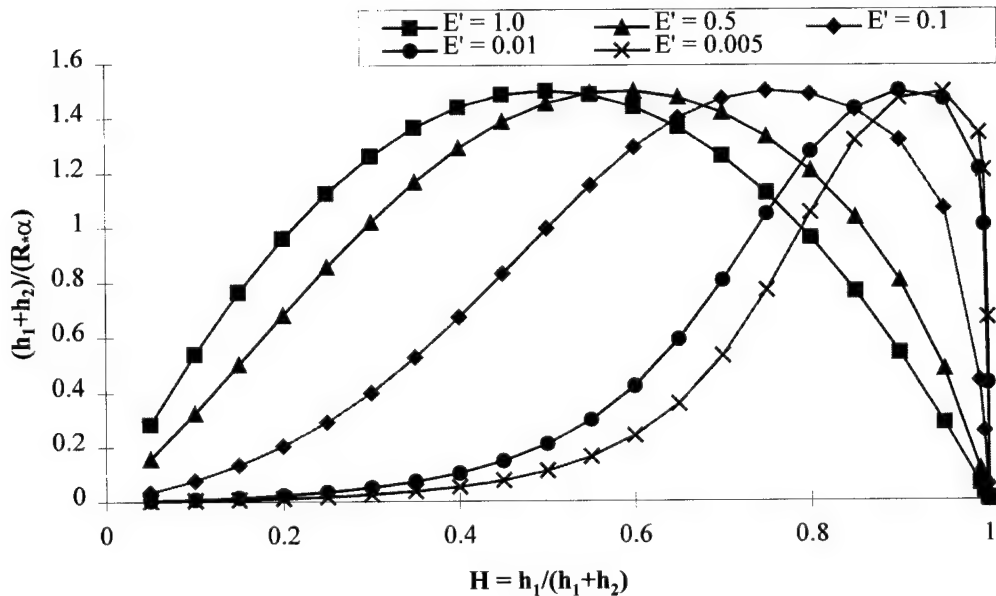


**Figure 27:** Dimensionless relationship between curvature and relative thickness of the bilayer layers for various ratios of between the two layers.

### 3.3.5.1 Theory of bilayers

The change in curvature of a bilayer is described by <sup>11</sup>,

$$\frac{1}{R} - \frac{1}{R_0} = \frac{6\alpha}{\left(E_1'E_2'h_1^2 - E_2'E_1'h_2^2\right)^2 + 4(h_1 + h_2)} , \quad 19$$

where  $R$  is the final radius of curvature,  $R_0$  is the initial radius,  $\alpha$  is the linear strain, the subscripts specify the layer,  $E' = E/(1-\nu)$  where  $E$  is the Young's modulus and  $\nu$  is the Poisson's ratio for that material, and  $h_1$  and  $h_2$  are the layer thicknesses.

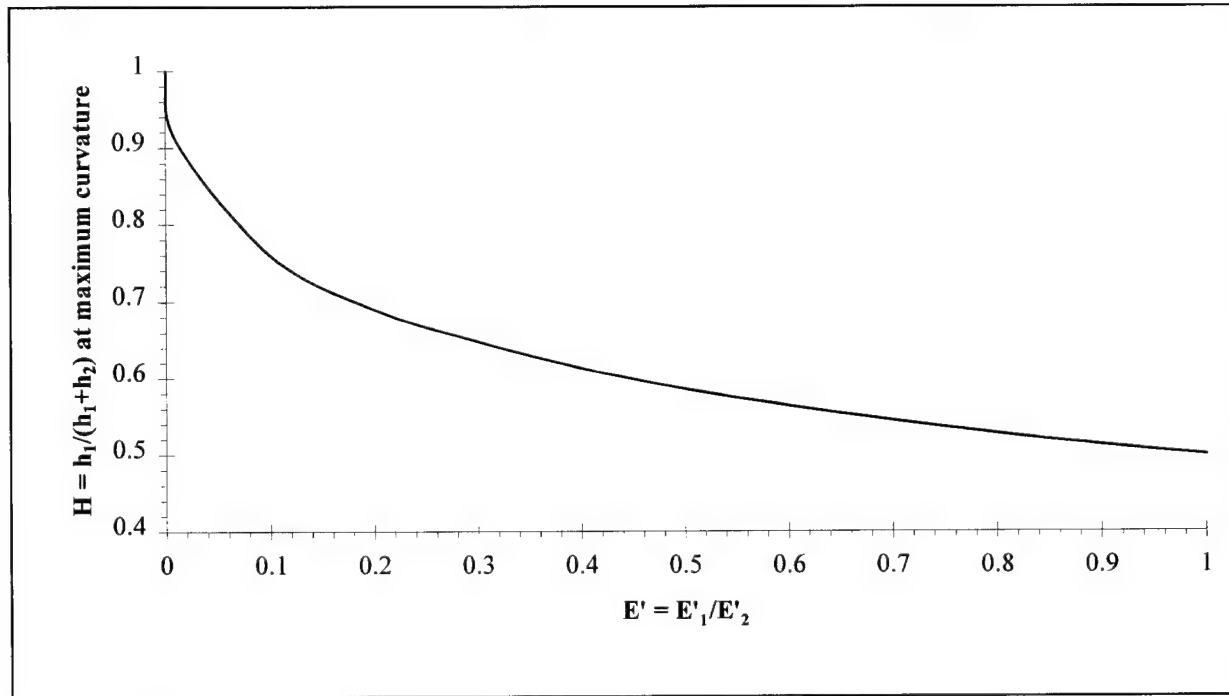


**Figure 28:** Dimensionless plot showing bilayer curvature (and thus deflection) as a function of relative thickness of the bilayer layers and elastic moduli of each layer.

The curvature and deflection are thus determined by the relative thickness and elastic moduli of the layers. In order to aid design we have put the bilayer equation in a dimensionless form,

$$\frac{(h_1 + h_2)}{R} = \frac{6\alpha}{\left[ E'H^2 - (1-H)^2 \right]^2 + 4}, \quad 20$$

where  $E' = E_1/E_2$  and  $H = h_1/(h_1+h_2)$ . Using Equation 17, curves for various values of  $E'$  can be plotted on an  $(h_1+h_2)/(R*\alpha)$  versus  $H$  graph, shown in Figure 28. Given the ratios of the elastic moduli it is possible to choose relative thicknesses in order to generate a particular deflection,

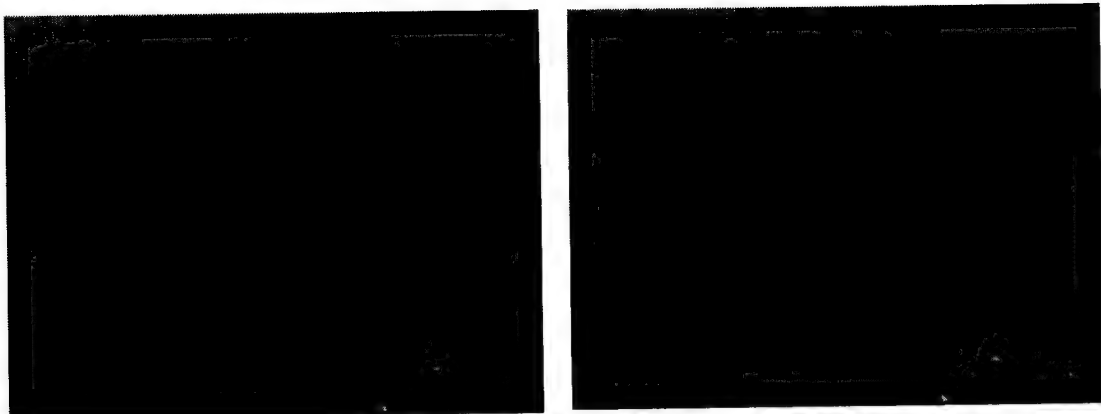


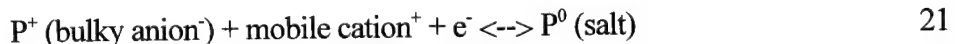
**Figure 29:** Photographs showing polypyrrole conducting bilayer activated with  $\pm 6$  V square wave applied with a 1 Hz frequency. The electrolyte solution was a 0.1M dodecylbenzenesulfonate aqueous solution.

provided  $\alpha$  is known. Often the maximum possible deflection is desired. Figure 28 provides the required thickness ratio to produce maximum deflection for a given ratio of elastic moduli.

The equations presented determine the bilayer response given the material properties of two layers, or alternatively enable one of the properties, e.g. strain, to be determined. The mechanism acts as a mechanical amplifier, allowing fairly large deflections to be observed in spite of small strains in the material.

### 3.3.5.2 Polymer strain mechanism

As with the polypyrrole in propylene carbonate, the mechanism of expansion and contraction appears to involve the insertion or removal of ions. In this case the small sodium cation is thought to move as depicted in Figure 5.



Here P represents a mer or repeat unit on the polymer backbone, in this case pyrrole. The pyrrole unit is shown in its oxidized and neutrally charged states. The bulky anion (dodecylbenzenesulfonate) is trapped within the material, whereas the cation ( $\text{Na}^+$ ) moves from solution (left hand side of the equation), into the polymer, to form a salt and balance charge (right hand side). It is thought that the influx of the cation during reduction of the polymer results in material expansion.

### 3.3.5.3 Experimental

The bilayers employed consist of a polypyrrole layer grown on a thin platinum layer. The platinum elastic modulus is about 200 times larger than that of the polymer, and hence must be much thinner in order to produce maximum deflection, as suggested by the design data in Figure 28.

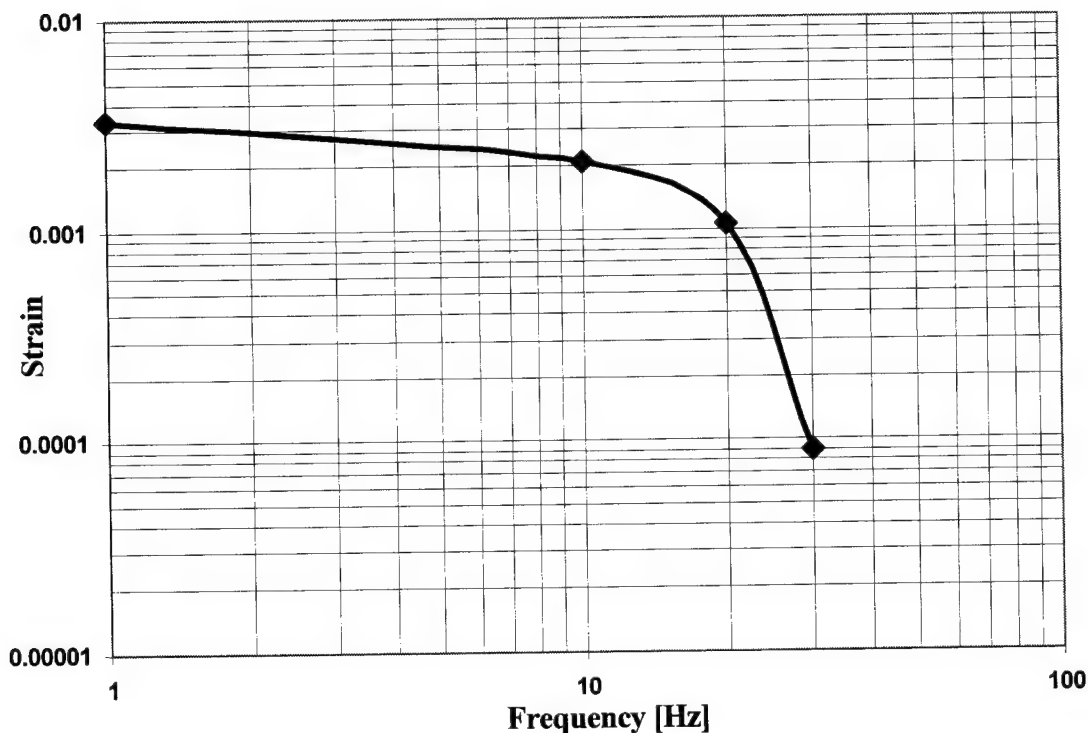


**Figure 30:** Polypyrrole bilayer mechanical frequency response in a  $0.1M$  dodecylbenzenesulfonate aqueous solution. The excitation voltage was a  $\pm 6 V$  square wave.

Polypyrrole was synthesized electrochemically from a  $0.1M$  Pyrrole,  $0.1M$  Sodium Dodecylbenzenesulfonate (DBS) aqueous solution. Deposition took place on a  $250\text{ nm}$  thick platinum film. The film was evaporated onto mylar (CHR, New Haven CT), with a  $50\text{ nm}$  titanium layer between the platinum and the mylar. The mylar film was  $10\text{ mm}$  wide by  $75\text{ mm}$  long by  $32$  micrometers thick. Deposition was performed galvanostatically against a very large stainless steel counter electrode (20 times the surface area of the working electrode).  $150\text{ nA}$  of current were

delivered over 17 hours at an average potential of  $0.83\text{ V}$  versus the counter electrode to yield a 61 micrometer thick film.

The resulting polypyrrole film and the platinum backing were peeled from the mylar layer and cut to form a  $0.75\text{ mm}$  wide by  $7\text{ mm}$  long finger. The finger was immersed in  $0.1M$  sodium dodecylbenzenesulfonate aqueous solution. A potential of  $+/- 6\text{ V}$  was applied between the finger and a large stainless steel counter electrode.

### 3.3.5.4 Bilayer Results

Figure 29 shows the deflection of a bilayer with a  $1\text{ Hz}$  activation frequency and its mechanical frequency response is given in Figure 30. Note that the  $3dB$  frequency response is  $10\text{ Hz}$  (the highest bandwidth yet reported in a conducting polymer actuator) and the slope of the roll-off above this frequency indicates the bilayer behaves mechanically as a  $4^{\text{th}}$  order system. The strain is calculated using Equation 16.

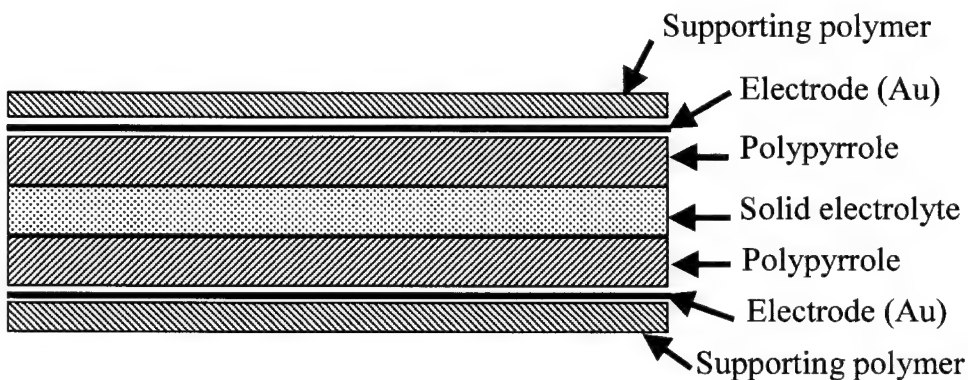


**Figure 31:** Encapsulated bilayer configuration for operation of conducting polymer actuator in air.

Larger deflections can be obtained by reducing the film thickness, thereby reducing the radius of curvature (which scales with thickness) while keeping the length constant. However the greater stiffness associated with thicker films is essential for valve applications, allowing the strip to overcome the  $40\text{ kPa}$  pump back pressure.

### 3.3.6 Bilayer operation in Air

To date, conducting polymer actuators have been restricted to operation in a liquid electrolyte. There are many situations, however, where operation out of such environments is desired, such as in air or in a fluid deficient in electrolytes, and, to do so, the actuator must be encapsulated. Mammalian skeletal muscle is Nature's example of an encapsulated actuator that can operate in a hostile environment. A similar encapsulation approach is employed here to enable operation of the conducting polymer bilayers outside of a liquid environment.

#### 3.3.6.1 Synthesis

The polypyrrole films employed in the air actuator were fabricated with the identical procedure described in Section 4.4. Two polypyrrole strips 10 mm wide by 40 mm long by 40 micrometers thick were cut. A sandwich structure was formed, as shown in Figure 31, with the polypyrrole strips forming outer layers, and containing a gel electrolyte between them. Gold was sputtered onto the

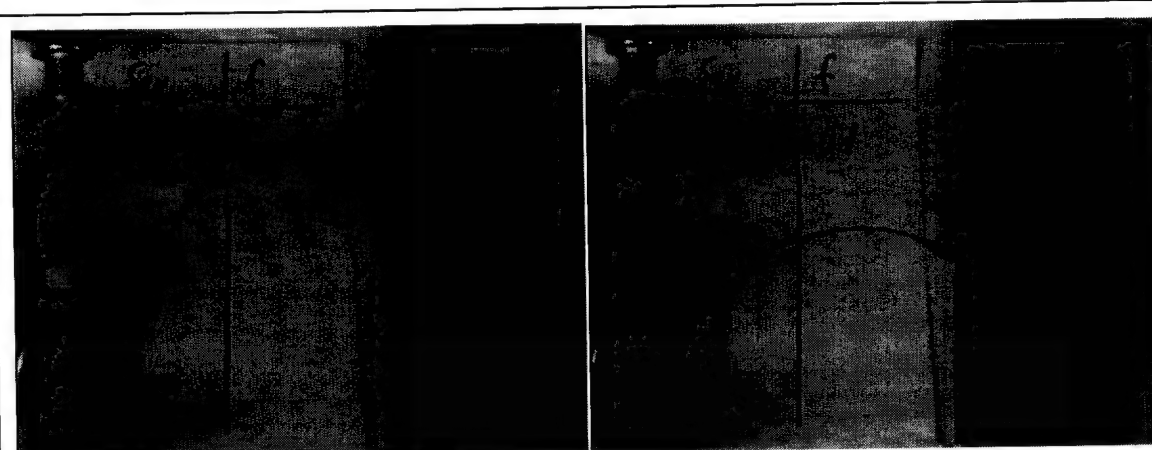


**Figure 32:** Air bilayer activated with  $\pm 5V$  applied at 0.1 Hz.

outer polymer surfaces, and the entire actuator was encapsulated in polyethylene tape, as indicated in the Figure 31. The gel layer was approximately 100 micrometers thick. The gel is synthesized according following a procedure related by Reynolds<sup>15</sup>. It consists of 70 wt% acetonitrile, 20 wt% propylene carbonate, 7 wt% polymethylmethacrylate (PMMA), and 3 wt% LiClO<sub>4</sub>. The actuator was

---

<sup>15</sup> Reynolds, J.R. Advanced Materials, 8:10 p.808

soaked for 15 minutes in a solution of 0.05M tetra ethyl ammonium hexafluoro phosphate in propylene carbonate, which rendered the polymer more compliant.

### 3.3.6.2 Testing

A square wave potential was applied (HP3245A Universal Source) between the platinum backing and a stainless steel counter electrode. Bilayer deflection was observed under a microscope (Zeiss Stemi SV 11). The microscope image was recorded using a CCD camera (Hitachi VK-C630) whose output went to a video tape recorder. The magnitude of deflection was determined from these images. The square wave peak to peak amplitude was between 2 V and 20 V, and applied frequencies ranged from 0.1 Hz to 60 Hz. Figure 32 is a pair of images showing the deflection of the bilayer on activation with a +/- 5V square wave at 0.1Hz frequency.

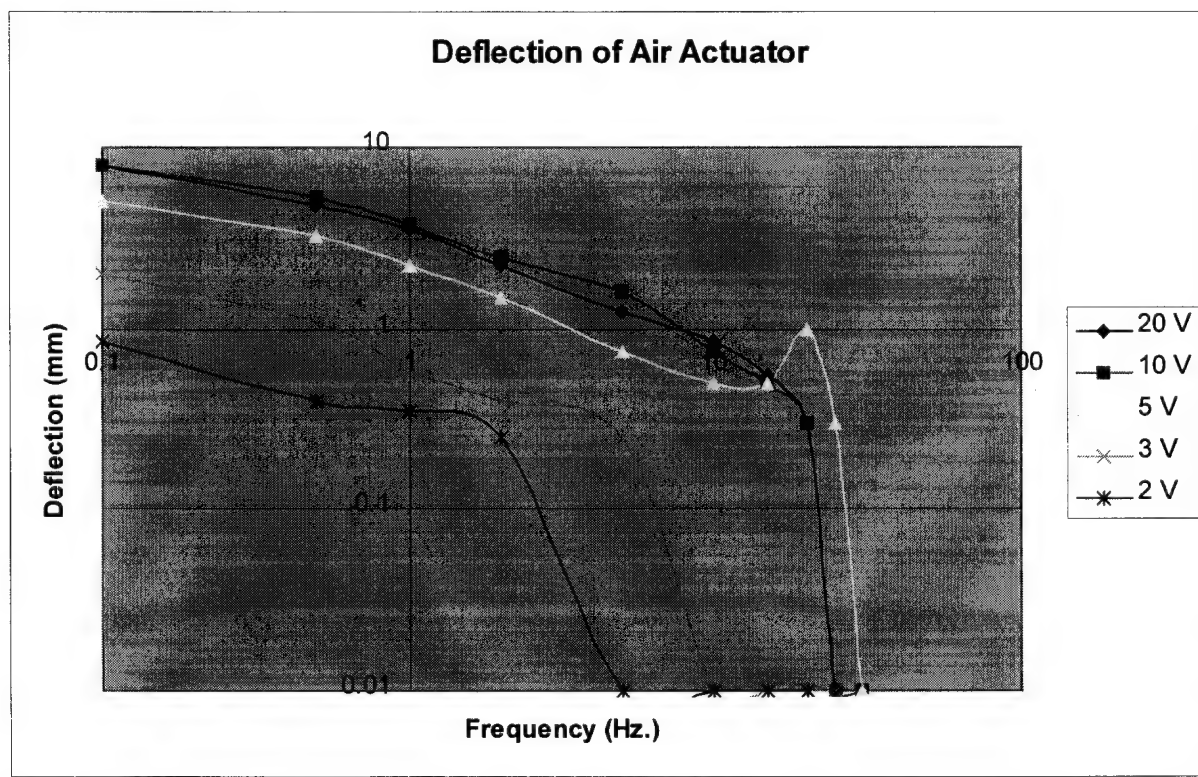


**Figure 33:** Mechanical frequency response of an encapsulated conducting polymer bilayer. Each curve plotted corresponds to a different peak-to-peak square wave voltage applied to the bilayer. For voltages greater than 5V, the 3dB roll-off occurs at a frequency > 10Hz.

### **3.3.6.3 Results**

Deflection as a function of frequency of activation and for different applied peak-to-peak voltages is shown in Figure 33. At low frequencies, scale in proportion to applied voltage such that for the maximum applied voltage ( $\pm 20V$ ) the end displacement of the bilayer was approximately  $1mm$ . Increasing the excitation frequency in all cases decreased the deflection with a  $3dB$  point for voltages above  $\pm 5V$  greater than  $10Hz$ . Above this frequency the bilayer deflection decreases rapidly with increasing frequency. This drop appears to correspond to the mechanical resonance of the bilayer. This result is very important as it sets the stage for activation of conducting polymer actuators out of liquid electrolytes.

## **3.4 Summary and Conclusions**

Section 3 describes our work in the electro-mechanical characterization of conducting polymers to determine their suitability as actuators for air inlet pumps and for controlling flow of liquids in a detector system. Our work has focused almost exclusively on one conducting polymer, polypyrrole, because of its low sensitivity to oxidation in air, and its high conductivity. Measurements were made of the passive (i.e. electrically unactivated) stress-strain properties of free-standing polypyrrole films and the results fit to a standard passive mechanical model. From these measurements a film tensile strength of  $25 MPa$  was found. It was also determined that substantial stress relaxation occurs at at  $2\%$  strain. Further study is required to determine the range of strains over which relaxation is minimized as well as fabrication techniques, such as stretch alignment, that will make relaxation effects negligible. Next, with a specially-built experimental setup, isotonic and isometric measurements were made of free-standing polypyrrole films as functions of electrical activation level. These measurements verified that the stress, strain and energy densities of polypyrrole actuators were greater than those required for an air inlet pump application. Dynamic isotonic and isometric measurements were also made and, after the passive mechanical properties accounted for in the data, it was shown the both the stress and strain were directly proportional to applied charge. The isometric and isotonic frequency response of the films indicated the charge transport process into and out of the film was a combination of diffusion and migration.

Electrically-activated conducting polymer bilayers were fabricated and their mechanical frequency response (displacement versus frequency) were measured when immersed in a liquid electrolyte. Achievement of high bandwidths ( $> 10 \text{ Hz}$  3  $\text{dB}$  bandwidth) for relatively large displacements ( $> 100 \mu\text{m}$ ) encouraged us to next create an encapsulation method to make the bilayer operation independent of the surrounding medium. Accordingly, we observed mechanical displacements of electrically-activated encapsulated bilayers exceeding 10 Hz when operated in air. Our bilayer results are an important and necessary step towards realizing microcilia and electrically-activated self-assembled enclosures whose function is independent of the external environment.

## 4.0 Voltage-controlled gas release capsule

### 4.1 Introduction

Realization of small, low power and low cost devices that can release small volumes of gases or fluids in a controlled manner into an external environment is a general problem to solve in field-portable biological detector inlets. We have devised a miniature gas release capsule (10 mm diameter  $\times$  10 mm height) that consumes little power ( $< 1 \text{ mW}$ ) capable of controlled and repeatable (if the reservoir is refilled) release of a compound contained within the capsule.

The operating principle of the gas release capsule can be seen from the schematic in Figure 34. Gas generated by the electrochemical cell inflates a bladder constructed from an impermeable elastic membrane. A second bladder or chamber is fabricated from an elastic membrane on one side and a semi-permeable membrane on the other. Inflation of the first chamber applies pressure to the second chamber membrane, which in turn, forces compound to move through the outer semi-permeable

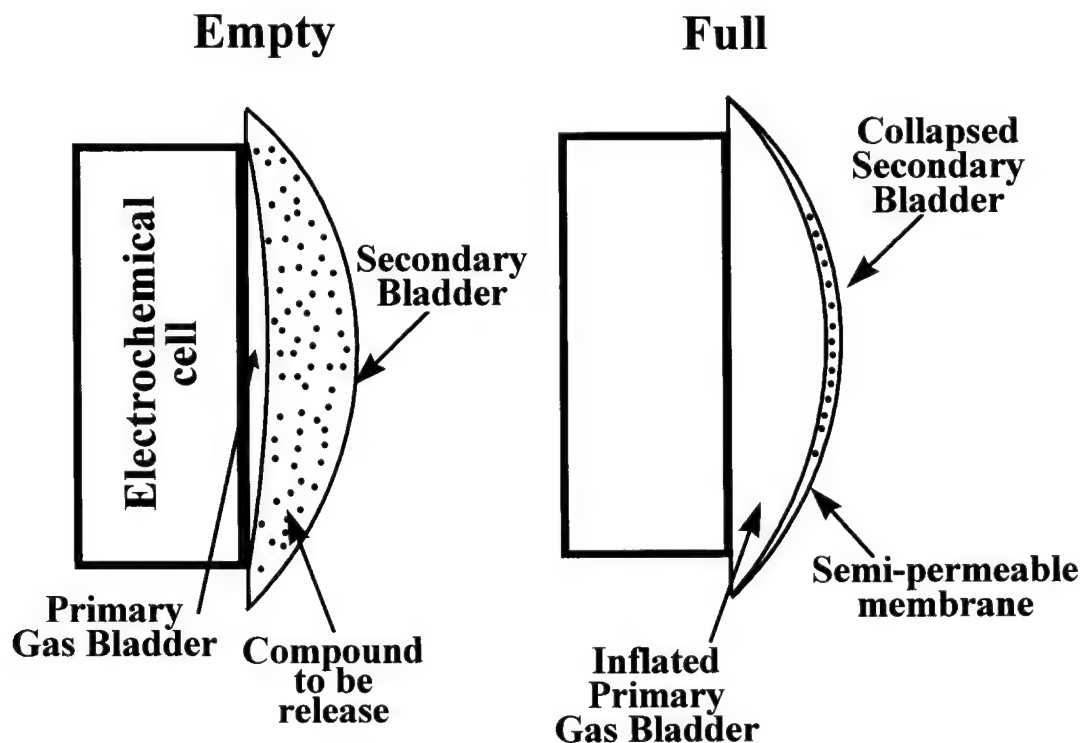


**Figure 34:** Schematic showing controlled-gas release capsule concept. Gas evolved from the electrochemical cell pressurizes the primary gas bladder resulting in a pressure applied to the secondary bladder that expels its contents.

membrane of the second chamber to the outside world.

The amount of material expelled from the capsule can be precisely controlled through the monitoring and control of the gas pressure in the primary chamber. Also, since the amount of gas generated is directly proportional to the amount of charge passed through the cell in a given period, the integration of the current magnitude times its duration can also be used to meter the release of compound from the capsule. Thus, the pressure differential between the first chamber and the outside ( $\Delta P$ )<sub>o</sub>, is one important determinant of the mass flow rate of material from the capsule. A second is the passive transport properties of the compound through the semi-permeable membrane.

For a long diffusion time constant of compound through the outside membrane relative to the pressurization time of the second chamber by the first, the following sequence describes how material is expelled from the release capsule. First, the gas pressure in the first bladder is increased to an initial value,  $P_i$ , by driving a current through the electrochemical cell. The moles of gas thus generated,  $\tilde{n}$ , is proportional to the electrical charge,  $Q$ , passed through the cell during the time interval,  $\Delta t$ . Thus,

$$\tilde{n} = \frac{I \Delta t}{n F} \quad 22$$

where  $I$  is the electrical current through the cell ( $I=dQ/dt$ ),  $F$  is Faraday's number (96 494 C/mole) and  $n$  is the number of electrons per ion or molecule. Assuming an ideal gas at constant volume and that the compound in the second cell is in a liquid state, the initial pressure difference across the second bladder's membrane is given as

$$(\Delta P)_o = P_i - P_{oi} = \frac{\tilde{n}RT}{V} = \frac{I \Delta t RT}{V n F} \quad 23$$

where  $R$  is the ideal gas constant (0.082 atm-l/mole-°K),  $T$  is the gas temperature,  $V$  is the volume and  $P_o$  is the external (atmospheric) pressure. This pressure difference across the cell membrane is the force per unit area, which drives the fluid (or gas) through the membrane to be expelled from the pump. The mass flow of material expelled from the second bladder is a function of the applied pressure. If the volume of the second bladder remains essentially constant for a period then the mass flow rate of material from the cell is also constant. As the primary gas bladder volume increases the

pressure differential applied to the second bladder will decrease. Increasing the electrochemical cell current to increase the primary gas pressure can compensate the corresponding decrease in mass flow rate. Feedback from an external chemical or internal pressure sensor can be used to control the cell current and keep the flow rate of material from the cell constant.

Two controlled release capsules were constructed and evaluated. The first is based on the electrochemical decomposition of Li<sub>3</sub>N to evolve N<sub>2</sub> gas to pressure the gas bladder while in the second device water (H<sub>2</sub>O) is electrolytically decomposed to evolve oxygen (O<sub>2</sub>) for gas bladder inflation. This section of the report details the design, fabrication and testing of each of the two controlled-release capsules. The basic operating principle will be elucidated, test data demonstrating the operation of each cell will be given and recommendations regarding the applicability of each capsule design will be given within the context of inlets for Chemical and biological Warfare (CBW\_sensor systems and other potential applications of the device. An experimental demonstration will also be given showing the scalability of the controlled-release capsule technology to enable large volume release of compound. Finally, future directions future directions regarding inlets for CBW sensor systems and other commercial applications will be outlined.

#### **4.2 Nitrogen gas controlled release capsule**

A controlled release capsule was developed based on the electrochemical decomposition of Li<sub>3</sub>N to produce Li metal and evolve nitrogen gas. The pertinent electrochemical reactions are as follows:



The above set of reactions occurs when the applied DC voltage is above the Li<sub>3</sub>N decomposition voltage of 0.45 V the reaction will continue until all the Li<sub>3</sub>N is consumed.

#### 4.2.1 Electrochemical Cell Design

$\text{Li}_3\text{N}$  powder was mixed with carbon black and pressed into disks 12.5 mm in diameter and 3 mm thick by a ten-ton press mounted in a glove box under a  $\text{N}_2$  environment. The carbon black was used as a conductor to provide a uniform current density in the disk. To form a cell, a disk was sandwiched between two Ni meshes that act as anode and cathode electrodes. The anode was held at earth ground and the cathode connected through a  $1.5 \text{ k}\Omega$  resistor to a 1.5 V DC power supply. The decomposition current was determined from the voltage drop measured across the  $1 \text{ k}\Omega$  resistor. All measurements were conducted in the glove box with a nitrogen environment so the reaction between the air moisture and  $\text{Li}_3\text{N}$  was eliminated. Figure 35 is a schematic that summarizes the experimental layout.

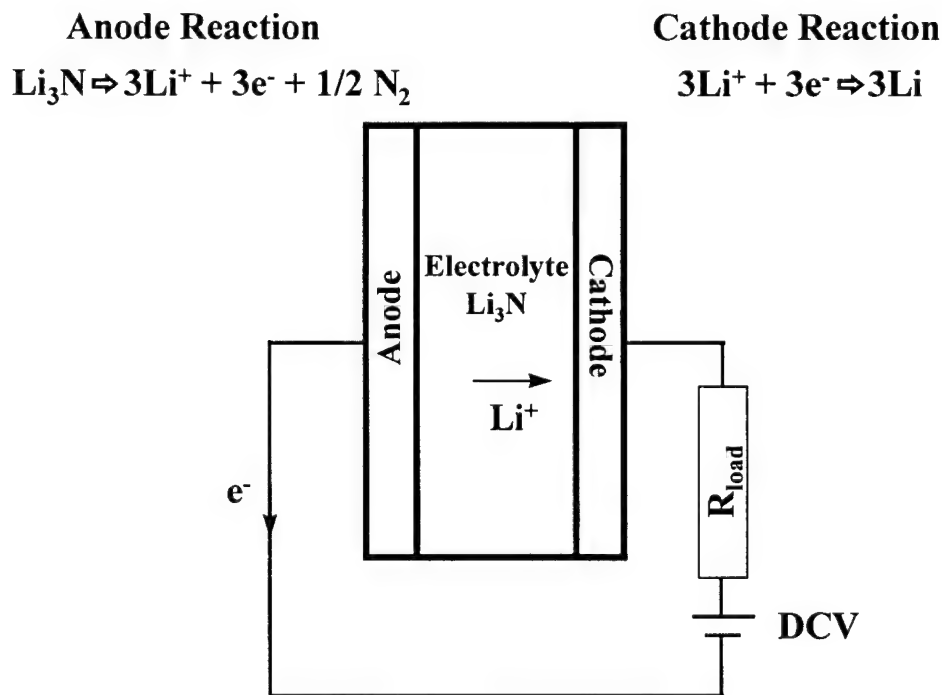


**Figure 35:** Schematic showing general experimental layout for  $\text{N}_2$  gas cell.

#### 4.2.2 Experimental Results

The gas evolution rate was measured to be  $3.8 \text{ cm}^3/\text{day}$  for a cell current of  $1 \text{ mA}$  when the cell was initially turned on. The gas generation for different cells was observed to be similar (Figure 36).

However, over the course of a 60 day measurement period the current density (and hence rate of gas evolution) decreased by over a factor of two for the highest initial current density setting ( $460 \mu A/cm^2$ ). Lower initial electrochemical currents (set by increasing the load resistor) produced a corresponding smaller relative decrease in current density with time.

#### 4.2.3 Conclusion regarding Nitrogen Generator

Nitrogen gas is electrochemically generated by decomposition of  $Li_3N$  powder mixed with carbon black. However, the decrease in current density -which is equivalent to the nitrogen generating rate-deteriorated with time. Reasons for the decrease include reaction between residual water and oxygen in the cell and  $Li_3N$  or polarization of the cell from charge build-up. Further investigations of these effects are needed to determine the cause of current density degradation.

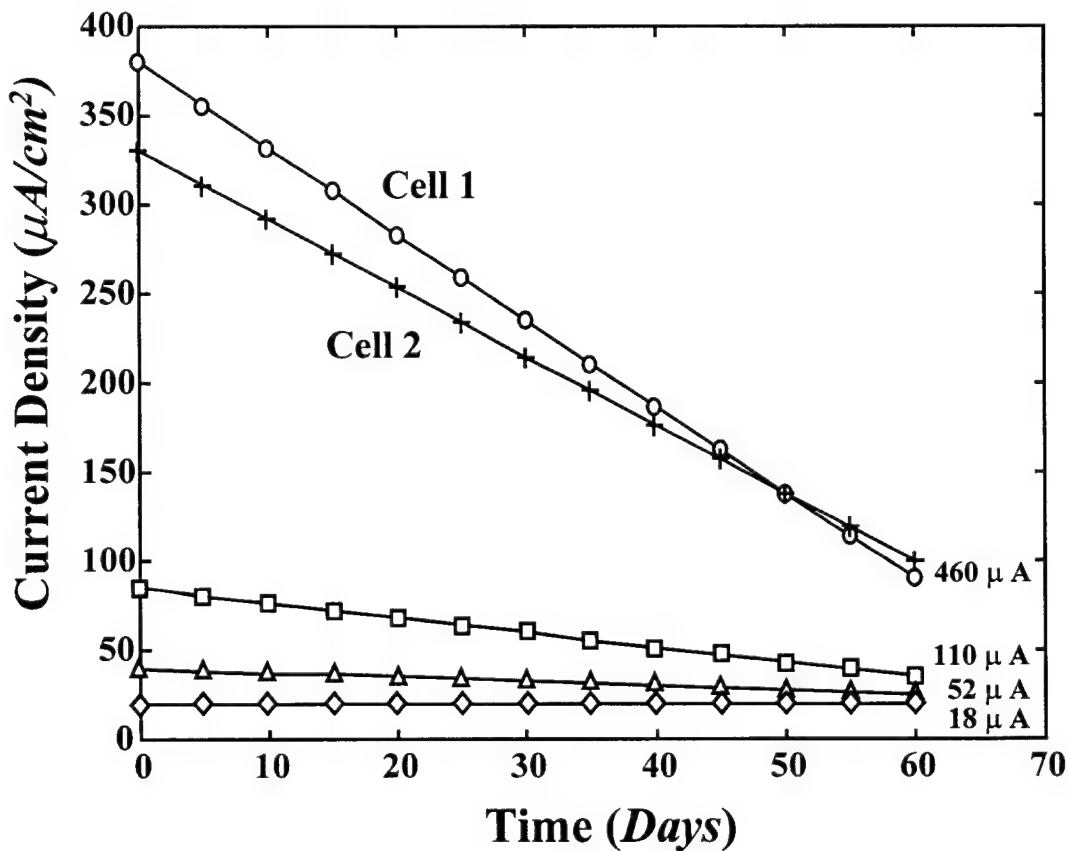
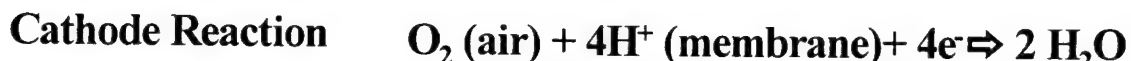


**Figure 36:** Cell current density as a function of time for different starting currents.

### **4.3 Oxygen gas controlled release capsule**

The poor long-term performance of the Li<sub>3</sub>N system and environmental toxicity of Li motivated us to consider alternative electrochemical gas generating schemes. As a promising alternative, we have developed an oxygen gas-generating device based on an electrochemical cell. In the cell (Figure 37), oxygen from the air is reduced to form water at a cathode attached to a membrane. Ions are transported across the membrane while water is oxidized and oxygen liberated at the anode, which is attached to the opposite side of the membrane. The steps involved in the electrochemical process are as follows:



### **Transport**

<b>Migration</b>	$4H^+$	<b>Anode <math>\Rightarrow</math> Cathode</b>
<b>Diffusion</b>	$2H_2O$	<b>Cathode <math>\Rightarrow</math> Anode</b>

which results in the transport of oxygen gas from the external air (or water reservoir) to pressurize the enclosed space defined by the first membrane.

#### **4.3.1 Electrochemical Cell Design**

A cation exchange membrane (Nafion 117 from Dupont) was utilized as a support for the electrodes, as a barrier between the air and the pump outlet, as a solid electrolyte through which protons can migrate under the influence of a potential gradient and as a media through which water can diffuse from cathode to anode. Platinum is the electro-catalyst for both anode and cathode. Electrodes are formed when an ink containing Pt is applied as a drop to the Nafion membrane and baked in an oven. This technique was developed previously by Yousheng Shen *et al.* and is detailed

in U.S. Patent No. 5,573,648. Since the Nafion conductivity is a function of the humidity, a water reservoir is integrated with the cell so the gas-generating rate is ambient-independent.

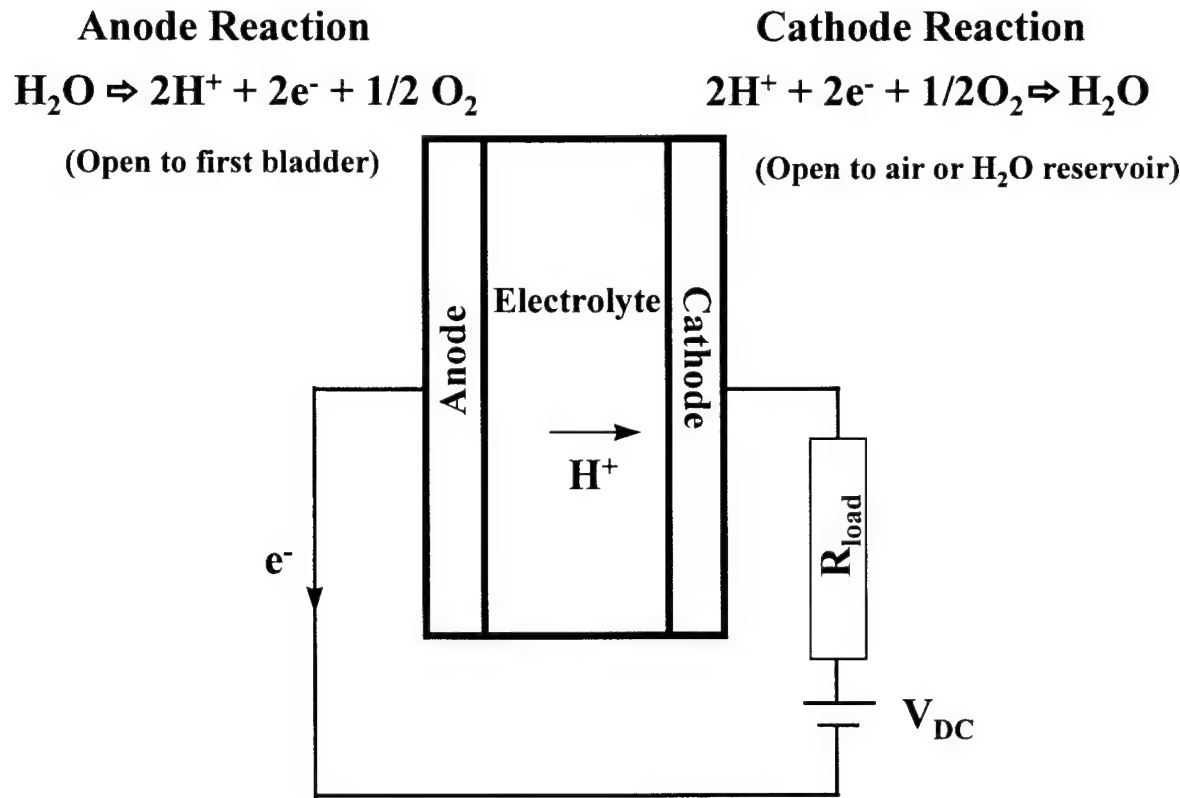


**Figure 37:** Schematic of electrochemical cell and reactions to generate oxygen gas at anode.

#### 4.3.2 Experimental Results

Application of  $1.5 \text{ V}_{DC}$  to the cell through a load resistor of  $1 \text{ k}\Omega$  resulted in a  $1 \text{ mA}$  of DC current that generated oxygen gas at  $5.5 \text{ cm}^3/\text{day}$  with only a small water drop as the reservoir. Only a small water drop is needed because of the high density ratio between gas and liquid states for the constituent gases. Figure 38 shows inflation of a membrane with the oxygen gas generated by the cell after three hours of operation at  $2.5 \text{ mA}$  current and  $1.5 \text{ V}_{DC}$  drive voltage. Integration of a water reservoir with the electrochemical cell is clearly advantageous to keep the gas evolution rate large and constant (Figure 39). This is not to say, however, that the pump can't be operated with ambient humidity but a performance decrease is expected that would be directly dependent on relative

humidity. Ambient temperature also influences rate of gas evolution but this dependency has yet to be explored.

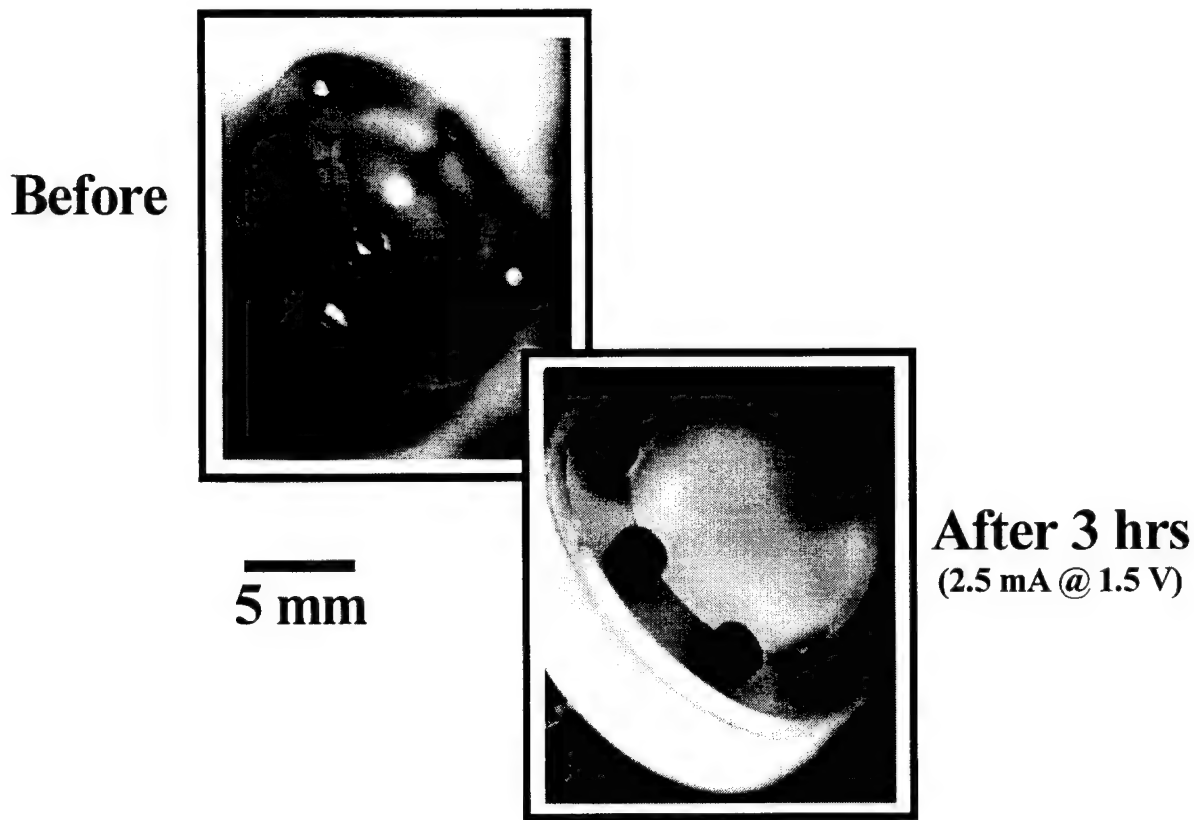


**Figure 38:** Inflation of a membrane with oxygen gas generated by the miniature electrochemical cell.

The number of moles of gas generated follows Equation 21, and for a constant current should be linear with time assuming no back pressure from the gas reservoir. Figure 40 shows the volume of gas measured as a function of time for two different currents through the cell. Comparison with the theoretical predictions from Equation 21 is excellent for the two cell currents considered. The slope of the  $V$  vs.  $t$  curve, as seen from Equation 21, equals the number of moles of gas produced per amount of charge passed through the cell. As an example, consider the amount of gas generated using a current of  $37 \mu\text{A}$ . Over a 5-day period,  $35 \mu\text{M}$  of oxygen gas was generated from  $16\text{C}$  of charge passed through the cell. The number of moles of gas produced per unit charge is therefore  $2.18 \mu\text{M/C}$  and is in good agreement with the prediction from Equation 21 ( $2.59 \mu\text{M/C}$ ) when the number of ionization electrons per molecule equals 4. A similar result holds for the smaller cell current of  $13 \mu\text{A}$ .

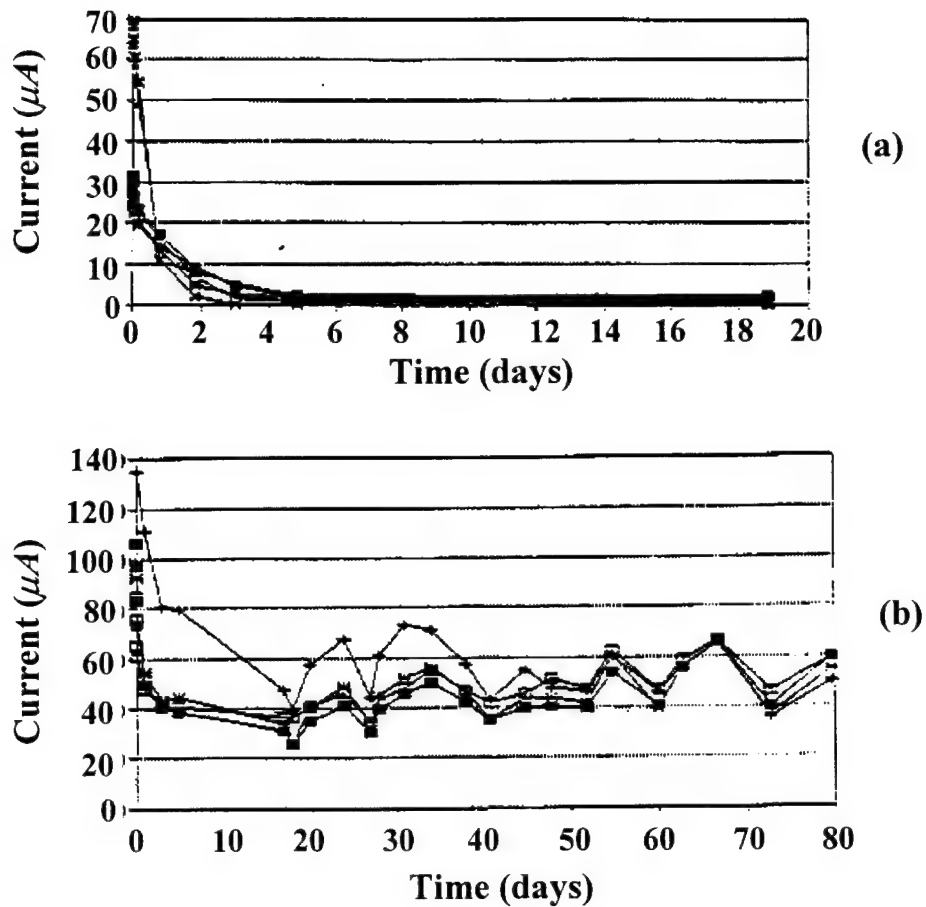


**Figure 39:** Comparison of electrochemical cell current as a function of time without (a) and with (b) water reservoir. Note that the rate of gas production is proportional to cell current.

The average rate of gas production for the two currents are  $0.19 \text{ cm}^3/\text{day}$  and  $0.065 \text{ cm}^3/\text{day}$  for the  $37 \mu A$  and  $13 \mu A$  drive currents, respectively. As expected for a linear model, the ratio of gas production rates and cell currents are similar (2.8 and 2.9, respectively). From this result we predict the pumping rate for a  $2 \text{ mA}$  cell current to be approximately  $10 \text{ cm}^3/\text{day}$  @ STP. This estimate is about a factor of two times larger than was actually observed for the  $2 \text{ mA}$  current ( $5.5 \text{ cm}^3/\text{day}$ ) and we speculate that the difference could be from the build up of bladder pressure that begins to decrease the mass flow of water through the Nafion membrane. Evidently, further work is needed to clarify the relationship between gas cell pressure and pumping rate.

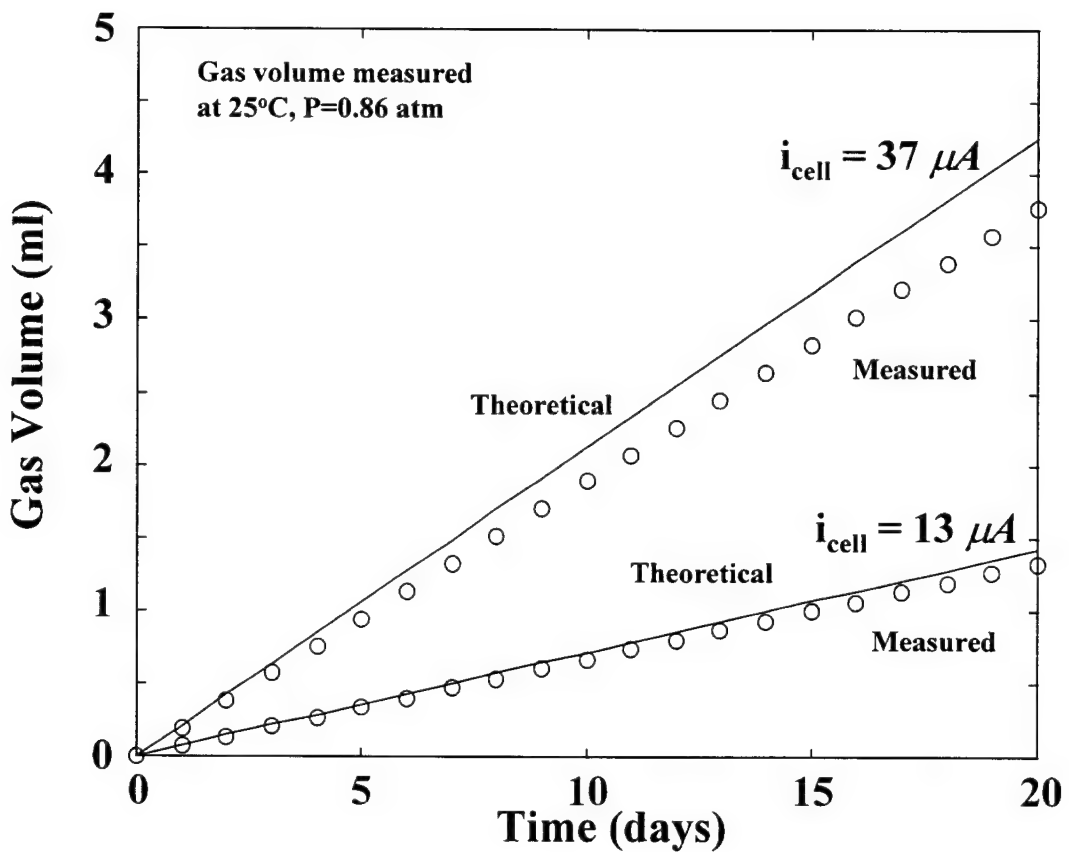


**Figure 40:** Volume of gas produced as a function of time for two different electrochemical cell currents.

A final example of this pump technology is a demonstration of its scalability for pumping larger volumes. Figure 41 demonstrates this concept where twenty electrochemical cells have been connected in parallel to a common manifold. Electrically connected in parallel, a  $2 \text{ mA}$  current is driven through each cell to generate sufficient oxygen gas to fill a bladder that is approximately  $\times 400$  larger in volume than a single electrochemical cell. As predicted, the larger volume is filled with gas generated by the cells in approximately 1.5 days of operation.

#### 4.3.3 Conclusion regarding oxygen gas pump

We have demonstrated a miniature pump that involves the electrolysis of water after diffusion through a Nafion membrane. A voltage established between Pt electrodes on either side of the membrane allow for the rapid movement of protons through the membrane (from anode to cathode)

and for the slower diffusion of water from an external reservoir to the anode located inside an enclosed volume (the first bladder). At the anode, water is disassociated into oxygen gas and hydrogen ions. The oxygen gas fills the volume while the electric field between the electrodes causes the free charge to migrate across the membrane. Charge neutrality is maintained by the flow of electrons into the anode from the external voltage source.

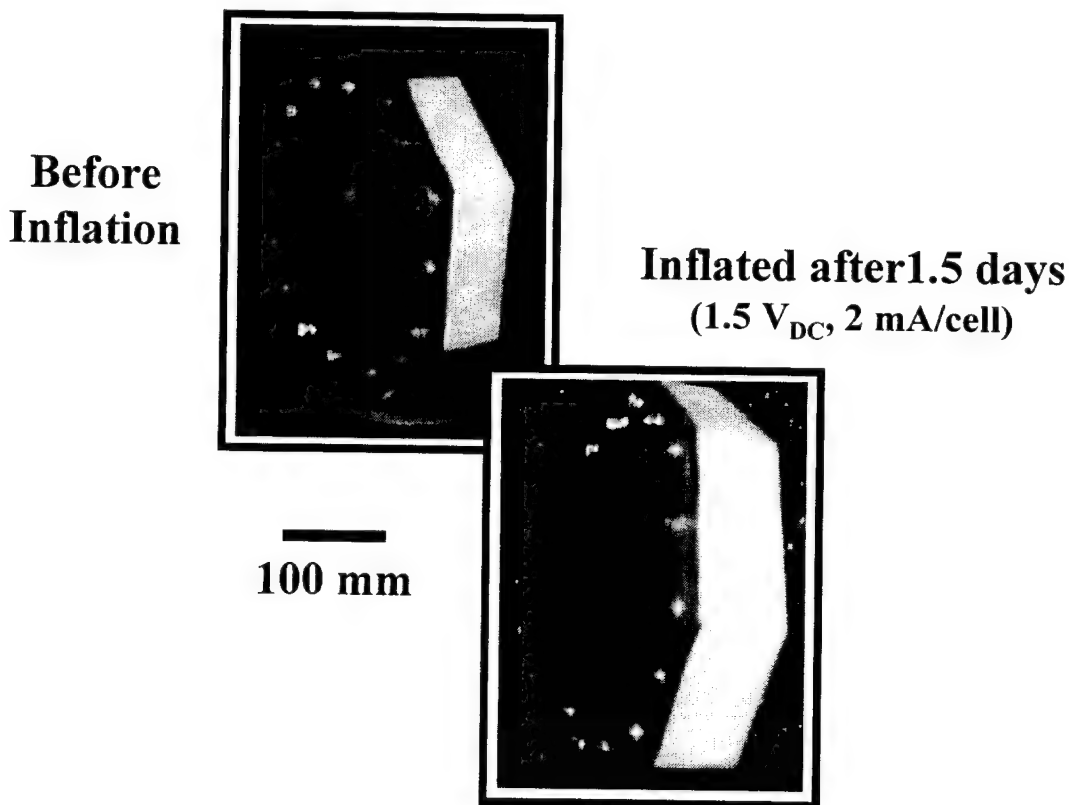


**Figure 41:** Demonstration of scaling of electrochemical gas cell for pumping large volumes. Twenty electrochemical cells are mounted with outlets that open into a common manifold. The large volume is filled with oxygen gas in approximately 1.5 days of pumping @ 2 mA per cell.

This process with a water reservoir was shown to produce oxygen at a constant rate (approximately  $5 \text{ cm}^3/\text{day}$ ) over an extended time period (greater than sixty days) for a constant current (2 mA) driven through the cell. The technology was demonstrated to be scalable to fill a volume almost three orders of magnitude larger than an individual electrochemical cell. These

miniature cells are therefore well suited for their original application of a voltage (or current)-controlled release capsule. Future work in this area includes addition of a second membrane filled with a liquid to be expelled in a controlled manner to the electrochemical cell and a feasibility demonstration of the controlled release concept in a target application. Furthermore, the pumping rate of the cell could be put under servo-control with respect to a feedback derived from a chemical sensor. Thus the controlled release of, for example, an antidote to a detected pathogen could be made possible with the gas cell technology. Its small size and low energy consumption ( $< 1 \text{ mW}$ ) make the device suitable as a portable unit.

#### ***4.4 Proposed applications and future work***

Applications in the realm of CBW sensors include release of compounds for reaction with those already present in the gas, fluid or aerosol stream passing through the sensor. The release could be synchronized with the intake stroke of the air inlet pump or it could be in response to the output of a chemical sensor. For example, a chemical sensor detects the presence of a CBW agent and the capsule releases the amount of antigen necessary into a mask worn by the soldier or into the environment local to the soldier to neutralize the CBW agent.

Civilian applications are also numerous and include controlled release of perfume over an extended time period or in response to a signal from a chemical sensor as can be imagined for bathroom air fresheners or extended wear perfume dispensers. Similarly, instead of perfume the capsule could release a bactericide or a fungicide into the air stream of a building's air conditioning system to keep the concentration of pathological bacteria and/or fungi below an acceptable level. Another application area is in the controlled delivery of drugs over an extended period. The controlled release capsule can be viewed as a simple pump with no moving parts that is advantageous over present-day micropump technology because it is a simple and hence inexpensive device that can deliver drug doses simply and accurately with a high reliability.

## 5.0 Shape memory alloy pumps

### 5.1 *Introduction*

BOMEC's extensive experience with shape memory alloys (SMA) for robotics applications, and the good match between the SMA properties and those required for inlet pump prompted us to design, build and evaluate two prototype pumps that use nickel titanium (NiTi) SMA fibers as actuators. Compared to the conducting polymer work, the SMA pump is primarily a developmental effort because of the accumulated much knowledge regarding the static and dynamic electro-mechanical properties of NiTi fibers both in this lab and in others. Thus the NiTi SMA fiber technology is an intermediate (and perhaps complementary) actuator technology suitable for creation of air inlet pumps that could be immediately useful to DARPA while the technical issues regarding conducting polymer actuated pumps are resolved.

Two different pump designs have been explored in this prototype evaluation . These designs were, in turn, limited to considering only those pump mechanisms that seem to be best suited for forcing a gas into a liquid. The first is based on the bellows action of a stiff membrane actuated by an antagonistic pair of NiTi fibers or springs. Advantages of the bellows pump design are many and include a large volume of gas displaced per pump stroke, a high pumping rate if the stroke rate is rapid, a small size and weight. However, high-pressure heads are not easily attained with bellows pumps and either passive or active valves are required to ensure uni-directional fluid flow.

The second design is based on peristaltic action. NiTi fibers are mechanically configured in a one-dimensional array such that their sequential contraction squeezes a bolus of material through a flexible tube. A variety of materials can be pumped in this manner, including gases, liquids of different viscosities and slurries. A peristaltic pump operates without valves, which keeps the pump design and construction simple. High outlet pressures can be generated by the peristaltic action, but with the potential disadvantage of a pulsating flow. However, the flow pulsation could be advantageous if delivery of a precise and discrete quantity of material is desired. Additionally, the modulated mass flow when coupled with a detector technology could be used as part of a signal-processing scheme to increase detection sensitivity of materials in the flowstream. Multiple lines can be multiplexed into a

single pump configuration to either increase the rate or the diversity of materials (i.e. a different material per pumping channel) pumped.

This section of the report is organized as follows. After a brief introduction, the properties that make SMAs a suitable pump actuator will be discussed and previous applications of SMA as pump actuators overviewed. Next, the design of the bellows and peristaltic pump are given, with the experimental set up and results that quantify the pump operation. Finally, this section of the report concludes with a summary of the work required to reduce the physical size and energy consumption of the pumps to make them field deployable as the air inlets to a CBW sensor system.

## 5.2 *Overview of SMA actuators*

### 5.2.1 Principle of Operation

Arne Ölander reported the first observation of shape memory transformation in 1932 in a gold-cadmium (Au-Cd) alloy. He described the rubbery feeling of the alloy without actually observing the shape memory effect. Chang and Read discovered in 1951 that an alloy of gold and copper would return to its pre-deformed state when heated after deformation. A few years later in 1954 Basinski and Christian observed the same effect in an indium-titanium alloy, as did Buehler, *et al* (in 1965) who worked with a nickel-titanium (50% Ni, 50%Ti) alloy. These researchers coined the term "Shape Memory Effect" to describe the phenomenon. Numerous SMAs have been studied<sup>16</sup> but the most extensively studied SMA is the NiTi alloy (typically 50% Ni).

Otsuka and Shimizu in 1970 showed that the shape memory effect was caused by a martensite to austenite phase transition. This phase transition occurs with different kinetics, over a band of temperatures. At low temperatures (i.e. below the phase transition temperature band) the NiTi has low crystal symmetry and can be readily plastically deformed. This state is alternatively called the martensite phase or the R-phase (because rhombohedral crystalline structures predominate). When heated to temperatures above the phase transition band the NiTi transforms to a higher symmetry crystalline structure, called the parent or austenite phase, which has the same distribution of atoms as

---

<sup>16</sup>Funakubo, H. *Shape memory alloys*. New York, NY: Gordon and Breach, 1987.

that found before the plastic deformation. Fibers can be "trained" to contract as they undergo a martensite to austenite phase transition with heating. Expansion to the original fiber length then occurs when the SMA is cooled to its martensitic phase again.

Ohmic heating is a convenient means to heat rapidly a NiTi fiber to above the transition temperature. Static stress is developed with a constant current through the fiber while dynamic stress (and strain) is generated by the fiber on stimulation by a current pulse. The contraction time of NiTi is governed by the amplitude of the current pulse (and hence the heating time) passed through it. By using large current pulses, this contraction time can be made very short<sup>17</sup>. The rate limiting part of the NiTi contraction and expansion cycle is in the relatively long time required for NiTi to cool and return to its original length. The cooling time is governed by thermal diffusion and the latent heat of

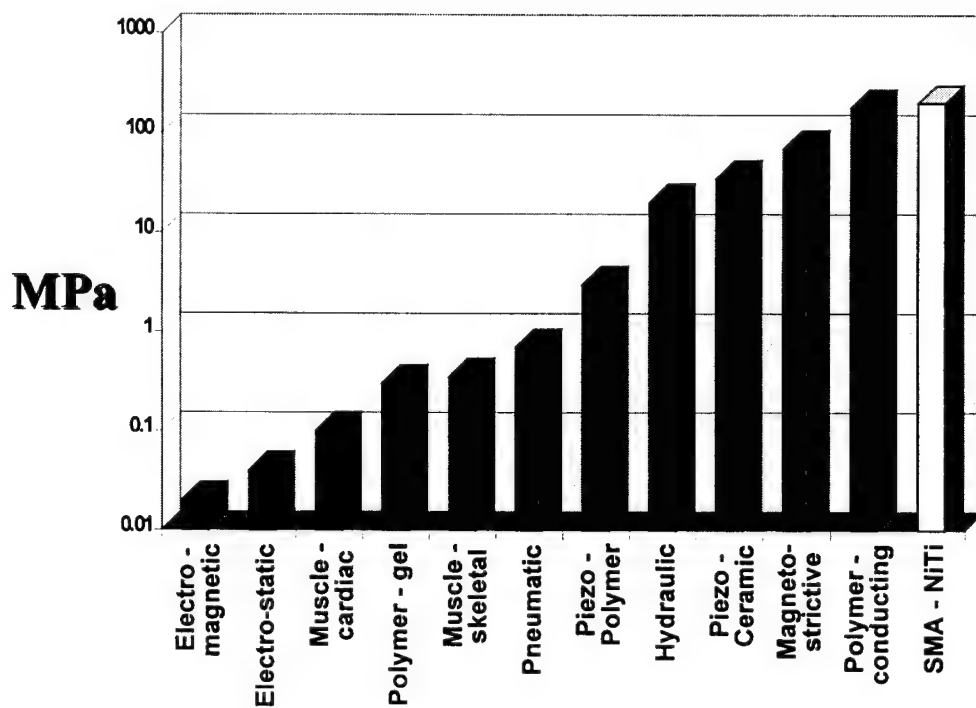


**Figure 42:** Comparison of maximum stress across different actuator technologies. Note that SMA can generate stress levels that exceed such conventional actuator technologies as electromagnetic motors by  $>10^4$  and piezoelectric ceramics by a factor of 10.

---

<sup>17</sup>Hunter, I.W. and Lafontaine, S. Shape memory alloy fibers having rapid twitch response. US patent 5,092,901, 1992.

transformation of the phase change between the austenite and martensite phase<sup>18</sup>

Several reviews (Hunter and Lafontaine<sup>19</sup>, Hunter<sup>20</sup>, Hollerbach et al.<sup>21</sup>) comparing actuator technologies concluded that, aside from their low electromechanical efficiency, SMAs (and in particular NiTi) are a material well-suited for robotics applications. Indeed, similar considerations hold for their application as actuators in pumps.

The first actuator property important to pump operation is the stress produced by different actuator technologies. According to Figure 42, NiTi fibers fare quite well when compared against other types of actuators usually considered for pumps. Capable of generating a stress greater than 200 MPa, this maximum stress is  $>10^4$  that of electromagnetic actuators and exceeds piezoelectric ceramics by over a factor of 10.

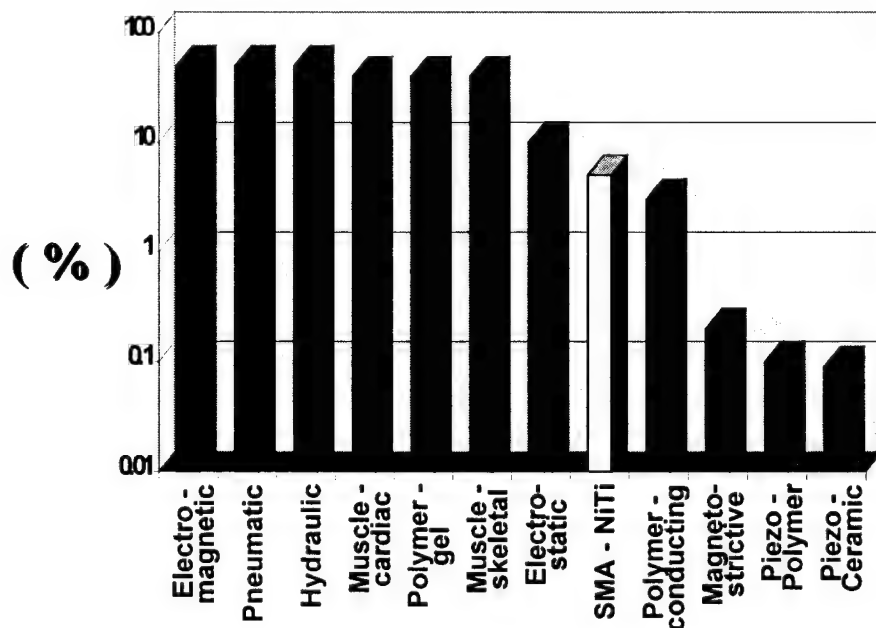


**Figure 43:** Comparison of maximum strain across different actuator technologies. SMA fibers are within a factor of 10 of electromagnetic, pneumatic and hydraulic actuators and over a factor of 100 times larger than piezoelectric ceramics.

<sup>18</sup> Ikua, K. Micro/miniature shape memory alloy actuator. *IEEE Micro Electro Mechanical Systems*, 1990, 3, 2156.

<sup>19</sup> Hunter, I.W. and Lafontaine, S. A comparison of muscle with artificial actuators. *Tech. Dig. 5th IEEE Solid State Sensor & Act. Workshop* 1992, 5, 178.

<sup>20</sup> Hunter, I.W. Novel actuators for use in robotics and tele-robotics. *Report Prepared for the US Office of Naval Research* 1990.

<sup>21</sup> Hollerbach, J.M., Hunter, I.W. and Ballantyne, J. A comparative analysis of actuator technologies for robots. *Robotics Review*, 1991, 301.

A second actuator property of importance in pump design is the maximal dimensional change experienced by the actuator normalized with respect to its resting length. Plotted in, Figure 43 the maximum strain that SMA fibers can produce -typically 8% for NiTi alloys and 15% for monocrystals- is within a factor of 10 of electromagnetic actuators and almost 100 times greater than piezoelectric ceramics. This large strain must be balanced against a commensurate decrease in the number of contraction cycles the fiber can be cycled through at that strain. For the strain quoted above, the number of contraction cycles is about  $10^5$ , while at smaller strains (<2%) yield cycle lifetimes  $>10^7$ . The limited lifetime at high strains can be circumvented somewhat through implementation of design strategies that capitalize on the fiber's low cost and small size. Such strategies include fiber redundancy or recruitment of fibers placed in parallel as individual fibers fail.

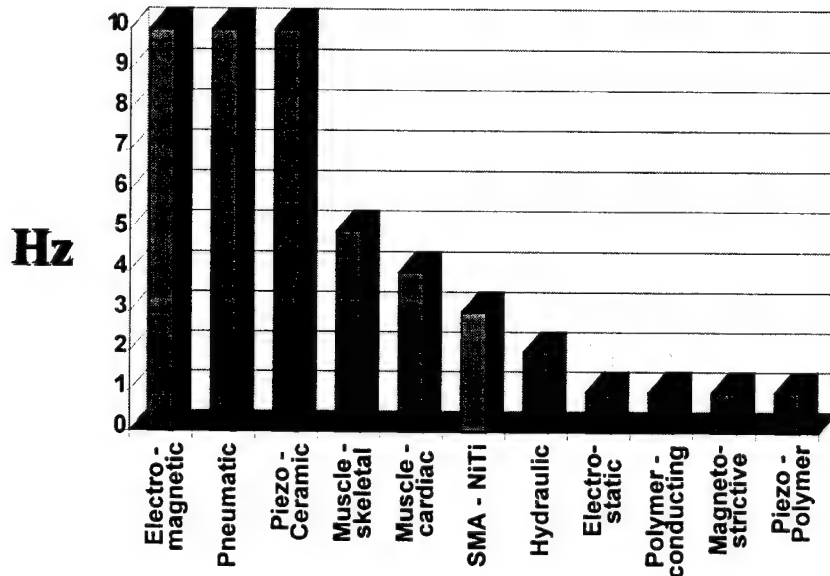


**Figure 44:** Maximum strain rate for different actuator technologies. SMA fibers exhibit strain rates three times larger than electrostatic actuators but smaller than electromagnetic, pneumatic and piezoceramics by the same amount.

Zero load strain rates indicates how rapid the actuator changes dimension and in conjunction with the peak stress, determines the maximum power output per mass of actuator. The higher the power output per unit mass, the more desirable the actuator is for use in a pump. Comparison of peak strain rates (at zero load) (Figure 44) shows NiTi fibers have maximum strain rates comparable to muscle (about  $3 \text{ s}^{-1}$ ) and are smaller by a factor of 3 than piezoceramics and electromagnetic actuators. As an

example of the contraction times possible with NiTi fibers, if the fiber is immersed in a coolant and then rapidly heated by a brief current pulse passed through it, the fiber will contract and then expand again in < 100 ms. However, contraction times in air can be substantially longer -of the order of several seconds- because of the over ten times smaller thermal impedance of air compared with water.

The peak power per unit mass generated by the NiTi fiber occurs at about 40% peak stress (cf. muscle 33%) and is over 50 kW/kg (Figure 45). This far exceeds electrostatic actuators -about 1000 times- and is comparable to piezoceramics. However, it must be remembered that the peak power/mass and peak generated stress values mentioned do not include the mass or volume of the cooling system in which the fiber is immersed. A fair comparison with other types of actuators requires this.

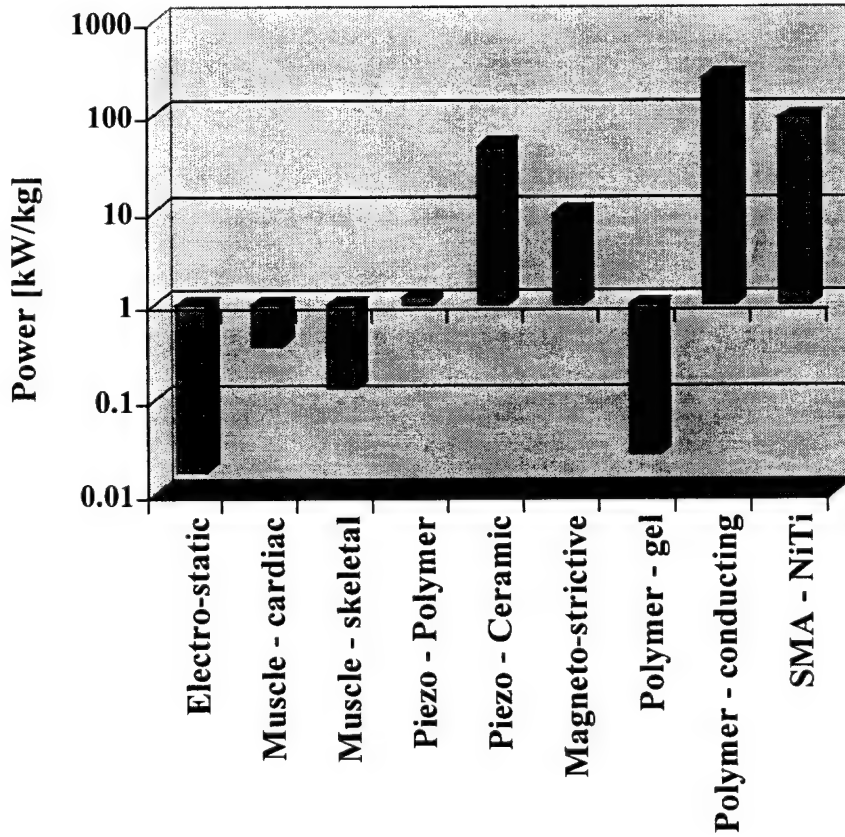


**Figure 45:** Comparison of power per unit mass across different actuator technologies.

The efficiency with which NiTi converts thermal energy to mechanical energy varies from <2% to >3% when there is full recovery of the heat associated with the thermal capacity. At present, no

method has been devised to recover this heat while retaining fast cycling. This is because current methods for producing relatively fast NiTi cycling involve continuous flow of a coolant over the NiTi. As seen in Figure 46, SMA electromechanical efficiency is substantially lower compared with other actuator types.

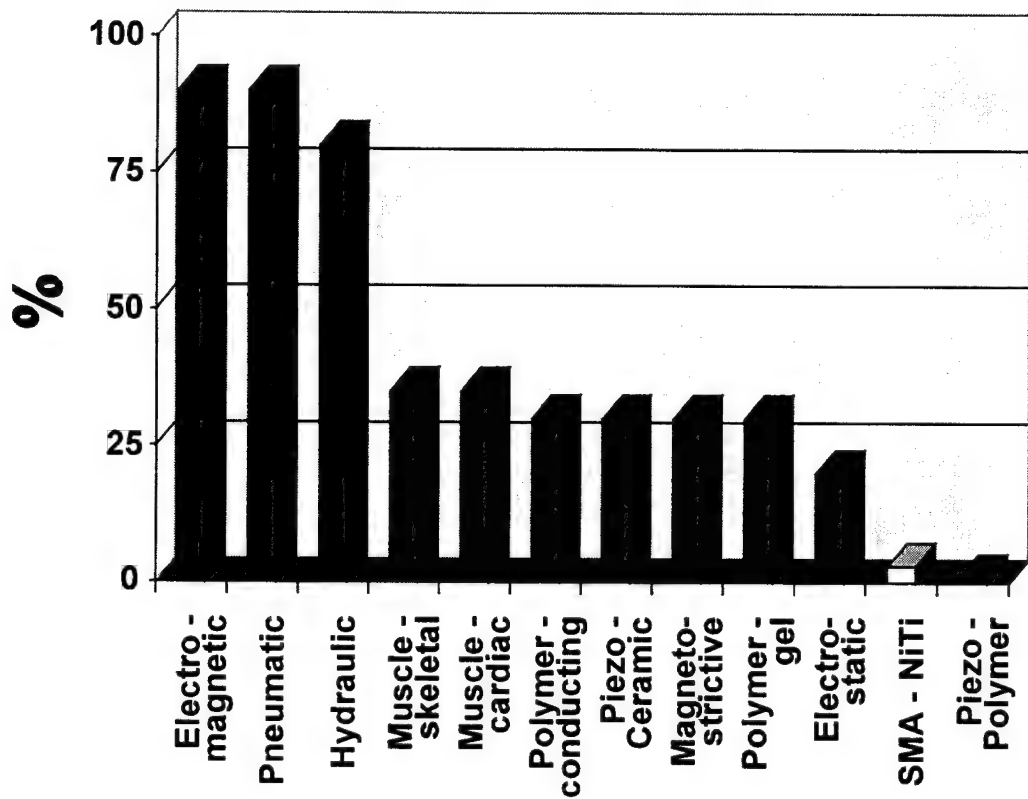


**Figure 46:** Comparison of electromechanical efficiency across different actuator technologies. Note that SMA efficiency is substantially lower -by about a factor of 10- than other pump actuator technologies.

Electromechanical attachment or mounting of NiTi fibers in a mechanism is another factor that has hindered widespread application of SMA as actuators. It is very difficult to bond, solder, braze or weld NiTi fibers, and since the properties of the alloy depend critically on the exact relative concentrations of each element, any slight deviation that could be a consequence of the joining process can result in very different material properties. Since titanium is a highly reactive material that readily oxidizes, soldering NiTi fibers to other materials usually results in a brittle interface due to the

migration of atoms at the interface or the oxidation of titanium and so joints readily break. When a NiTi alloy is heated its shape memory effect or superelastic effect is normally lost. It is therefore difficult to use any high temperature process to join them. Welding, brazing or soldering involves heating the NiTi alloys whose properties subsequently end up being severely degraded. Brazing can be effective, however, in joining two NiTi alloys, providing of course that the shape memory effect is not lost, because diffusion of metal atoms between parts does not change the net stoichiometry and embrittlement is not a problem.

It is impossible to glue, cement or bond NiTi alloys because of the large strains and stresses placed on the joint associated with the large strains per cycle of the NiTi. After a few cycles of contraction and expansion they will crack and fracture all known adhesives.

Clamps and screws normally used to attach metals and alloys rely on the forces produced by the elastic deformation of the material which is normally limited to 0.1% in most materials. Shape memory alloy materials will typically go through 8% dimensional changes when phase transformations occur and will readily release themselves from clamps and screws when they contract or will loosen their connection after a few cycles due the huge stresses arising from hysteresis after repeated contraction and expansion. The most commonly used technique to mount NiTi fibers consists of winding the fiber several times around an attachment to use the capstan effect such that the fiber tension itself increases the strength of the attachment. However, a capstan tends to consume a large amount of space and mass relative to the fibers it holds and is not well suited for miniaturization.

In our work, we used a technique invented by Hunter and Lafontaine<sup>22</sup> of electrochemically metallizing the NiTi fibers for subsequent electromechanical attachment through soldering. We have found this technique results in reliable, high conductivity joints with yield strengths exceeding 540 MPa (27 N for a 250  $\mu m$  diameter fiber). Although not as high as the fiber yield stress, this is still 2.7 times higher than the maximum recommended stress for a fiber of this size in normal applications.

A further problem with shape memory alloys is that they can be very fast when contracting but the relaxation speed is normally limited by heat dissipation from the fiber. The

---

<sup>22</sup> Hunter and Lafontaine, Method of joining NiTi fibers, Patent Pending.

contraction process can occur in milliseconds when the fiber is quickly heated with large current pulses. In air, however, depending on the ratio of surface area to volume the relaxation will normally take several seconds in air. Heat dissipation can be enhanced by designing actuators with a number of small fibers that can dissipate heat more rapidly than larger fibers, by using water or other liquids for cooling, or by using thermal pumps such as Peltier devices for active cooling.

The response of NiTi alloys to mechanical, electrical or thermal commands is highly nonlinear. The shape change occurs very rapidly over a very narrow temperature range and is difficult to control precisely. There is a hysteresis typically of 15 °C to 30 °C between the temperature at which the fiber contracts and the temperature at which expansion occurs. In addition, NiTi materials can go one or two intermediate phases between austenite and the low-temperature martensite. Each phase change occurs with a considerable latent heat and the martensitic transformations are highly exothermic. In all cases they generate work when contracting but no appreciable amount of mechanical work can be obtained from shape memory materials in the cooling process. In cases where only small forces and displacements are required there is an intermediate secondary phase transformation where the hysteresis is limited to approximately 1.5 °C where continuous control is more readily achieved. Because of this highly non-linear mechanical behavior, new control strategies must be devised if feedback control of the actuator is desired. In our work, the actuators can be operated open loop thus obviating the need for servocontrol.

### ***5.3 Applications of NiTi Shape Memory Alloys***

Following the discovery of NiTi alloys, a number of attempts were made to use them in practical applications. NiTi alloys have been used in preference to other shape memory alloys in industrial applications because of their larger recovery strain and stress, their longer repetition life, their good resistance to corrosion, and relatively low cost. Table 1.0 summarizes a survey of the patent, scientific and engineering literature over the past three decades for applications of NiTi alloys.

Field	Application
Electronic Equipment	Circuit breakers Zero force insertion connectors (ZIF) Disk-drive heads Cell phones antennas
Automotive	Head lights actuation Noise reduction (damping) Radiator thermostat
Home and Textile	Circuit breakers (coffee makers, etc.) Underwire bra Permanent press shirts Air conditioners (louver actuation) Toys, ashtrays, etc. Ashtrays (low hot cigarette buts) Eyeglass frames
Food	Temperature extrema marker (thermomarker)
Smart Materials	Composite materials, building dampers
Robotics	Robotic actuators (grippers, arms, hands) Sealing Ring Actuator for camera
Machinery	Pipe joints Fixation mechanisms Valves
Medicine	Artificial joins, spines Vascular, esophageal and biliary stents Artificial heart Micro-pumps Guide wires for catheters Guidepins, localization hooks Blood clot filter
Space	Antenna releasing system Release mechanism and bolts Vibration damping during launching
Photography	Shutter mechanism for telescope CCDs.
Security Systems	Fire alarm and extinction actuators Anti-scald device Gas-valve lock

**Table 1.0:** Applications of Shape Memory Materials

Interestingly there are few reports of pumps that utilize shape memory alloy as the actuator. Lee<sup>23</sup> received a patent in 1997 for his invention of a piston pump based on mechanism that uses the SMA fiber to provide a force to move the piston in one direction and a passive spring that provides a bias force to return the piston to its start position. Young and Freidhoff<sup>24</sup> were also

<sup>23</sup> Lee, U.S. Patent No. 5622482, "Pump using shape memory alloys".

<sup>24</sup> Young, R. and Freidhoff, C., U.S. Patent No. 5659171, "Micro-miniature diaphragm pump for the low pressure pumping of gases".

awarded a patent in that same year for a diaphragm pump using a shape memory alloy sheet as the inlet pump to a mass spectrometer. A similar idea is employed by Huff<sup>25</sup> at Case Western Reserve University in the SMA diaphragm pump he invented for drug delivery. His prototype consists of a rectangular silicon chamber with one of the outer walls made of two thin layers of NiTi sheet sandwiched around a layer of silicon. The alloy changes shape when heated to above 60°C causing the chamber to expand. To operate the pump, a staggered pulse of electrical current passes directly through the sheet causing the sheet to alternately expand and contract the chamber. The expansion pulls fluid into the chamber through a passive polyamide intake valve and the contraction expels fluid through a similar exhaust valve. Pumping rates achieved to date are in the range of microliters per second.

#### **5.4 *Shape memory alloy air inlet pump***

We have investigated two mechanisms for pumping gas into fluid -the bellows pump and the peristaltic pump. In this section, we detail the design and construction of prototype bellow and peristaltic pumps fabricated using NiTi fiber actuators. The primary design criterion for either class of pump is a pumping rate greater than  $1\text{cm}^3/\text{min}$  of air into water. Secondary design criteria pertinent - but not critical to the acceptance or rejection of a prototype pump design- include maximum pressure head at pump outlet, power consumption and physical size. Indeed, optimization of these criteria (and others not listed) will take place in a second later phase of the development program.

##### **5.4.1 SMA Bellows pump-Version 1**

###### **5.4.1.1 Principle of Operation**

The basic idea behind the bellows pump is similar to that of a piston with two one-way valves. On the intake stroke, the outlet valve closes, the inlet valve opens and air is drawn into the piston chamber. As the piston moves to compress the cell, the inlet valve closes and the outlet valve opens. The increased pressure inside the chamber forces air out through the open outlet valve and air is expelled from the pump. As the piston returns to its starting position, the outlet valve closes, the inlet

---

<sup>25</sup> Design News, September 8, 1997, 14.

valve opens and the chamber is refilled with air from outside the pump. The volume pumped per piston stroke depends on the piston stroke length and cross-sectional area while the pumping rate depends on the interplay of a variety factors including fiber strain rate and power per unit mass. The maximum pressure generated by the pump is determined ultimately by the maximum stress generated by the fiber.

#### 5.4.1.2 Pump Design

A schematic of a SMA bellows pump fabricated from an antagonistic pair of NiTi springs is shown in Figure 47. One end of each spring is attached by Pb-Sn solder to a stiff, 0.5 mm thick brass shim plate to which is glued a thin (100  $\mu m$  thick), flexible polyethylene sheet. The film is mechanically held fast between two halves of an Al housing joined together by an O ring seal. Clearance between the plate ( $\phi = 22.2 \text{ mm}$ ) and the housing ( $\phi ID = 25 \text{ mm}$ ) is small to allow free axial motion of the plate and membrane while minimizing their lateral motion. The opposite ends of the NiTi springs are soldered to brass plates that cap each end of the Al housing. The brass caps are epoxied to the housing to make a leak tight seal.

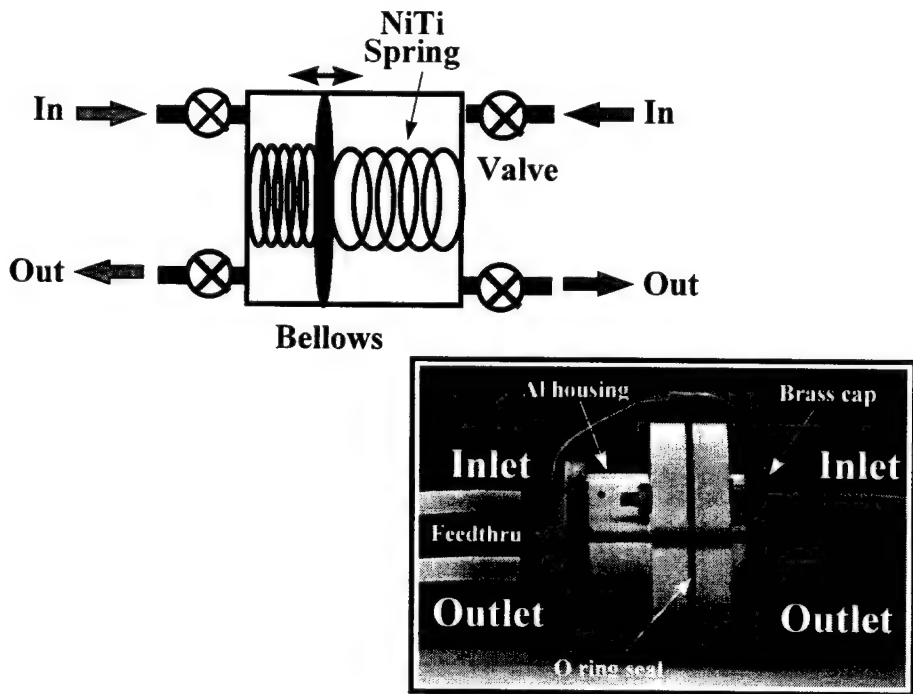


**Figure 47:** SMA bellows pump schematic and photograph showing detail of housing configuration.

Two pumping chambers are thus formed in this geometry and alternately contracting and relaxing the NiTi springs fill one chamber filled with air while the other is evacuated. Each chamber has its own pair of inlet and outlet ports with valves. The photograph of the pump in Figure 47 shows the external housing configuration.

Electrical connections to the fibers are made through the brass end pieces and a wire soldered to the brass membrane. With the membrane held at ground potential, a fiber spring is stimulated to contract when voltage is applied to its opposite end. The electrical resistance of each spring was  $1.28 \Omega$  (at room temperature) which means a voltage of  $1 V$  was needed to drive a maximum current of  $0.78 A$  through the fiber spring to achieve the desired level of stress and strain.

The springs are made from  $250 \mu m$  diameter NiTi wire capable of producing  $10 N$  of force and a nominal strain of 5%. The springs are fabricated by tightly winding the wire around a threaded rod with the desired thread pitch. The fiber on its mandrel is then heated above the transition temperature ( $500 ^\circ C$ ) for approximately 10 minutes. Once cooled, the wire takes on the helical shape of the mandrel and once deformed from this shape will return to it on heating.

In this bellows pump configuration, an antagonistic pair of “active” NiTi springs is preferred over a single fiber with a “passive” spring to provide the necessary restoring force. The stiffness of NiTi fiber changes by up to three orders of magnitude as the fiber is heated above its transition temperature.<sup>26</sup> NiTi springs can therefore be made alternatively to be very stiff when heated and flaccid when cooled. This is opposed to passive springs in which the stiffness is constant. Mounted as an antagonistic pair and alternately heating one spring while the other cools results in large axial forces applied to the membrane.

---

<sup>26</sup>Lafontaine, S.R. and Hunter, I.W. Time resolved stiffness of fast NiTi artificial muscle fibers. *IRIS – PRECARN IV Annual Conference*, 1994.

The volume displaced per pump stroke critically depends on the NiTi spring design. The spring must be able to generate sufficient force to overcome the intrinsic stiffness of the plate-membrane structure and its length change -under the combined load of the plate-membrane and pressure head necessary to force gas out of the pumping chamber- sufficient to reach the target volume change per pump stroke. A  $250 \mu\text{m}$  NiTi fiber can undergo about six contraction/relaxation cycles per minute in air. To achieve a target  $1 \text{ cm}^3/\text{min}$  pumping rate, each pump chamber must change volume by  $0.083 \text{ cm}^3$  per pump stroke. This corresponds to a plate displacement of  $0.2 \text{ mm}$  per pump stroke for a plate area of  $3.87 \text{ cm}^2$ . After several iterations, a  $4 \text{ mm}$  diameter coil having a pitch of  $2.6 \text{ coils/mm}$  and a length of  $8 \text{ mm}$  was found that generates a static force ( $2 \text{ N}$ ) and no load displacement ( $5 \text{ mm}$ ) which is more than sufficient to reach the target pumping rate. The estimated air volume displaced per pump stroke is  $1.93 \text{ cm}^3$  and at six contraction cycles per minute the estimated pumping rate is  $11.6 \text{ cm}^3/\text{min}$ .

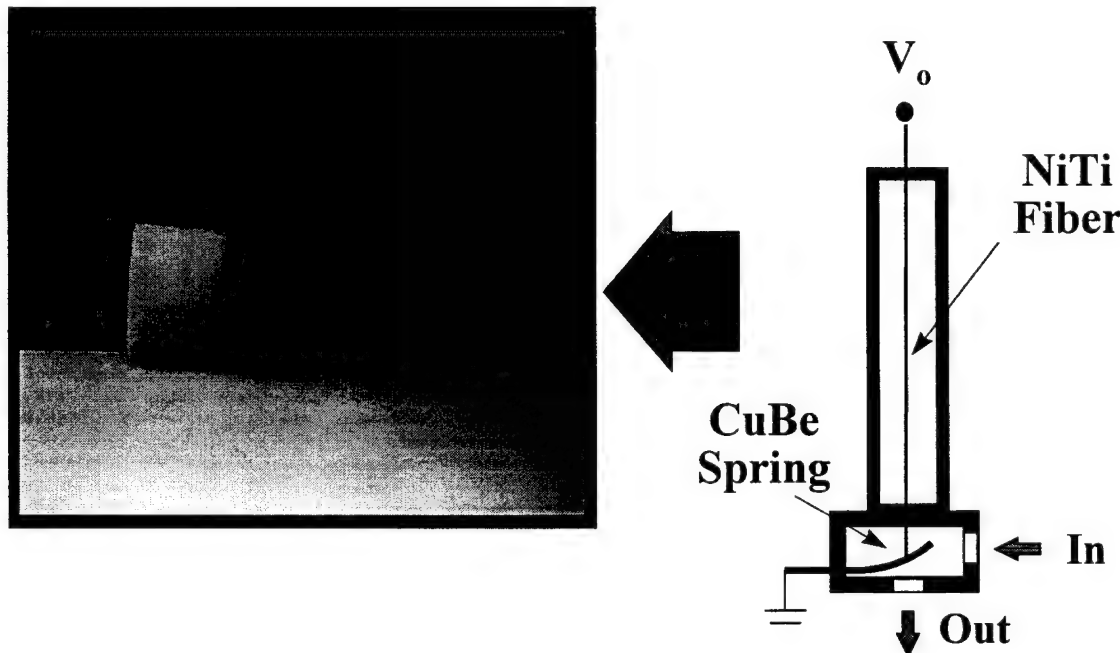


**Figure 48:** Schematic and photograph showing detail of NiTi fiber valve.

Establishment of uni-directional flow of air through the pump requires the opening and closing of the inlet and outlet valves be synchronized to the movement of the membrane. In the initial tests of the prototype, the valve operation was performed manually by blocking and unblocking the chamber

inlet/outlets in the appropriate sequence. Subsequently, a NiTi fiber-actuated valve was built and tested so that the valve sequence could be automated. Unfortunately, the large hysteresis observed in the NiTi spring resulted in marginal performance of this bellows pump configuration and integration of the pump and valves was not pursued further.

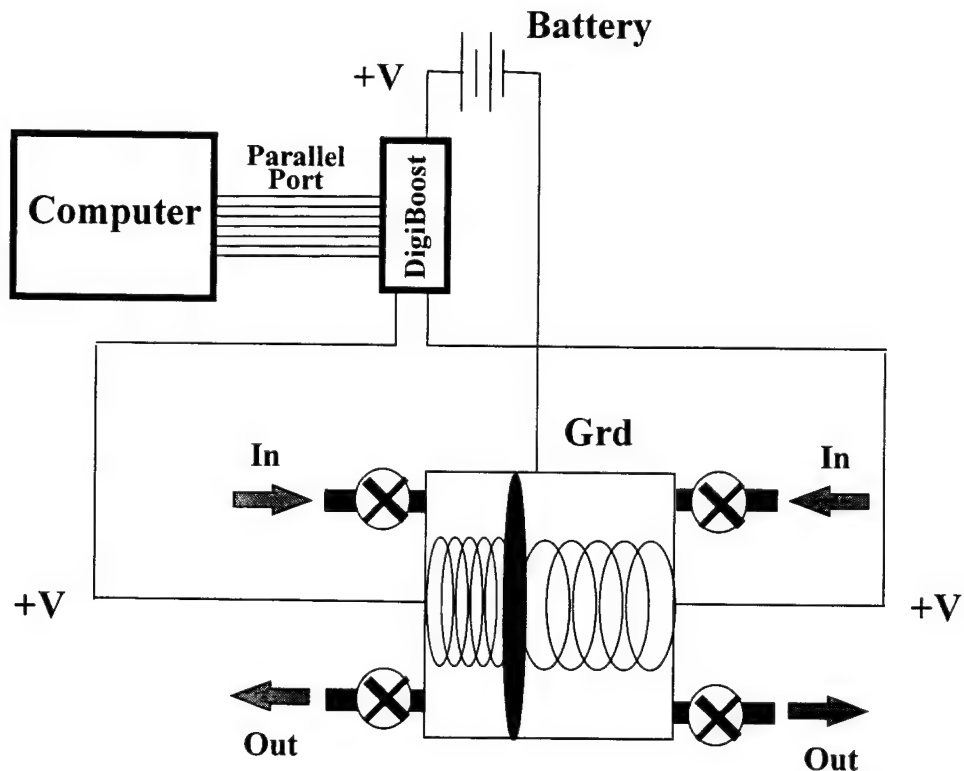


**Figure 49:** Schematic of experimental arrangement to evaluate bellows pump operation.

A schematic of the NiTi fiber valve (Figure 48) shows the valve is constructed from a single 50 mm long,  $250 \mu\text{m}$  diameter NiTi fiber placed inside a Delrin tube. One end of the fiber is soldered to a brass sheet capping the tube while the other end is soldered to a copper beryllium (CuBe) spring leaf. Glued to the spring leaf is a soft rubber pad that fills the valve outlet when the fiber is relaxed. To open the valve, an electrical connection is made to the spring leaf and the fiber is activated with  $0.75 \text{ A}$  of current sufficient to generate 5% strain in the fiber. The fiber contracts and lifts the pad away from the outlet thereby permitting gas to flow from inlet to outlet. When the fiber cools, the spring leaf provides the restoring force needed to reseat the pad in the valve outlet. The valve turn-on time was measured to be the time required to heat the fiber to its transition temperature -about 2

seconds- and the turn-off time was found to be about the same. The valve was found to be capable of withstanding an inlet-to-outlet pressure difference of  $>5\text{ atm}$  above ambient pressure without leaking.

#### 5.4.1.3 Experimental Results

The experimental arrangement assembled to evaluate the pump operation is shown in Figure 49. The pump is connected to a 12-volt battery through a digital high current switch called the DigiBoost<sup>27</sup>. This circuit switches up to eight channels under control by a computer through its parallel port. One or more fibers are connected to each channel and the battery voltage is applied to the fiber through a high current HexFet. With one HexFet per channel, the maximum current that can be switched by the DigiBoost per channel is over  $5\text{ A}$ . The switching time per channel is quite short - less than  $1\text{ ms}$ - and the time to cycle sequentially through all eight channels is less than  $3\text{ s}$ .

The volume of air pumped per pump stroke was measured by placing one of the pump outlets in an inverted graduated cylinder filled with water and observing the volume of water displaced by the air expelled from the pump per stroke. With  $0.78\text{ A}$  per spring and equal time periods ( $2\text{ s}$ ) for the fiber heating and cooling periods, an average pumping rate of  $2\text{ cm}^3/\text{min}$  was observed. Increasing the time per contraction cycle saw no increase in the volume displaced per contraction cycle while decreasing the time to less than  $2\text{ s}$  saw a proportional decrease in pumped volume.

The maximum pressure generated by the pump was measured by observing the change in water level in a capillary tube with one end immersed in a water bath and the other end attached to one of the pump inlets. As the pump evacuates one end of the tube, the pressure difference across the liquid in the tube causes the water column height to increase with decreasing pressure and decrease with increasing pressure. Thus, both the inlet and outlet pump pressures can be measured in this manner. The inlet and outlet pressures were measured to be essentially the same at  $0.64\text{ kPa}$  and  $0.51\text{ kPa}$ , respectively.

#### 5.4.1.4 Conclusion-Version 1 Bellows pump

A bellows pump based on the “push-pull” mechanical arrangement of an antagonistic pair NiTi springs was built and its operation evaluated. The measured pumping rate was a factor of two larger

---

<sup>27</sup> Mirage Technologies, Inc., Newton, MA.

than the target pumping rate of  $1 \text{ cm}^3/\text{min}$ . The measured pressure head for both the pump inlet and outlet were approximately the same at  $640 \text{ Pa}$  and  $510 \text{ Pa}$ , respectively. The measured volume displaced per contraction cycle,  $0.095 \text{ cm}^3/\text{contraction}$ , is substantially less than the theoretical estimate based on the measured spring displacement of  $5 \text{ mm}$ . One possible explanation is that the stiffness of the plate-membrane structure was, in fact, larger than originally estimated and the force produced by the spring was insufficient to generate the estimated displacement. Another factor could be a shift in the stress-strain properties of the fiber if it is kept for too long above the transition temperature under load. This could result in a permanent elongation of the spring, thus decreasing the maximum force and displacement available for moving the bellows.

#### 5.4.2 SMA Bellows Pump – Version 2

The NiTi spring-based bellow pump has a pump rate limited by the low force and slow contraction velocity inherent to the NiTi spring. In an effort to overcome this limitation, a second bellows pump was built based on NiTi fibers mounted in parallel. Similar to the first bellows pump configuration, the second bellows pump has two pumping chambers with air flow in to and out of the chambers controlled by passive check valves. The actuator configuration and operation is such that the filling and evacuation of each chamber are  $180^\circ$  out-of-phase with respect to each other.

Figure 50 is a schematic diagram of a macroscale version of the bellows pump. A large scale version of the pump was built to verify the design concept before attempting to miniaturizing the pump design. Two pumping chambers at either end of a  $50 \text{ mm}$  diameter Plexiglas cylinder are formed between the cylinder end caps and a  $1 \text{ mm}$  brass plate epoxied to a silicone rubber membrane stretched across the cylinder opening. A small annulus ( $5 \text{ mm}$  wide) of membrane between the inside wall of the cylinder and the brass plate ensures flexure of the membrane over the displacement range of the NiTi fibers. A  $10 \text{ mm}$  diameter Delrin rod connects the brass plates at opposite ends of the cylinder.

Two sets of  $200 \text{ mm}$  long NiTi fibers are placed inside the cylinder and for each set of fibers, one end is soldered to a brass plate while the other is mechanically attached to an aluminum disk placed inside the Plexiglas cylinder. The fibers are distributed such that when they are stimulated, a uniform force is applied to a brass plate. Stimulation of one set of NiTi fibers occurs when an electrical

potential is applied between one of the brass plates and its opposing Al disk. The plate is then displaced by an amount equal to the length change of the stimulated NiTi fiber.

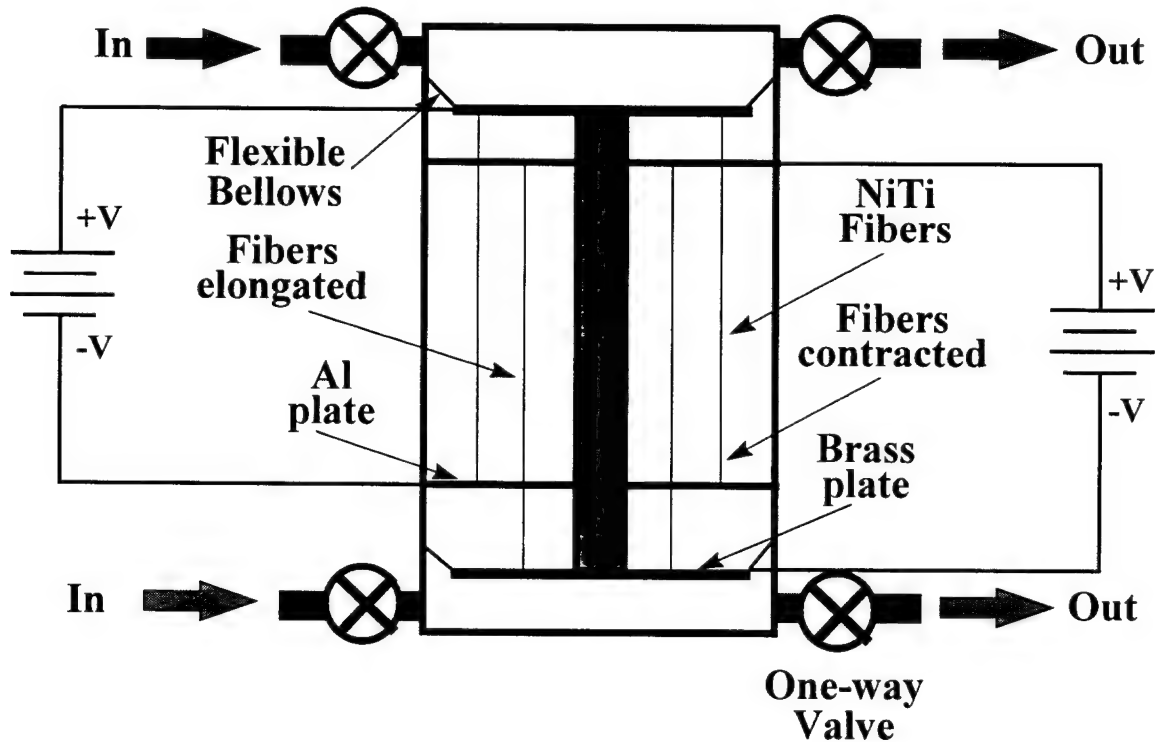


**Figure 50:** Schematic showing second version of NiTi bellows pump

Passive check valves were constructed from 10 *mm* diameter Plexiglas cylinders with an axially drilled 2 *mm* diameter hole. A flap of Mylar tape over the hole forms a vacuum seal when a pressure difference is imposed across the valve in one direction (i.e. the valve closes) whilst in the opposite direction the valve opens when the pressure difference is reversed. Each pump chamber has a pair of check valves arranged such that when one valve is closed the other is open. This ensures the a one way flow of air from outside the pump, through the pump chamber and into the liquid at the pump outlet.

An estimate of the pump performance can now be made. Driving electrical current through the fibers to generate a 5% strain will displace the brass plates by approximately 10 *mm*. Assuming a plate diameter of approximately 50 *mm*, the volume change of the pump chamber per stroke is estimated to be about 20 *cm*<sup>3</sup>. The pressure head that can potentially be generated in this pump

configuration is based on the maximum force generated by the fibers. Assuming a  $10\text{ N}$  force (based on  $250\text{ }\mu\text{m}$  diameter NiTi fibers), the maximum pressure that can be produced is approximately  $5\text{ kPa}$ .

#### 5.4.2.1 Experimental Results

The experimental set up to measure the bellows NiTi fiber pump operation is shown in Figure 51. A contraction sequence is programmed in software and used to activate the fibers in each pump section through the DigiBoost circuit. The battery voltage was six volts and the current pulse duration per fiber, the number of contraction cycles and the time between contraction cycles is software programmable. With a nominal setting of  $300\text{ ms}$  current pulse duration we observed a volume displacement of about  $15\text{ cm}^3$  per contraction cycle -similar to the displacement estimated earlier. Allowing approximately  $3\text{ s}$  between contractions to allow the fibers to cool results in a pumping rate of  $600\text{ cm}^3/\text{min}$  that exceeds by at least two orders of magnitude the required pump rate of  $1\text{ cm}^3/\text{min}$ .

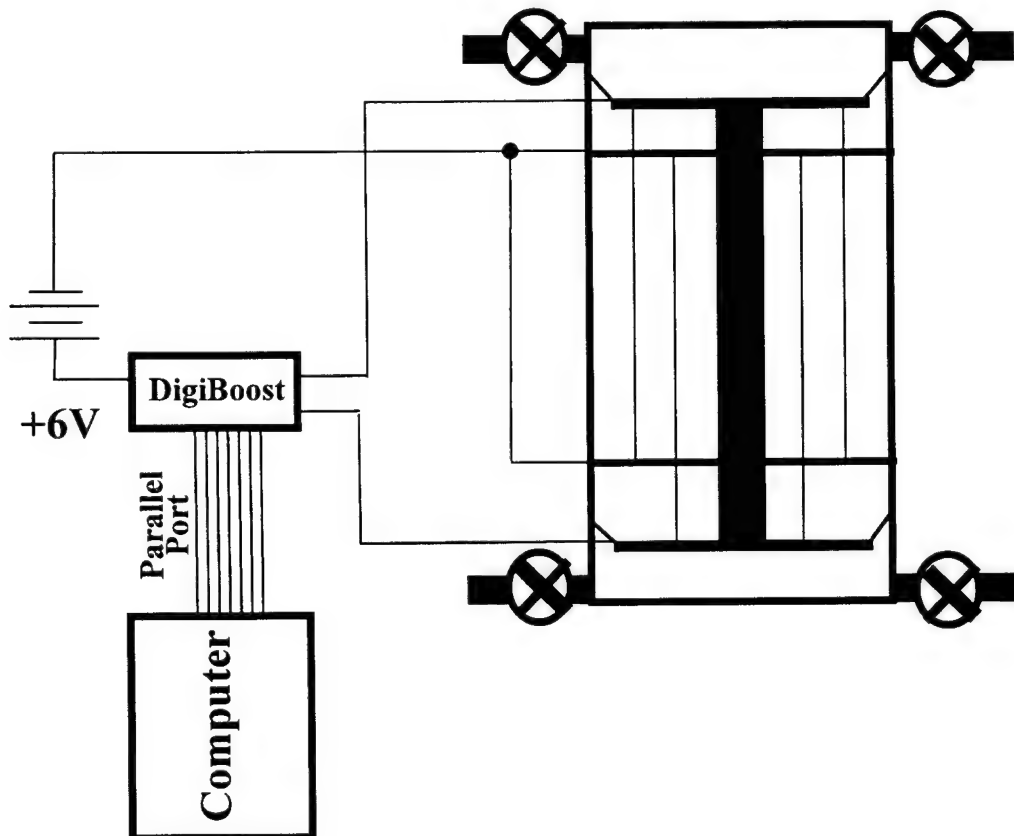


**Figure 51:** Schematic showing experimental arrangement to evaluation operation of second NiTi bellows pump.

#### 5.4.2.2 Conclusion

A bellows pump was built based on contraction of NiTi fibers to change the volume of a flexible bellows and expel air from chamber. The maroscale version of the pump resulted in a pumping rate at least two orders of magnitude larger than what is required of an air inlet pump. These results suggest this pump design can be made substantially smaller yet whilst meeting the pumping rate required for air inlet pumps.

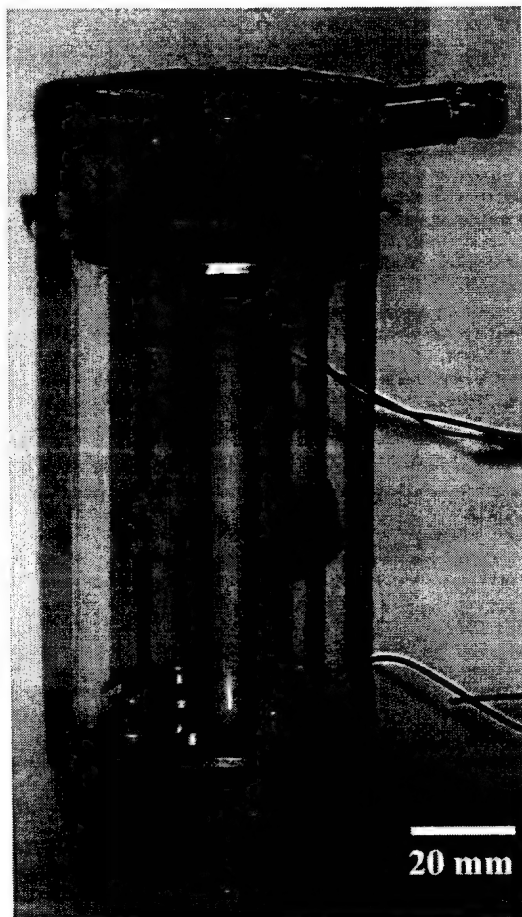


**Figure 52:** Photograph of SMA bellows pump-Version 2. The two pumping chambers are visible on opposite end of the white Delrin rod in the center of the picture. The attachment points for the NiTi fibers are the Al disks located at either end of the Delrin rod. Attached to the rod ends are the brass plates that are flexed to change the dimensions of the pumping chamber. In the upper right is one of the check valves.

### **5.4.3 Peristaltic SMA pump**

#### **5.4.3.1 Principle of Operation**

The second SMA pump design we investigated was one based on peristaltic action. NiTi fibers are arranged such that their sequential contraction squeezes a bolus of material through a flexible tube. The volume of material pumped is directly dependent on the volume of tube collapsed by the fibers during the contraction sequence. The mass flow rate of material through the pump is determined by the rate of volume change per contraction cycle. Thus a given flow rate is achieved by either small volume changes at high repetition rates or large volume changes at low repetition rates. In the first case, the time modulation of the flow rate is small while in the second case the flow pulsation is larger. A variety of materials can be pumped in this manner including gases, liquids of different viscosity and slurries. A peristaltic pump operates without valves, which keeps the pump design and construction simple. High outlet pressures can be generated by the peristaltic action but with the potential disadvantage of a pulsating flow. However, the flow pulsation could be advantageous if delivery of precise and discrete quantity of material is desired. Additionally, the modulated mass flow when coupled with a detector technology could be used as part of a signal-processing scheme to increase detection sensitivity of materials in the flowstream. Multiple lines can be multiplexed into a single pump configuration to either increase the rate or the diversity of materials (i.e. a different material per pumping channel) pumped.

#### **5.4.3.2 Pump Design**

A schematic of the prototype pump is given in Figure 53 and a photograph of the pump is in Figure 54. The pump is constructed from three Delrin sections in which each section divided into two halves separated by 4 *mm* CuBe leaf spring arrayed along either edge of the pump sections. Once assembled, the outside dimensions of the pump are 25 *mm* in width by 70 *mm* in height by 40 *mm* in length with an approximately 4 *mm* spring-loaded gap between the two sections. Eight 250  $\square\text{m}$  fibers are wrapped circumferentially around the three sections with two sections having three equi-spaced fibers and one section two. Each fiber is held in place by a pair of 3 *mm* cap screw around which the fiber is wrapped several times. Between the fibers and Delrin plastic is a layer of Mylar tape to protect the plastic from melting when in contact with the heated NiTi fibers.

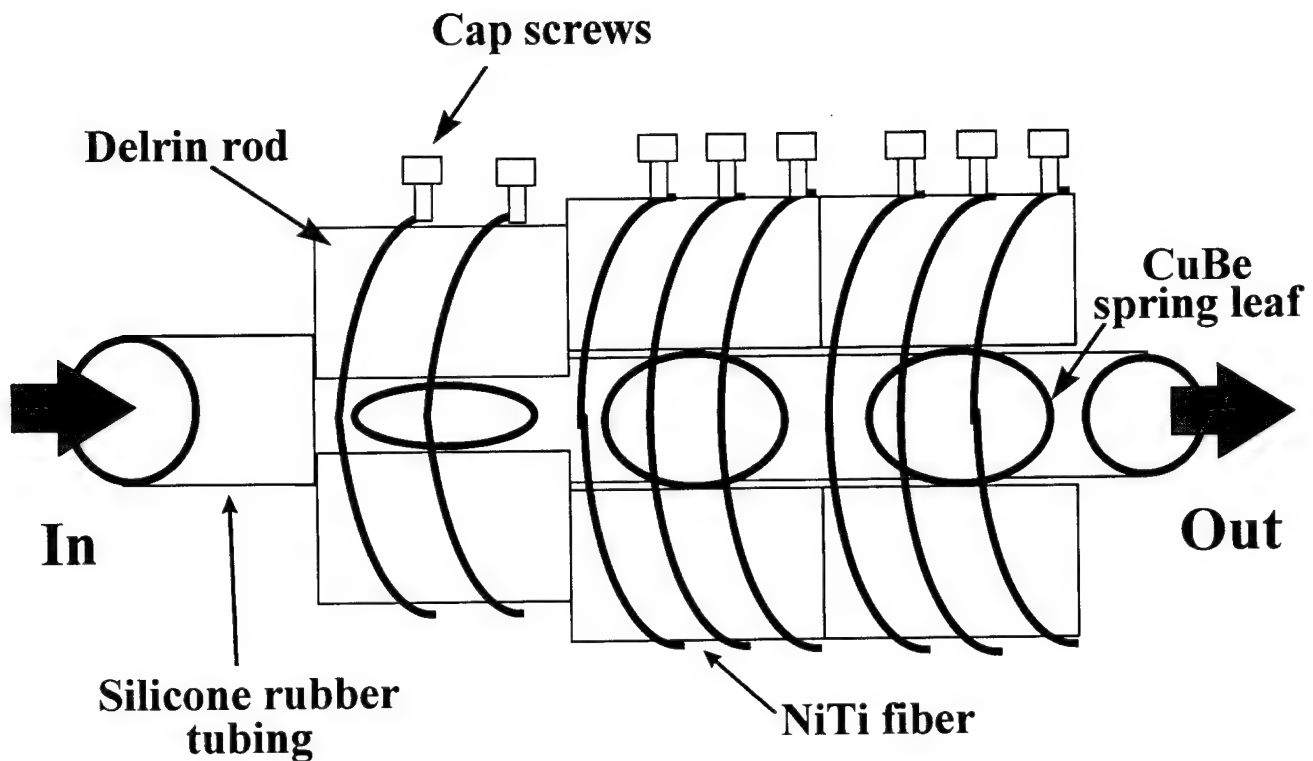


**Figure 53:** NiTi fibers peristaltic pump schematic

Inserted into the gap between the two halves is a  $4.6\text{ mm}$  OD,  $3.3\text{ mm}$  ID silicon rubber tube whose length extends beyond either end of the pump assembly. The low elastic modulus of silicone rubber does not provide sufficient restoring force to return the fibers to their original position on cooling hence the need for the CuBe spring leaf. The fibers are heated with  $0.75\text{ A}$  to produce a 5% strain. Over the  $70\text{ mm}$  long fiber length, this results in a longitudinal dimensional change of  $3.5\text{ mm}$  - sufficient to close the gap between the two pump halves and collapse the tubing. The closure can be made air tight because of the  $20\text{ N}$  of force applied by the fibers to the tubing. A slight bias is applied to the tubing to ensure that the tube walls touch each other when the fibers fully contract. Consequently, with a gap of  $2.88\text{ mm}$ , the total volume that can be expelled from the length of tubing in the pump ( $120\text{ mm}$ ) is estimated to be  $0.47\text{ cm}^3$ . With approximately six contraction cycles per minute, the pumping rate is estimated to be approximately  $2.82\text{ cm}^3/\text{min}$ .

### 5.4.3.3 Experimental Results

The experimental set up to measure the peristaltic NiTi fiber pump pumping rate is shown in Figure 55. A contraction sequence is programmed in software and used to activate the fibers in each

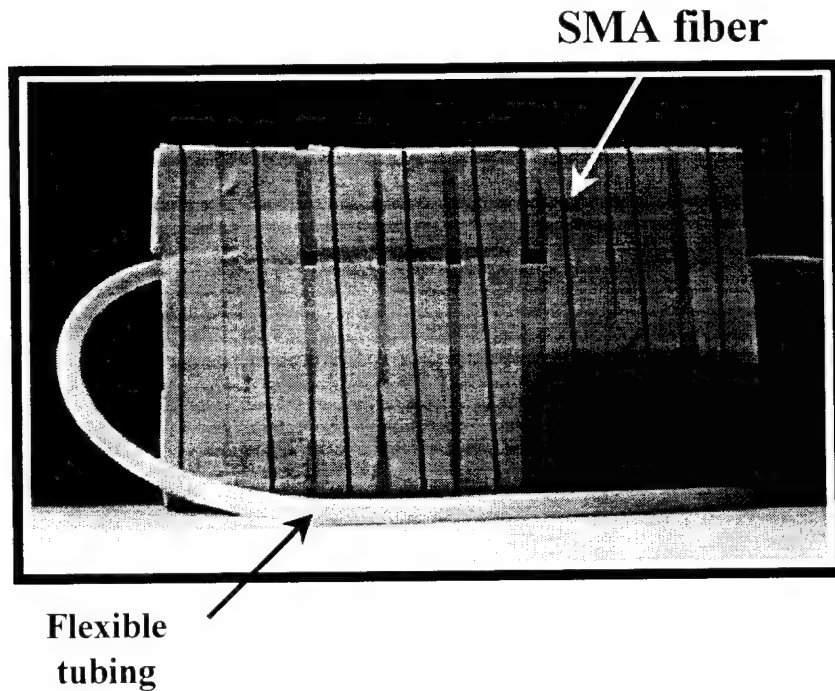


**Figure 54:** Photograph showing SMA peristaltic pump configuration.

pump section through the DigiBoost circuit. The battery voltage was  $6V$  and the current pulse duration per fiber, the number of contraction cycles and the time between contraction cycles was software programmable. With a nominal setting of  $300\text{ ms}$  current pulse duration we observed a volume displacement of  $0.2\text{ cm}^3$  per contraction cycle -within a factor of two of the estimated volume displacement. The difference could arise from the tube not being fully compressed during a contraction because the thickness of the compressed CuBe spring leaf is slightly thicker than the compressed tube thickness. Increasing the current pulse width to greater than  $300\text{ ms}$  saw no increase in displaced volume while decreasing the pulse width resulted in a decreased volume change because the NiTi fibers did not have time to fully contract. Making the time between contraction cycles equal to the time for one cycle ( $3\text{ s}$ ) gives sufficient time for the fibers to cool and relax back to their original

length. The pumping rate under these conditions was measured to be  $2 \text{ cm}^3/\text{min}$  -twice the target flow rate.

#### 5.4.3.4 Conclusion –Peristaltic pump

A peristaltic pump was built based on the sequential contraction of NiTi fibers to expel material from a flexible tube. Evaluation of the prototype operation showed that it pumped air at over twice the target pump rate of  $1 \text{ cm}^3/\text{min}$ . Further evaluation of the pump operation will include measurement of the pressure head generated by the pump and evaluation of its pumping rate with liquids and slurries. Optimization is also required to decrease the physical volume of the pump whilst maintaining a high pump rate. It is expected that a NiTi fiber peristaltic pump will find many applications that require a degree of portability and small size

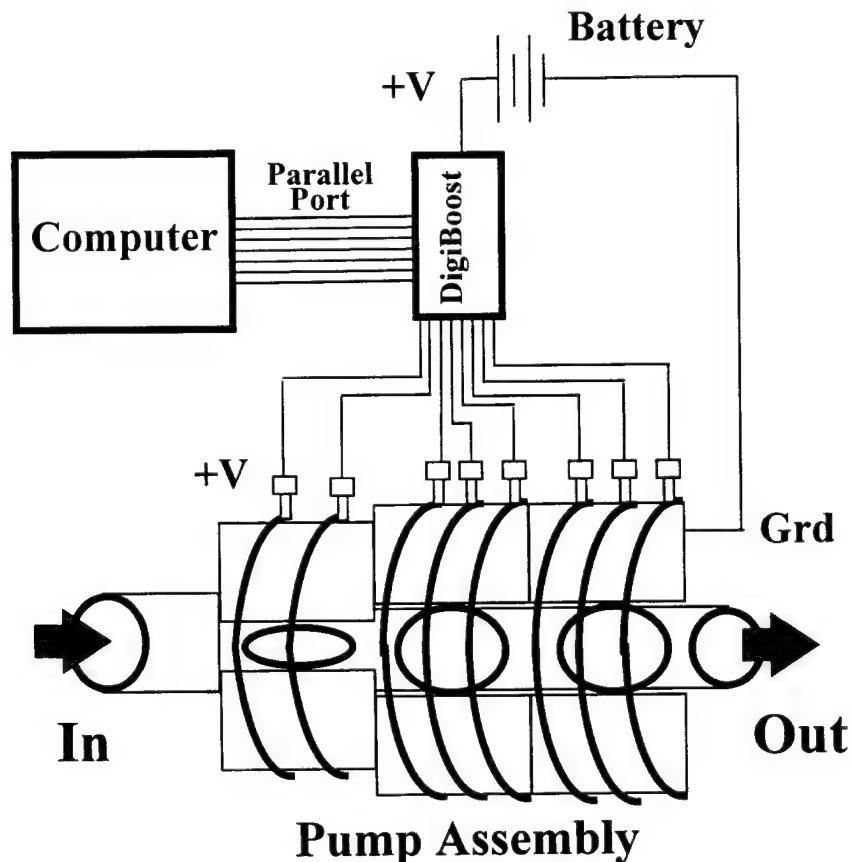


**Figure 55:** Schematic showing experimental arrangement to evaluation operation of NiTi fiber peristaltic pump.

## 6.0 Summary and Conclusions

A Phase I SBIR research project was performed to evaluate and demonstrate new polymer based inlet samplers for biological and chemical agent detection systems. The focus was on polymer systems, and the potential of polymers to form the basis for such systems was demonstrated in the course of this research. Air to liquid sampler prototypes, incorporating NiTi SMA pumps, were developed and demonstrated, proving pump design concepts and exceeding targeted sampling rates. In addition, key adjunct components of the pump – gas driven controlled release capsules - were fabricated as components of an inlet system.

**Task One** of the program involves the evaluation of several competing pump designs. It is demonstrated in Section 2 that paddle and fan-based designs are impractical in air, due to the relative increase in viscous forces as compared to the inertia of the flow (as determined by the Reynolds number). Displacement designs are then analyzed in terms of the required pump characteristics, which are then related to requirements on actuator performance. It was determined from this analysis that the data available on conducting polymer actuators was both insufficient and incomplete to be certain that these would in fact meet the specified requirements. Consequently, a major component of the work performed in Phase I was devoted to a thorough experimental characterization of the conducting polymer material. Extensive measurements were made on electrolytically-grown polypyrrole films of the actuator characteristics identified to be important to actuate the air inlet pump designs of Section 2. Our results show that conducting polymer actuators of this type exhibit electro-mechanical characteristics that meet, or in many cases exceeds, the required actuator characteristics. Furthermore, since polymeric actuators have been demonstrated heretofore only in bulk liquid environments, it was recognized that a key challenge was demonstration of bilayer operation independent of the external environment. This led to our creation of a bilayer encapsulation method which subsequently resulted in a demonstration of conducting polymer bilayer operation in air. This new and substantial technological achievement is a key accomplishment of this program. Accordingly, we have filed a patent application on this technology.

**Task Two** of the project is the fabrication an aerosol pump that meets the performance criteria specified in Task One. These are a flow of  $0.1 \text{ cm}^3/\text{min}$  at a pressure of  $20 \text{ kPa}$ , as was determined

necessary to meet the requirements of many biological and chemical detectors. By relating the pump requirements to actuator properties, we have shown that conducting polymer actuators have the necessary properties to meet or exceed the design goals. Peristaltic and bellows pumps were fabricated, tested, and shown to meet or exceed the requirements. The actuator employed in the prototypes are NiTi shape memory alloys, which have very similar contractile properties to conducting polymers. These were employed as a temporary substitute while studies of conducting polymer actuator properties were underway. Creation of piston and peristaltic pumps actuated by NiTi SMA fibers is a second substantial accomplishment of this work and a patent application has been filed on this technology as well.

Task Three of the project was to fabricate and analyze aerosol /fluid exchange components. This task, in turn, was broken into three subtasks, namely the fabrication of microelectrocilia, fabrication of field driven self assembled enclosures and the fabrication of voltage driven ionic conduction chemical release capsules. As described in Section 3, the demonstration of microelectrocilia operating in electrolytic solution was accomplished early on in the project and was extended to operation in air (i.e. independent of the external environment). The self-assembled enclosures in an electrolyte were demonstrated prior to the projects beginning in a number of laboratories and are a straightforward extension of the microelectrocilia technology.

A controlled release capsule based on ionic condition was demonstrated and its operation characterized. BOMEC is presently exploring commercial applications of this technology by itself or as part of a larger system containing gas sensors to control the release rate of a compound contained within the capsule.

Completion of the project tasks led to the following new and substantive advances in actuator technology:

1. The first comprehensive model of conducting polymer actuators, combined with extensive testing of actuator electro-chemo-mechanical behavior, which led to identification of the key properties needed for sampling inlets.

2. The first demonstration of self-contained, electrically activated conducting polymeric actuators operated outside a liquid electrolyte. These devices meet the design requirements for the microcilia and self-assembled enclosures of the air sampler detection module.
3. The first demonstration of ionic conduction based gas driven material injectors suitable for a number of controlled chemical release functions.
4. The first demonstration of peristaltic and piston-style pumps actuated with shape memory alloy. Although macroscale versions of these pump designs were built and tested, their miniaturization is a straightforward process and would be suitable for a Phase II follow-on program.

These many accomplishments in Phase I of this program clearly demonstrate the potential of this technology to meet military needs for sampling inlet and a wide range of other robotic applications. Indeed, the conducting polymer actuators have the stress, strain and bandwidth properties to make a significant impact in present and future military systems. These materials have inherently low detectability and are compatible with ambient operating conditions. The BOMEC approach is to develop subsystems consisting of substrates actuators, active devices and passive devices on a single substrate, AMPS or adaptive polymeric Subsystems. Phase II effort by BOMEC will capitalize on the advances in state of the art actuators and materials developed in Phase I and will lead to practical CBW inlet pumps for field testing and as well as the demonstration, through modeling and demonstration of key component performance, of a wide range of systems for both military and civilian applications.

## **7.0 Acknowledgements**

We would like to express our appreciation for the support and encouragement of DARPA for supporting this work and the cooperation of Dr. Mildred Donlon, and the DARPA staff as well as inputs from Perry Peterson and his colleagues at Dugway Proving Ground. We would also like to thank Steve Hartenstein, William Blume, William Motes and the staff of Lockheed Idaho National Engineering Lab for valued discussions on air sampler requirements.

We would like to thank the efforts of BOMEC staff researchers Dr. Colin Brenan, Mr. John Madden, Dr. Serge Lafontaine, Dr. Joel Dubow, Dr. Douglas Chinn and Mr. B. Ganesh on this project. Without their dedication the accomplishments of this program would have never been attained.